Chapter 9
Underwater Shock Waves

9.1 Introduction

Liquids are less compressible than gases. The compressibility is the measure of volume change when compressed by pressure. A pressure increment Δp is proportional to a relative volume change $\Delta V/V_0$,

$$\Delta p = -E\,\Delta V/V_0 \tag{9.1}$$

where V is specific volume, $V = 1/\rho$, V_0 is an initial volume, and E is the modulus of elasticity which has the dimension of pressure.

The sound speed is defined as

$$a^2 = (\partial p/\partial \rho)_s \text{ in isentropic condition} \tag{9.2}$$

The sound speed is related to the modulus of elasticity and it is defined as,

$$a = (E/\rho)^{1/2}. \tag{9.3}$$

Therefore, a pressure increase of 100 kPa in water at ambient condition reduces the volume of water only by 0.005 of the original volume, whereas when the same pressure applied to air the occupied volume is reduced to one half of its original volume. Water is less compressible than air and sometimes considered to be incompressible.

In an incompressible medium, as the density does not change and then $\Delta \rho = 0$. Hence, the sound speed is infinitely large so that the sound speed in water is much higher than that in air. In the incompressible flows, the information is transmitted

K. Takayama, *Visualization of Shock Wave Phenomena*,
https://doi.org/10.1007/978-3-030-19451-2_9

instantaneously everywhere in the flow field. Therefore, the flow Mach number is always zero. On the contrary, in compressible flows, a pressure perturbation Δp induces a particle velocity Δu as given by,

$$\Delta p = a\rho \, \Delta u, \tag{9.4}$$

where $a\rho$ is defined as the acoustic impedance. Equation (9.4) is derived from the conservation equations and the definition of sound speed.

The acoustic impedance is a coefficient which relates the pressure perturbation and the velocity perturbation. Recalling the Ohm's law in electricity and replacing the pressure perturbation and the velocity perturbation with the electrical voltage and the electrical current, respectively, the acoustic impedance is equivalent to the resistance in the flow.

The acoustic impedance is a measure of the compressibility. The acoustic impedance in water is approximately 3500 times larger than that of air. A given pressure increase in water induces particle velocity of 1/3500 of those induced in air. Glass and Heuckroth (1968) ruptured a glass spheres containing several ten atmospheres of gases in water and generated a low energy underwater shock wave. Today underwater shock waves are generated in a small scale underwater explosion but the pressure exceeded a few GPa.

In gases, the pressure decreases down to vacuum, whereas in liquids the pressure cannot decrease below the liquid's vapor pressure. When the pressures approach to the vapor pressure, the liquids start to evaporate. Water evaporates at 373 K at atmospheric pressure. The Bernoulli equation in incompressible flows is written as

$$p + \rho u^2/2 = P \tag{9.5}$$

where ρ, the density which is constant abd. When the flow velocity u increases, p decreases close to the water vapor pressure. Then water starts to boil even at room temperature. This phenomenon is named "Cavitation". Cavitation appears when water is suddenly exposed to a large tensile force. Upon the exposure to a high tensile stress, water shifts in the phase diagram from liquid phase to gas phase, in short, starts to evaporate inducing a cloud of water vapor. Therefore, the cavitation phenomenon plays an important role not only in the underwater shock wave research but also in the bubble dynamics.

Underwater shock wave research and bubble dynamic research are linked in their applications not only for engineering applications but also in biology and medical applications.

9.2 Underwater Micro-explosion

9.2.1 Micro-explosives

In 1981, the collaboration with Dr. Kuwahara of Tohoku University Hospital started. It was invited us to collaborate for the development of Extra corporeal shock wave lithotripsy, in short ESWL, using micro-explosives produced in house. A prototype lithotripter was designed (Takayama 1983). Meantime, the Chugoku Kayaku Co. Ltd. kindly supplied 10 mg AgN_3 pellets supporting the ESWL research (Nagayasu 2002).

Figure 9.1a shows an infinite fringe interferogram of a spherical shock wave generated by exploding a 4 mg of PbN_6 pellet taken after 34 μs from the ignition. Figure 9.1b shows results deduced from the fringe analysis. The pressure profile behind the shock wave is shown in Fig. 9.1a together with appropriate numerical simulation based on the Random Choice Method. Figure 9.1c shows a scaled distance diagram of the overpressures created by micro-explosions. The ordinate denotes overpressures normalized by the initial pressure and the abscissa denotes the scaled distance $m/kg^{1/3}$. Black filled circles denote shock overpressures obtained by the explosion of 4 mg PbN_6 pellets, red filled circles denote the pressures obtained by the exploding of AgN_3 pellets from 10 to 300 μg measured at stand-off distance of 10 mm, blue filled circles for AgN_3 pellets from 3 to 100 μg measured at stand-off distance 5 mm. It is noticed that the scaling law agrees well even in the case of small explosives.

A PbN_6 pellet was glued on a thin cotton thread and suspended in water as seen in Fig. 9.1a. Irradiation of a Q-switched ruby laser beam on to the explosive ignited it. A PbN_6 pellet has energy about 1.5 J/mg and hence a 4 mg PbN_6 has total energy of about 6 J, however, one third of its energy was consumed in an underwater shock wave formation. The ignition laser beam had energy of less than 10 mJ but the laser energy would not contribute to the shock wave formation. Later the laser ignition method was improved: A explosive pellet was glued on the edge of a 0.6 mm diameter quartz optical fiber. The transmission of a Q-switched Nd:YAG laser beam of energy of 10 mJ and 7 ns pulse width through it ignited the small explosive.

Figure 9.1a shows a co-axial fringe distribution taken at magnification of 0.5 time. Fringes are formed due to the integration of the density profile along the *OB* path but clear enough to resolve the interval between neighboring fringes. Assuming that the flow field is spherical, the density distribution behind the shock wave was determined by counting the fringes and their intervals. The measured densities and the numerical simulations were compared. When the density jump across the shock wave is determined, then the pressure profile is calculated using the Tait equation. The Tait equation is an empirical equation of state of water valid below 2.5 GPa (Tait 1888).

$$(p + B)/(p_0 + B) = (\rho/\rho_0)^n, \tag{9.6}$$

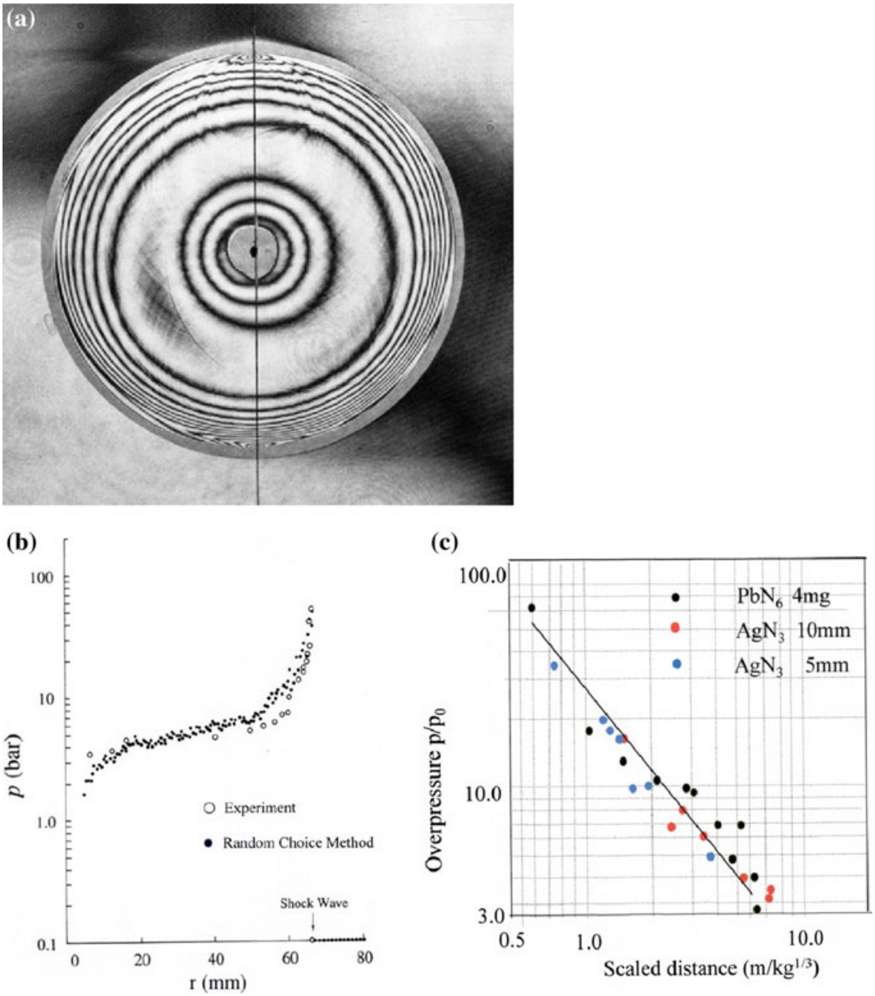

Fig. 9.1 A spherical underwater shock wave: **a** #83011712. Infinite fringe interferogram of 4 mg PbN_6 at 34 μs after ignition; **b** comparison with Random Choice Method; **c** dimension-less pressure versus scaled distance (Sachs 1944)

where p_0 and ρ_0 are ambient pressure and density, B = 300 MPa and n = 7.145. Once the peak density is given, the pressure profiles of the entire flow fields are determined by Eq. (9.6).

But it should be noticed that the *OB* path length was zero at the shock front therefore the density across the shock front could not be resolved. Then the pressure jump across the shock wave was taken from a pressure transducer reading.

9.2.2 Underwater Shock Waves

Figure 9.1c shows the scaling law of a shock wave overpressure. The ordinate shows an overpressure and the abscissa shows the scaled distance in m/kg$^{1/3}$ (Sachs 1944). Red and blue filled circles denote overpressures generated by explosions of AgN_3 pellets weighing from 3 to 300 μg at stand-off distance of 5 and 10 mm, respectively. Black filled circles denote overpressures of explosions of 4 mg PbN_6 pellets at stand-off distances of 10–80 mm. Normalized overpressures were expressed in the scaled distance regardless of types of explosives. The experimental results were compared with an appropriates simulation based on the Random Choice Method, RCM (Esashi 1983). The explosion of 4 mg PbN_6 pellet was assumed to be equivalent to a 2.0 mm diameter air bubble having the pressure and temperature at 1 GPa and 2800 K, respectively. The air bubble is placed at the center of a 100 mm radius water chamber at ambient condition of 100 kPa and 293 K. Pressure and the density variations are shown in Fig. 9.2a. The ordinate in Fig. 9.2a denotes the time and the abscissae denote the dimensionless distances normalized by the bubble radius. As soon as the bubble is released into water, the diverging underwater shock wave propagates outward and an expansion wave converges toward the center. The high pressure air becomes an expanding bubble. At the same time, the converging expansion is reflected at the center of the bubble and becomes a secondary shock wave.

The diverging shock wave is reflected from the outer wall at the 100 mm distance from the center. When the reflected shock wave encounters with the diverging bubble surface, the bubble starts contracting. Then the pressure outside the expanding bubble starts spontaneously contract. The sudden bubble contraction creates cavitation bubbles. The RCM (Esashi 1983), however, can not numerically reproduce the cavitation.

Figure 9.2b shows a streak recording of a shock wave generated by explosion of a 5 mg AgN_3 pellet. The ordinate denotes elapsing time in μs and the abscissa denotes a shock wave radius in mm. The scale of the streak recording was 10 μs/mm. A 5 mg AgN_3 pellet was glued at the edge of a 0.6 mm core diameter optical fiber and ignited by transmitting a Q-switched Nd:YAG laser beam through it. The detonation gas products appear as a dark shadow expanding vertically. Dark oblique lines running from the center are trajectories of the resulting spherical shock wave. The detonation speed of the AgN_3 pellet is about 2.89 km/s and hence its Mach number is $Ms = 1.93$. However, it attenuated exponentially with elapsed time to $Ms = 1 + \varepsilon$, and takes relatively long time to fully recover to a sound speed. Oblique lines appearing at later time are trajectories of reflected shock waves from the side wall.

Figure 9.3a shows a sequential observation of explosion of a 10 mg AgN_3 pellet using ImaCon 790 at framing rate of 10^5 frame/s. The detonation product gas expanded initially very fast as seen in Fig. 9.2b, but quickly attenuated. When it ceased to expand, the debris particles, probably non-reacted particles, were shattered from the surface of the explosive and penetrated the detonation product gas.

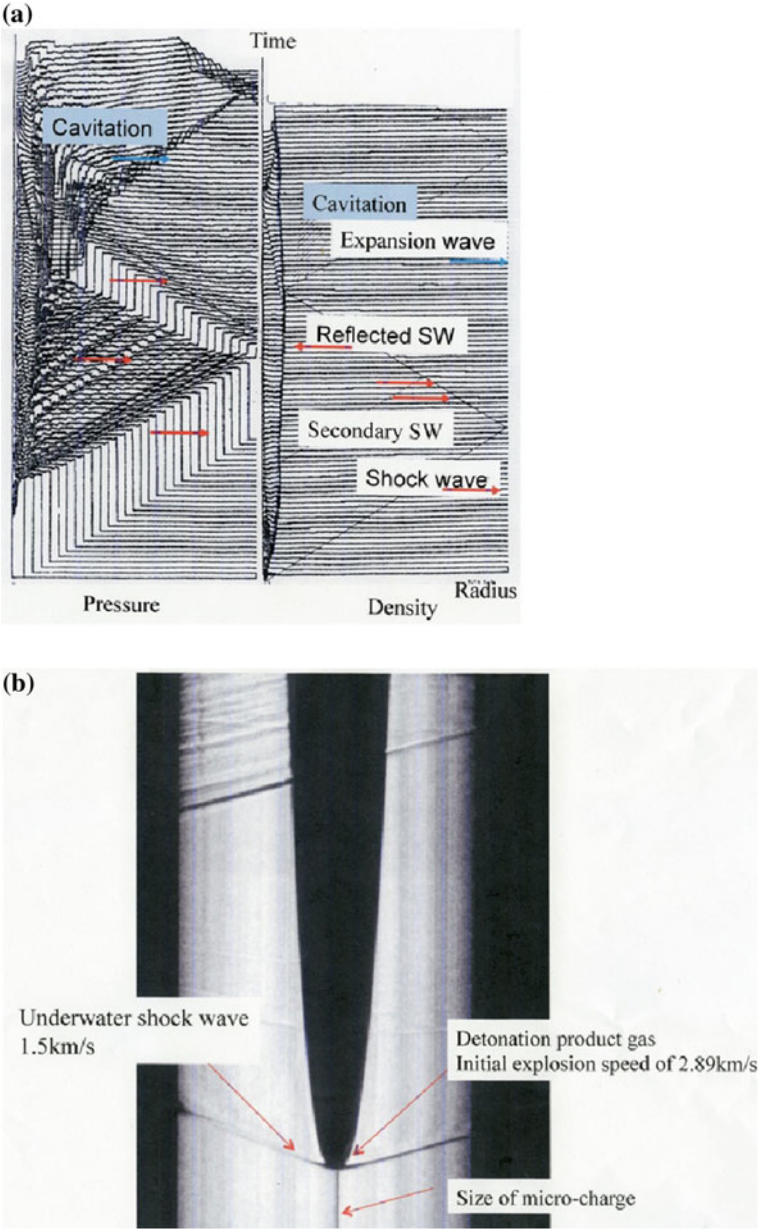

Fig. 9.2 Micro-explosion: **a** RCM numerical simulation (Esashi 1983): **b** streak recording, #90070614, of a shock wave generated by explosion of a 5 mg AgN_3 pellet at streak recording speed of 10 μs/mm

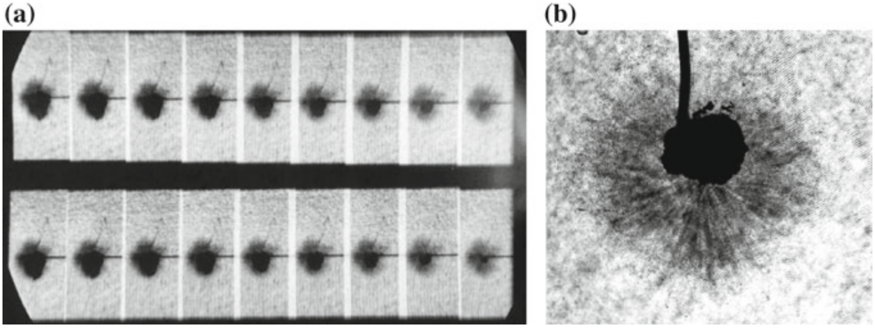

Fig. 9.3 Observation at a later stage of exploding a 10 mg AgN_3 pellet: **a** #90070908, 10^5 frame/s; **b** #92011611 taken at 4.2 ms after ignition at Tw = 290.1 K

At this time, it contracted and became slightly transparent. Figure 9.3b is a single exposure interferogram taken at 4.2 ms after the ignition. The optical fiber holding a AgN_3 pellet was significantly deformed.

9.2.3 Reflection of Underwater Shock Waves

Glass and Heuckroth (1968) intended to observe the presence of a MR in underwater shock wave reflection by rupturing simultaneously two pressurized glass spheres but were not successful to observed distinct triple points. Coleburn and Roslund (1970) visualized the head-on collision of two underwater shock waves by simultaneous detonations of two 63.3 mm diameter mixture of 50% TNT and 50% PETN weighing 225 g and eventually measured the critical transition angle of 37°, although the images they visualized were not necessarily clear.

As such amounts of high explosive are totally unsuitable to use in university laboratory, underwater shock wave reflections from metal walls were visualized using holographic interferometry, Fig. 9.4a, b shows underwater shock wave reflections from 10° and 150° brass cones. Spherical shock waves were created by explosion of 4 and 10 mg PbN_6 pellets at stand-off distance of 4 and 5 mm at over-pressures of over several ten MPa. In gases, the shock wave reflection pattern from these cone angles show either a MR or a RR. However, in underwater shock wave reflections from brass cones, longitudinal and transversal waves propagate much faster than the underwater shock wave. For example, in brass, the longitudinal wave propagates at 4.7 km/s and the transversal waves propagates at 2.1 km/s. The transversal waves transmitted into water created dense fringes at the foot of underwater shock waves. The fringes were too dense to identify patterns of reflected shock waves. Therefore, it is impossible to determine the critical transition angles by observing underwater shock wave reflections from metal cones.

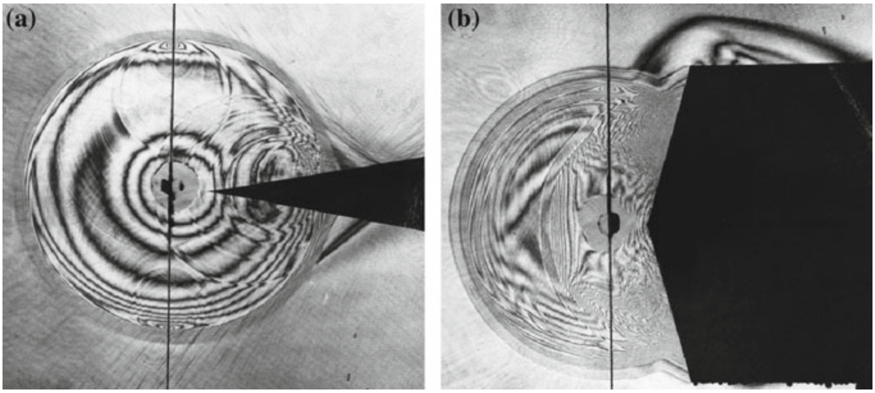

Fig. 9.4 Shock wave reflection from brass cones at 285.8 K: **a** #82122101, a shock wave was generated by explosion of a 4 mg PbN_6 pellet at stand-off distance of 4 mm; **b** #82122105, a shock wave was generated by explosion of a 10 mg PbN_6 pellet at stand-off distance of 5 mm

Eventually, it was decided to observe the reflection of two underwater shock waves having almost identical strengths obtained by exploding 5–6 mg PbN_6 pellets suspended from 4 to 10 mm interval in water. Figure 9.5 shows reflections of two underwater shock waves of identical strengths. Figure 9.5a shows a single exposure interferogram of two 6 mg PbN_6 pellets ignited at 6 mm interval. The resulting reflection pattern was a RR. Figure 9.5b shows the reflection conducted in the same condition as Fig. 9.5a. In the range of the intersection angle as seen in Fig. 9.5d–f, a MR would have appeared but the reflected pattern so far observed was vNMR. Condensed matter, including water, is less compressible than gases so that the particle velocities are always low and the slip lines are hardly generated. Hence the reflected patterns are always vNMR. In detonating two 5 mg AgN_3 pellets separated at 10 mm interval created the observed reflection patterns were vNMR as seen in Fig. 9.5f. Longitudinal waves were also observed along the optical fiber. Figure 9.5g shows enlargement of Fig. 9.5f.

9.2.4 Reflection of Conical Shock Waves Generated by MDF Explosions

Mild detonating fuse (MDF, Ensigh-Bichford Co. Ltd.) is a 2.0 mm aluminum sheath filled explosives HNS (Hexa-Nitro-Stilbene, detonation velocity of 6.8 km/s) (Nagayasu 2002). In order to determine θ_{crit} of reflecting conical shock wave, two 80 mm long MDF pieces were submerged in a test chamber intersecting at variable intersecting an angle α. Figure 9.6a shows the experimental arrangement. 10 mg AgN_3 pellets were glued at the edge of 80 mm long individual MDF, and ignited simultaneously with laser beams. Figure 9.6b shows conical shock wave

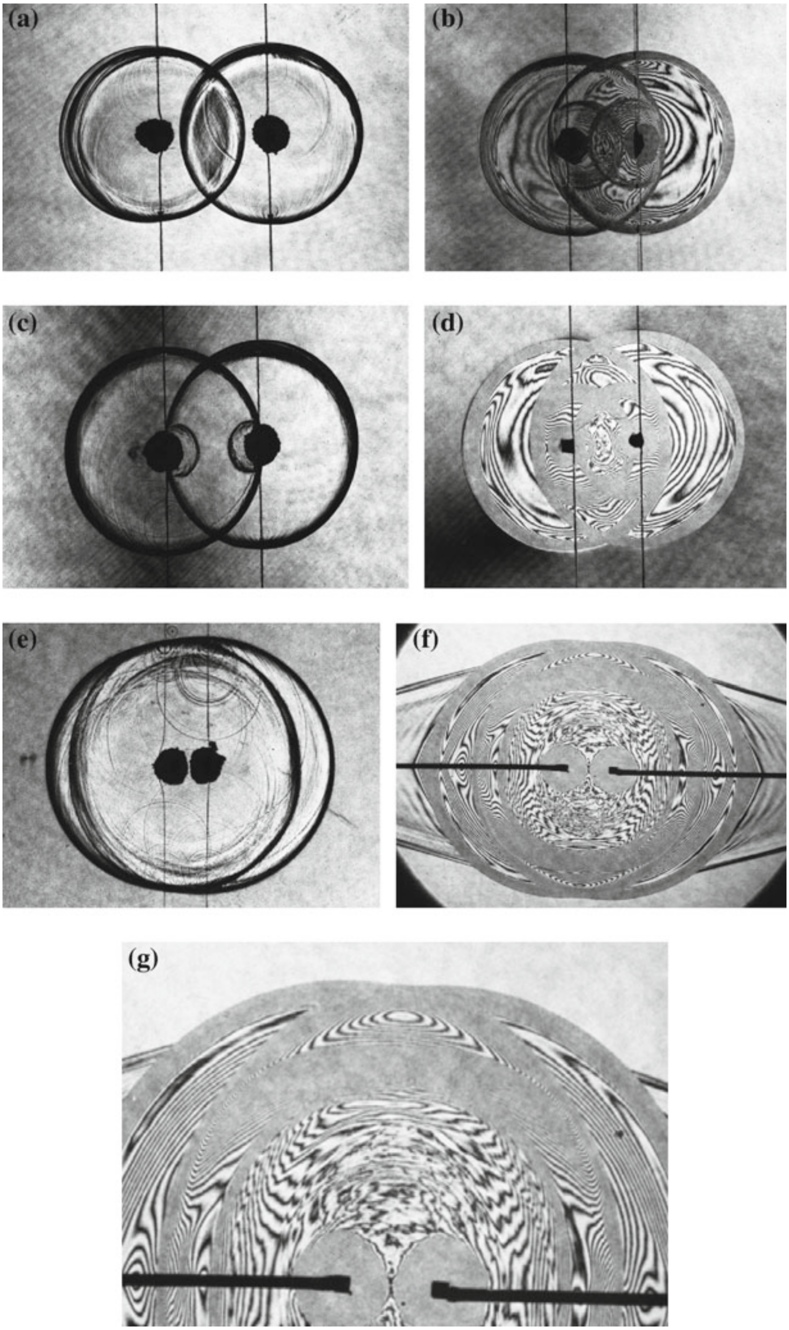

Fig. 9.5 Interaction of two spherical shock waves: **a** #83060208, 3.5 μs from ignition, PbN_6 6–6 mg, at interval L = 6 mm, single exposure, RR; **b** #83060206, PbN_6 6–6 mg, L = 6 mm, RR; **c** #83060302, L = 8 mm, single exposure, RR; **d** #83060102, PbN_6 6–6 mg, L = 10 mm, vNMR; **e** #83120504, PbN_6 5.7–5.9 mg, L = 8 mm, vNMR; **f** #93011205, AgN_3 5–5 mg, L = 10 mm, vNMR; **g** enlargement of (**f**)

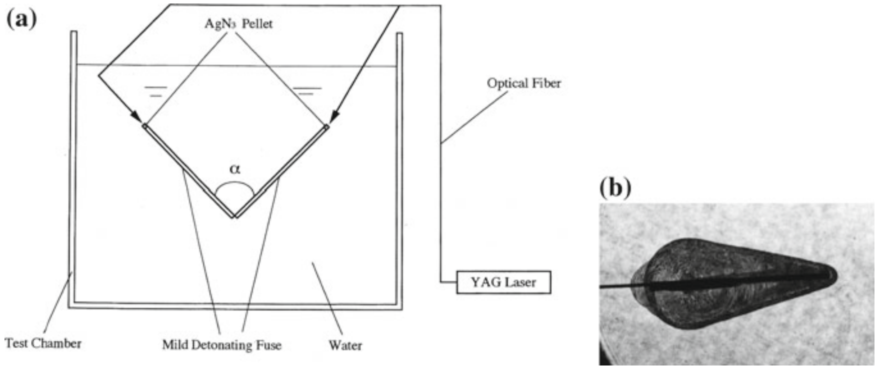

Fig. 9.6 Reflection of conical shock waves: **a** experimental setup; **b** explosion of MDF (Nagayasu 2002)

propagating along the MDF at propagation speed of 6.8 km/s. The shock wave so far generated along the MDF propagated at the constant speed at half apex angle of $\theta = 14.5°$.

Defining the detonation speed of MDF, U_{MDF}, and the conical shock speed U_{cone}, the relationship $\sin\theta = U_{cone}/U_{MDF}$ is valid. Then $U_{cone} = 1.7$ km/s. The sound speed of water being 1.5 km/s, the Mach number of the conical shock wave Ms is 1.14. During the experiments, to suppress bang noises occurred at each shot, the wall of the test chamber was covered with thick sponge sheets.

In Fig. 9.7a–d, the pattern of reflection pattern is a RR. However, in Fig. 9.7e–g, a vNMR appear at the points of the intersection of the incident shock waves, IS and Mach stem MS. Then the position of the triple can be plotted.

Figure 9.8 summarizes the locations of triple points. The ordinate denotes the normalized triple point height h/L, where h is the height of the estimated tripe point and L is the distance from the center of the intersection. The abscissa denotes the initial angle α/2 in degree. Figure 9.8b is a summary of measured data. The ordinate denotes h/L and the abscissa shows the inclination angle in degree. The vNMR occurs at the transition angle of bout 30° (Nagayasu 2002).

9.3 Shock Wave Over a Liquid Surface

9.3.1 PDMS/Water Interfaces

Micro-explosives were frequently exploded in PDMS. PDMS is called silicone which has chemical structure, Polydimethylsiloxane, PDMS: $(CH_3)_3SiO–[(CH_3)_2SiO]_n–SiO(CH_3)_3$. To determine the isothermal compression test of PDMS. Figure 9.9a shows the experimental setup. Figure 9.9b shows an isothermal

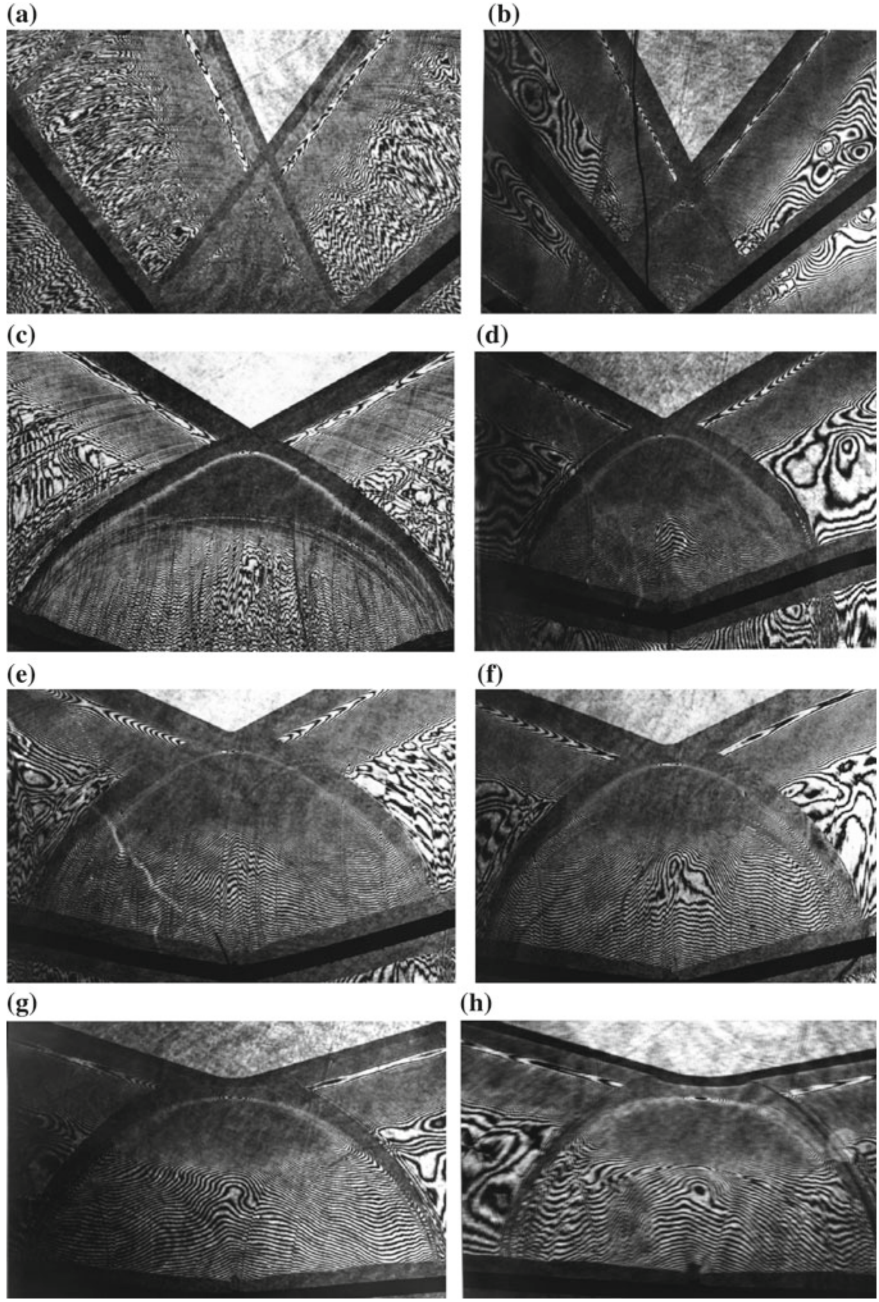

Fig. 9.7 Reflection of MDF generated conical shock waves: **a** #96111307, α = 58°; **b** #96111906, α = 66°; **c** #96111503, α = 95°; **d** α = 114°; **e** #96111904, α = 122°; **f** #96111803, α = 125°; **g** #96111902, α = 134°; **h** #96111901, α = 143°

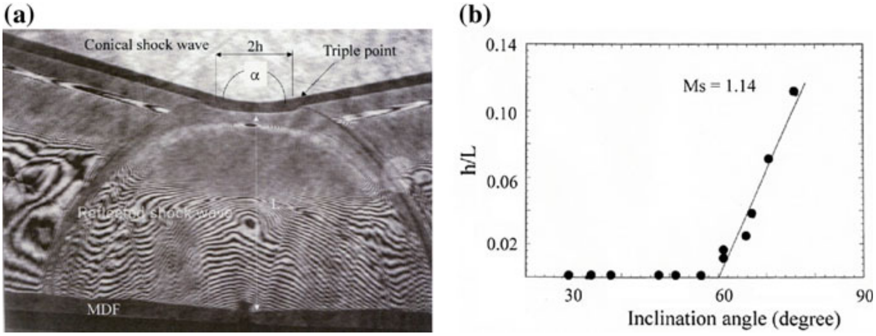

Fig. 9.8 Triple point height h against inclination angle; **a** intersection of two MDF; **b** summary

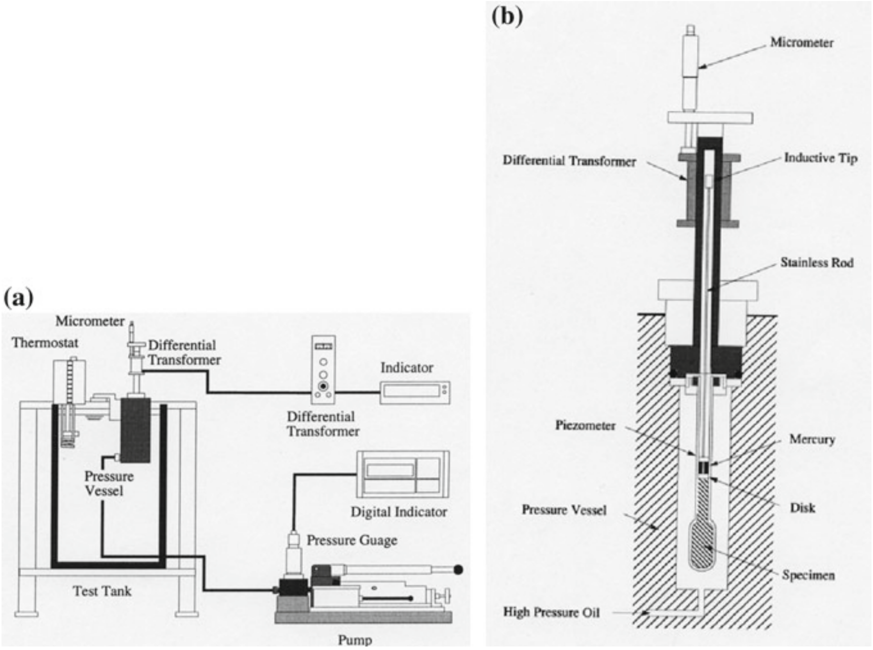

Fig. 9.9 Isothermal compression tester: **a** experimental setup; **b** compression chamber (Hayakawa 1987)

compression system. Filling PDMS in a small glass tester of known volume and compressing the tester with a hydraulic compressor starting from the ambient pressure and up to 250 MPa, the volume change of the tester was measured.

From the measured data, the equation of state of silicon oil can be determined assuming a formulation of the Tait type equation, that is, $(p + B)/(p_0 + B) = (\rho/\rho_0)^n$. The values of the exponent n and B in MPa for PDMS in isothermal conditions are: At 298 K, PDMS 1cSt, density of 0.818 g/cm^3, sound speed of 901.3 m/s; PDMS 10cSt (Shin-Etsu Chemical Industry Co., KF96-10, 10cSt), density of 0.932 g/cm^3, surface tension of 20.1×10^{-3} N/m, sound speed $a_{silicon} = 980$ m/s at 298 K and parameters of Tait type equation of state, n = 9.36 and B = 95.4 MPa refractive index of 1.399 and kinematic viscosity $\nu = 1.0$ 10^{-5} m^2/s; PDMS 100cSt, density of 0.962 g/cm^3, surface tension of 20.9×10^{-3} N/m, and sound speed of 998.7 m/s, n = 10.24, and B = 93.6 MPa; PDMS 1000cSt, surface tension of 21.1×10^{-3} N/m, sound speed of 1000.4 m/s, whereas just for reference those of water at 298 K are viscosity of 0.89cSt, density of 0.997 g/cm^3, surface tension of 20.1×10^{-3} N/m, sound speed of 1496 m/s, n = 7.145 and B = 2.963 MPa (Hayakawa 1987; Yamada 1992).

Prior to the experiments, when micro-explosives were detonated in PDMS, the color in PDMS became yellowish probably due to the thermal decomposition of PDMS. In Fig. 9.10, shock waves in water propagate at 1500 m/s and shock waves in PDMS propagate at 980 m/s. Then the ratio m of acoustic impedances between water and 10cSt PDMS is 1.64. The energy transmitted from PDMS to water $I_{transmission}$ and the energy reflected $I_{reflection}$ is expressed in terms of m,

$$I_{transmission}/I_0 = 4m/(m+1)^2, \quad I_{reflection}/I_0 = (m-1)^2/(m+1)^2 \tag{9.7}$$

where I_0 is the total energy. In the planar wave interaction, approximately 94% of the total energy was transmitted from PDMS to water interface, and about 6% was

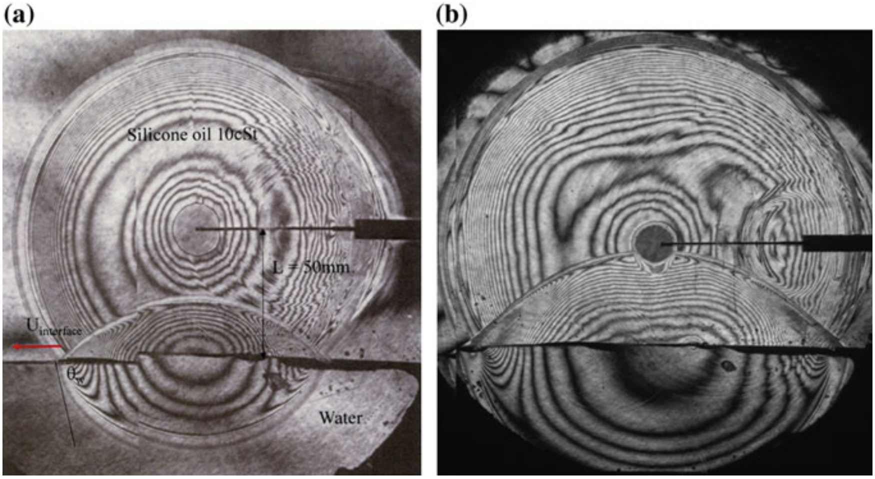

Fig. 9.10 Micro-explosion of 10 mg AgN_3 pellet at L = 50 mm above the interface at 1013 hPa, 296.8 K: **a** #90101603, 76.5 μs from the ignition; **b** #90101605, 92.0 μs from the ignition

reflected from water. Hence the water/PDMS interface would move just a little toward water. Then a shock wave was released into water. Although this estimate is valid only in the case of one dimensional acoustic waves, the predicted value would be a useful estimate of the energy transfer across the water/PDMS interface.

When detonating a 10 mg AgN_3 in PDMS at the distance L = 50 mm above the interface. The spherical shock wave arrived at the interface at $L/a_{silicone}$ = 51 µs and a spherical shock wave was transmitted. Denoting the intersection angle of the shock wave in PDMS with the interface by θ and defining $U_{interface}$ as the propagation speed of the foot of the shock wave along the interface, as seen in Fig. 9.10a, then $U_{interface}$ can be written as following:

$$U_{interface} = a_{silicone}/\sin\theta. \tag{9.8}$$

Equation (9.8) indicates that at the moment when the shock wave in 10cSt PDMS touches the plane interface, θ = 0 and hence $U_{interface}$ is higher than $a_{silicon}$. At $L/a_{silicon}$, the spherical shock wave in 10cSt PDMS induced a transmitted shock wave into the water, that propagated at an earlier stage along the interface at the same speed of $U_{interface}$. Denote θ_w as the intersection angle of the shock wave in water and a_{water} the sound speed of water, then

$$U_{interface} = a_{water}/\sin\theta_w. \tag{9.9}$$

As seen in Fig. 9.10a, at earlier stage θ_w is always larger than θ, hence the relation $a_{water}/\sin\theta_w = a_{silicone}/\sin\theta$ is valid. However, when this condition is violated, the shock wave in water propagates ahead of the shock wave in PDMS and a precursory oblique wave appears ahead of the shock wave in PDMS.

9.3.1.1 Explosion in PDMS Above the PDMS/Water Interface

Figure 9.11 shows the interaction of explosively generated spherical shock wave (by a 10 mg AgN_3 pellet), initiated 10 mm above the PDMS/water interface with PDMS over the water interface.

Figure 9.12 shows the evolution of the interaction of the spherical shock wave create by explosion of a 10 mg AgN_3 pellet at stand-off distance of L = 30 mm above a PDMS/water interface in PDMS over water interface.

9.3.1.2 Explosion in Water Below PDMS/Water Interface

Figure 9.13 shows the explosion in water at the stand-off distance of 10 mm below the PDMS/water interface. The pressure in water behind the reflected shock from the interface wouldn’t decrease below the water vapor pressure, therefore, bubbles

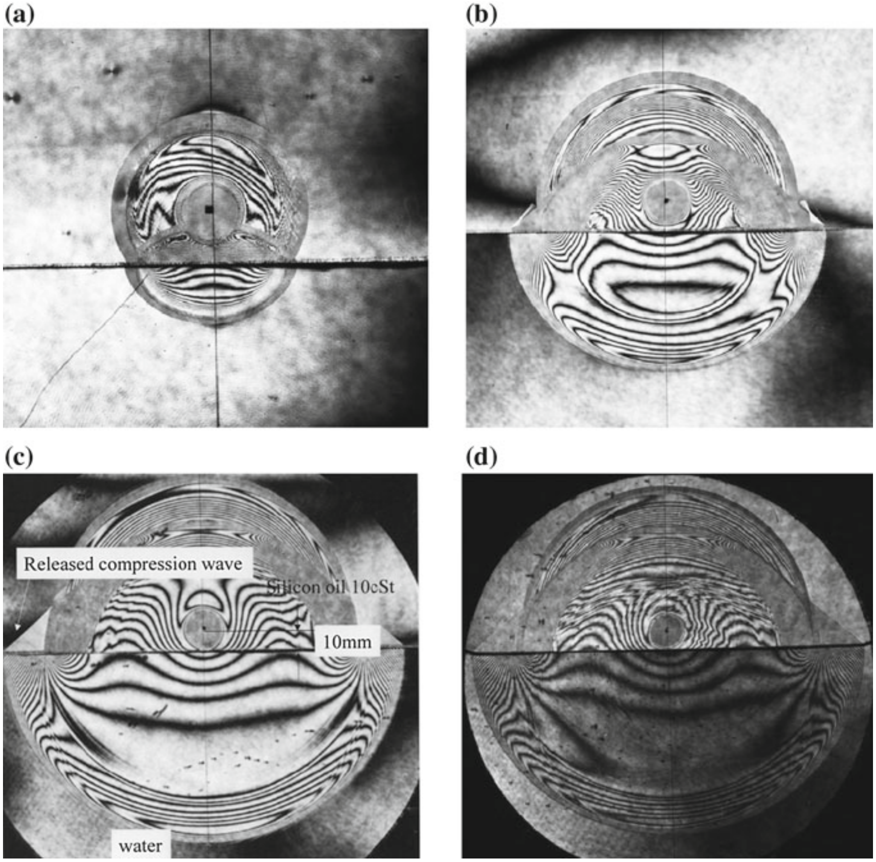

Fig. 9.11 Shock wave generated by explosion of a 10 mg AgN_3 pellet ignited at L = 10 mm above a PDMS/water interface at 1013 hPa, 297 K: **a** #92123002, 16 µs from ignition; **b** #92123102, 42.5 µs; **c** #92122901, 63 µs; **d** #92122902, 86 µs

are hardly initiated. A shock wave in PDMS is always followed by a precursory oblique wave. A secondary shock wave was generated behind the direct shock wave in water.

9.3.1.3 Explosion at PDMS/Water Interface

Figure 9.14a–d shows sequential single exposure interferograms. Shock waves were generated by exploding 8.7–9.0 mg AgN_3 pellets in 1cSt PDMS at L = 3 mm above the PDMS/water interface. Figure 9.14e–i also shows sequential single

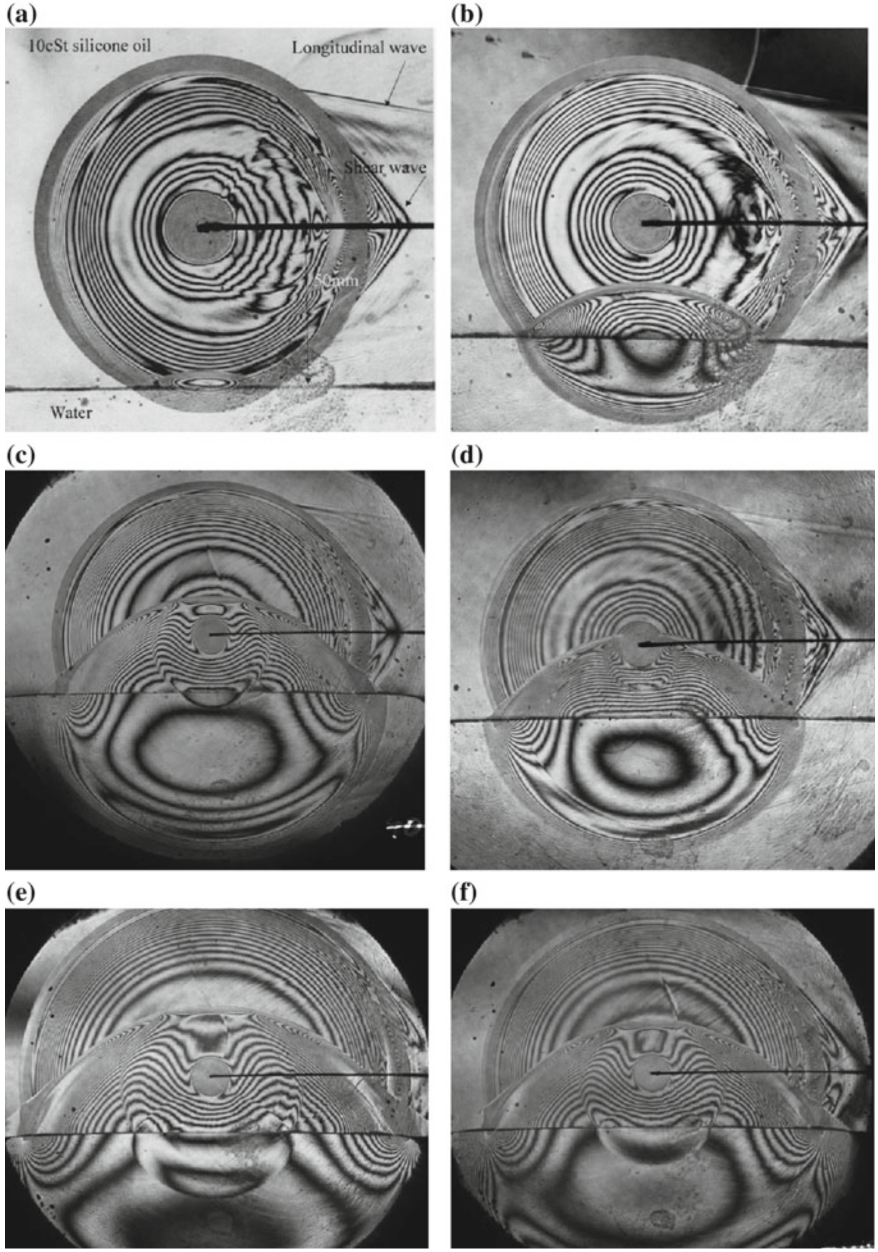

Fig. 9.12 Shock wave generated by explosion of a 10 mg AgN_3 pellet ignited at L = 30 mm above PDMS/water interface, Tw = 296.6 K: **a** #90101802, 38.2 μs from ignition; **b** #90101804, 42.0 μs; **c** #90101809, 47 μs; **d** #90101807, 61.2 μs; **e** #90101811, 90.5 μs; **f** #90101810, 96.7 μs

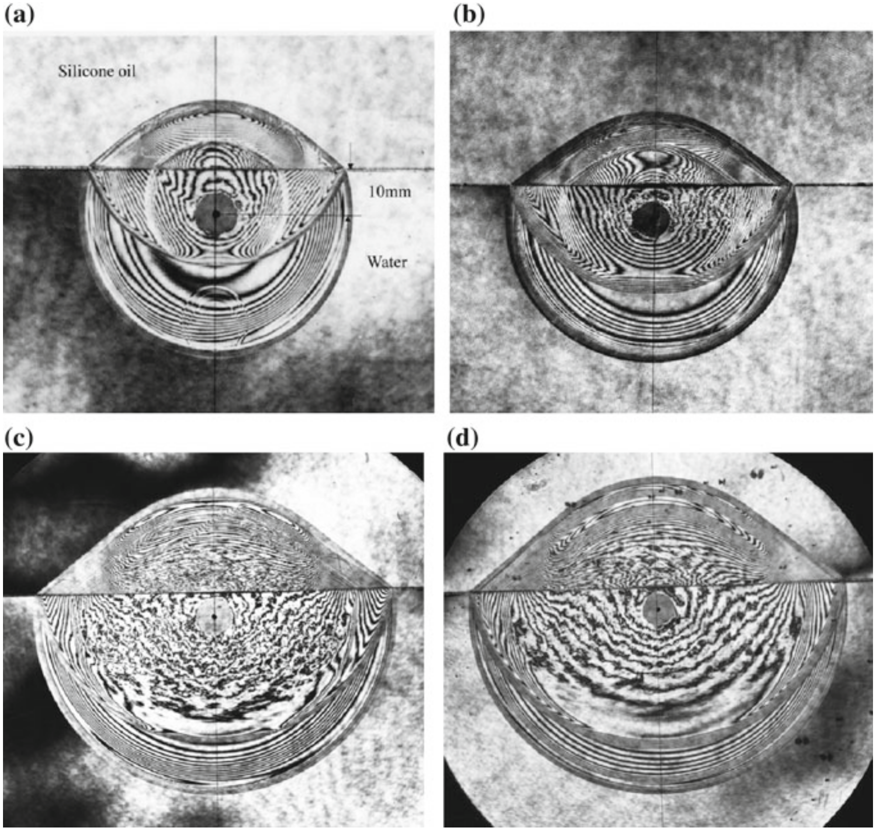

Fig. 9.13 Micro-explosion of 10 mg AgN_3 pellet at L = 10 mm below PDMS/water interface: **a** #92121507, 20 μs from ignition, see the generation of a secondary shock wave; **b** #92120806, 28 μs; **c** #92120904, 48 μs from ignition; **d** #92121504, 63 μs

exposure interferograms taken in the same condition as in Fig. 9.14a–d but L—10 mm. The difference in the magnitude of the stand-off distance, L does-not significantly affect the waves interaction.

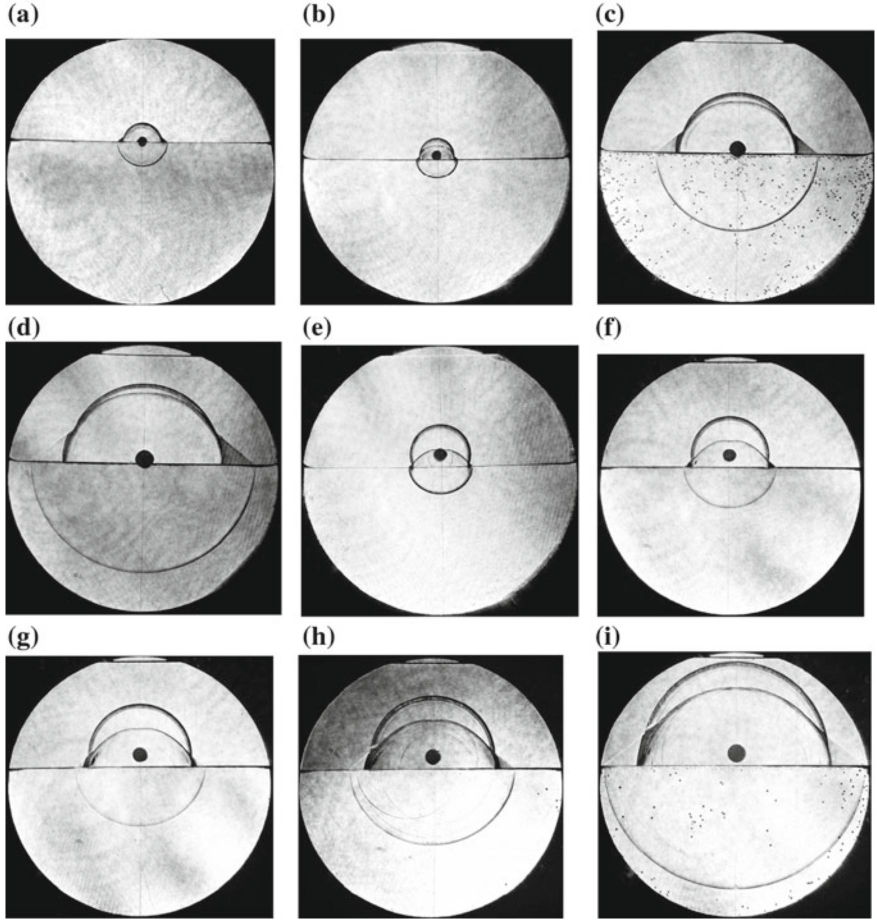

Fig. 9.14 Single exposure interferograms showing the interaction of 1cSt PDMS/water interface with shock waves generated by explosion of 8.7–9.0 mg AgN_3 pellets; **a**–**d** L = 3, **e**–**i**: L = 10 mm at 292.0 K: **a** #93102501, AgN_3 pellets, L = 3 mm; **b** #93102502, AgN_3 pellets, L = 3 mm; **c** #93102503, 8.7 mg AgN_3 pellets, L = 3 mm, L = 3 mm; **d** #93102504, L = 3 mm, 9.0 mg AgN_3pellet; **e** #93102506, L = 10 mm, 9.0 mg AgN_3 pellet; **f** #93102602, L = 10 mm, 9.0 mg AgN_3pellet; **g** #93102601, L = 10 mm, 8.9 mg AgN_3 8.9 mg; **h** #93102507, L = 10 mm, 8.1 mg AgN_3; **i** #93102804, L = 10 mm, 8.1 mg AgN_3

9.4 Underwater Shock Wave Focusing

An ellipsoid has two focal points. Hence a linear wave, for example, a sound wave or a light emitted at one of its focal points is reflected from the ellipsoidal wall and converges at its second focal point. A micro explosion placed at the first focal point creates a spherical shock wave, which focuses almost at the second focal point. The shock wave focuses at a point slightly deviated from the second focal point because the underwater shock wave interacts with the detonation product gas and cavitation phenomena perturb the shock wave propagation. Nevertheless, the deviation from proper focusing between linear waves and micro-explosion driven shock waves is negligibly small.

9.4.1 Two-Dimensional Elliptical Reflectors

Focusing of an underwater shock wave inside an elliptic cavity is discussed subsequently. Figure 9.15 shows the elliptic reflector used for visualization. The elliptical reflector has a minor radius of 45 mm and a major radius of 63.5 mm, ratio of the radii is square root of 2. The reflector is made of a 10 mm thick brass plate and sandwiched by two 15 mm thick acrylic plates.

The elliptical reflector shown in Fig. 9.15 is a two-dimensional test section. It was filled with water and a 4 mg PbN_6 pellet was glued on the edge of a 0.6 mm core diameter optical fiber at one of the focal points of elliptic reflector and detonated. The resulting shock wave became a cylindrical shock wave after repeated reflections between the two acrylic plates. The cylindrical shock wave propagated and eventually focused at another focal point (Shitamori 1990).

The time passed from ignition and until reaching complete the focusing took about 83 μs. Figure 9.16 shows sequential observations of the focusing process,

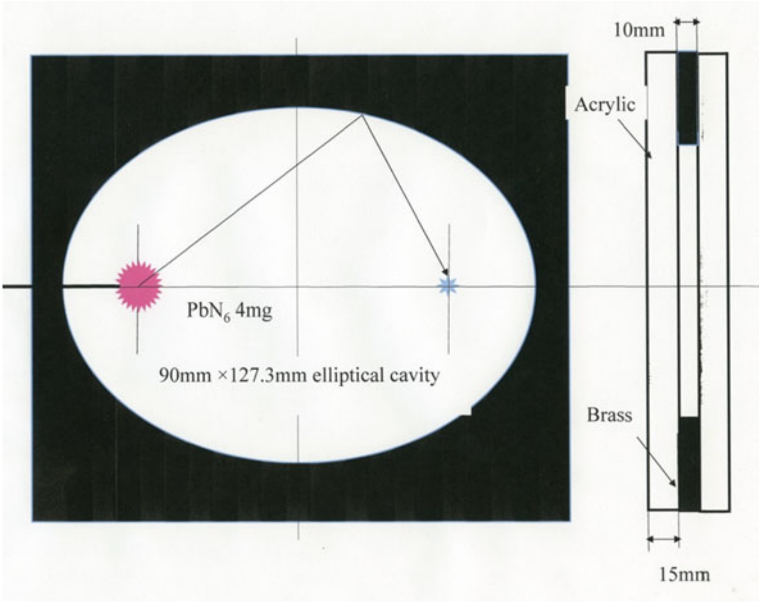

Fig. 9.15 Elliptical reflector, minor diameter 90 mm × major diameter 127.3 mm

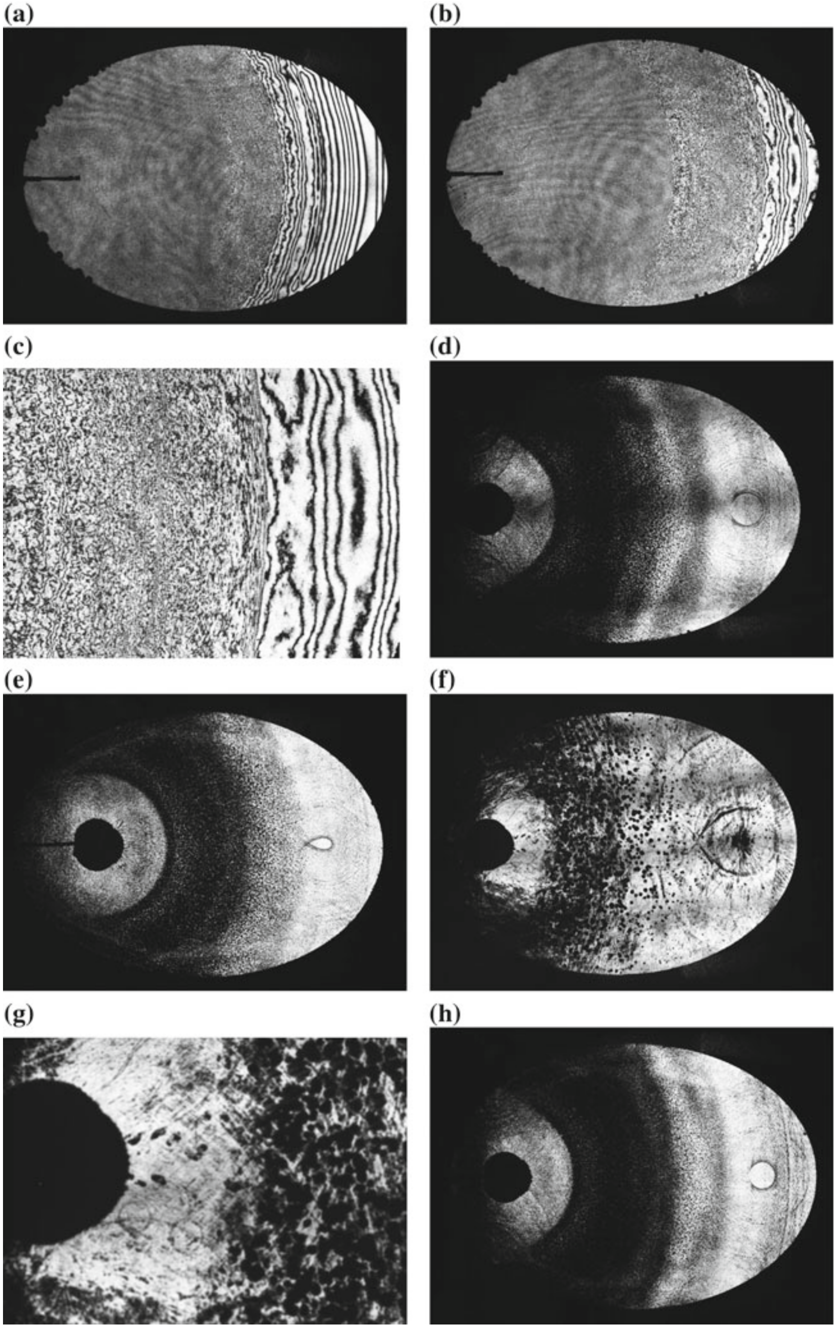

Fig. 9.16 Sequential observation of shock wave focusing in an elliptic cavity: **a** #87101502, 48 µs from explosion; **b** #87101503, 60 µs; **c** enlargement of (**b**); **d** #87101506, 65 µs; **e** 87101903, 73 µs; **f** #87101501, 83 µs; **g** enlargement of (**f**); **h** 87101605, 85 µs; **i** #87101606, 86 µs; **j** #87101710. 98 µs

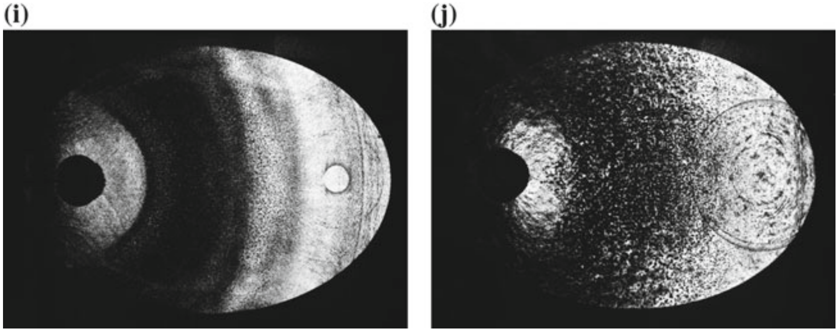

Fig. 9.16 (continued)

in particular the later stage of focusing. The overpressure measured at 5 mm from the center of point explosion was over 50 MPa hence such a sudden high-pressure loading deformed outward the acrylic plate spontaneously probably for less than a few µm. Such sudden deformations generated a strong tensile force in water and induced cavitation. Figure 9.16a, b shows double exposure interferograms. Fringes show stress waves in the acrylic plates and a grey region indicates cavitation bubble cloud. The other images in Fig. 9.16 are single exposure interferogram that are equivalent to shadowgraph. Dark regions show cavitation clouds. Figure 9.16c shows enlargement of Fig. 9.16b. Fine structure of bubbles are visible in these images. Figure 9.16g shows the enlargement of f. Small rings correspond to secondary shock waves created when the cavitation bubbles collapsed. The evolution of focusing of the reflected shock waves was clearly observed.

9.4.2 Shallow Spherical Reflectors

9.4.2.1 Concentric Circular Reflector

A 4 mg PbN_6 pellet was exploded at the center of a 50 mm diameter shallow concentric reflector of 70 mm in diameter. The resulting spherical shock wave was reflected from the reflector. The sequential interferograms (Esashi 1983) and their comparison with unreconstructed images, equivalence to direct shadowgraphs, are shown in Fig. 9.17.

The energy recovery efficiency measured at the focal point is defined as the ratio of energy carried in the reflected wave to that contained in the direct wave, which is the solid angle of the reflector viewed from the point of the explosion normalized by 4π. Then the efficiency of a 50 mm diameter concentric reflector which is composed of 70 mm diameter sphere as shown in Fig. 9.17a, is about 14%. In other words, about 14% of energy was recovered at the focal point.

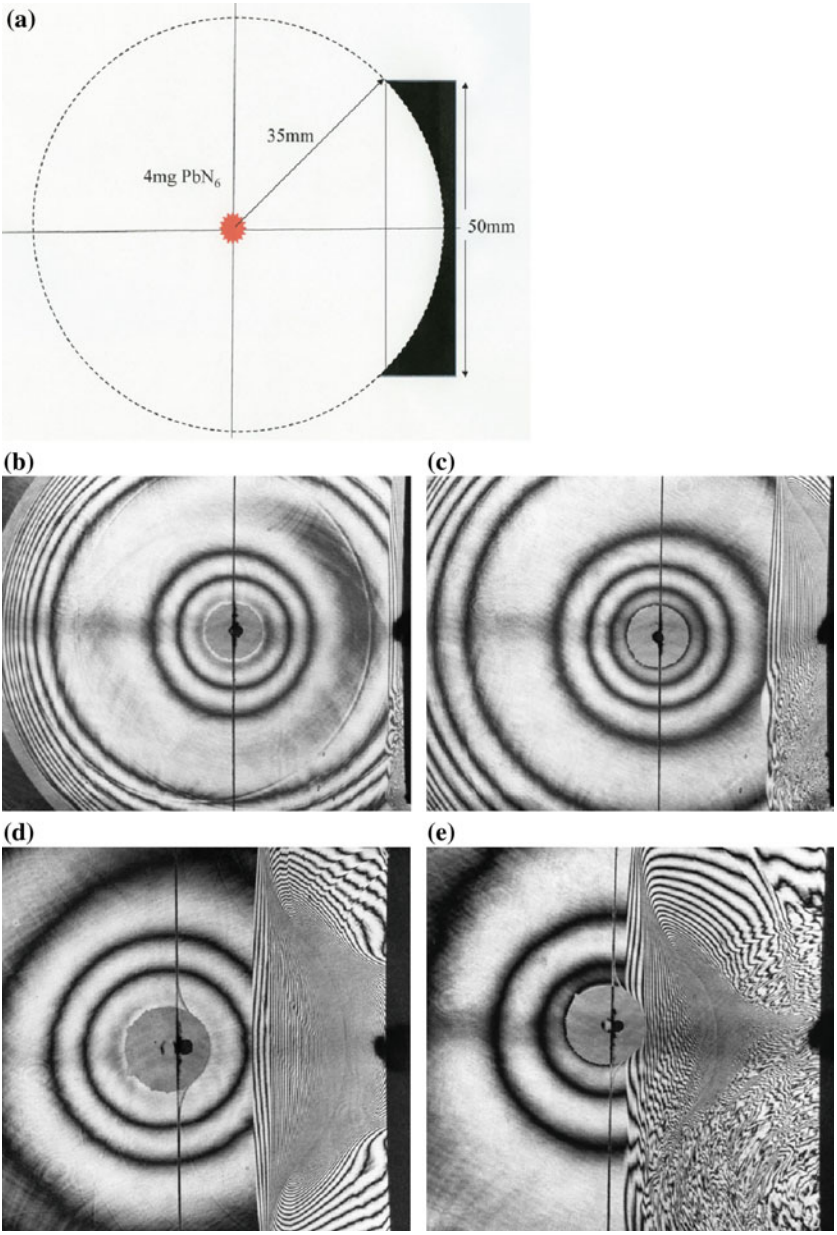

Fig. 9.17 Shock wave focusing from a 50 mm reflector PbN$_6$ 4 mg at 287 K: **a** experimental setup; **b** #82121707, elapsed time 2.5 μs from the exit; **c** #82121706, 4.8 μs; **d** #82121715, 11 μs; **e** #82121710, 15 μs; **f** #82121713, 21 μs; **g** unreconstructed image of (**f**); **h** #82122007, 27 μs; **i** unreconstructed image of (**g**); **j** #82122010, 29 μs; **k** unreconstructed image of (**j**); **l** #82122011, 33 μs; **m** unreconstructed image of (**l**) (Esashi 1983)

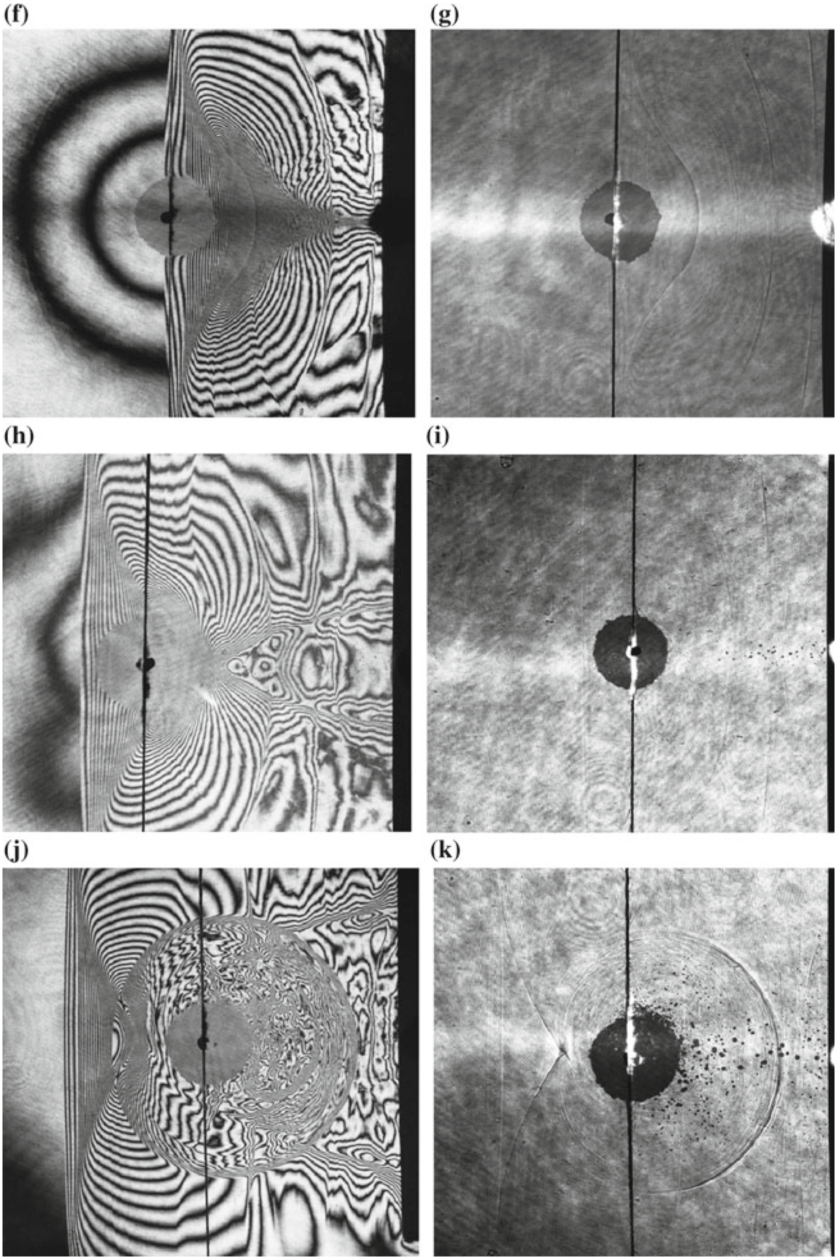

Fig. 9.17 (continued)

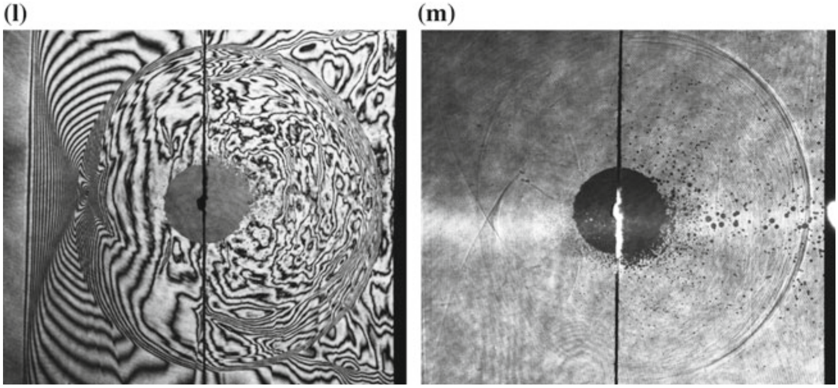

Fig. 9.17 (continued)

Figure 9.17g, i, k are unreconstructed interferograms which are equivalent to direct shadowgraphs. Double exposure interferograms describe quantitatively the density variation but sometimes the inception of cavitation bubbles are difficult to identify. The shock wave reflected from a concentric circular reflector moved toward the position at which the micro-explosive was ignited. Therefore, the shape of the reflected shock wave was concentric with the detonation product gas bubble which was expanding spherically. When the reflected shock wave approached to the spherical detonation product gas sphere, the spherical shock wave interacted with a water/gas interface. Then bubble clouds were generated along the center axis as seen in Fig. 9.17g, i, k. The detonation product gas bubble having a slightly irregular spherical shape was slowly expanding. At the same time, the reflected shock wave impinged, at first, on the bubble and converged toward the center of the bubble. Figure 9.17h, i shows the moment of convergence. In Fig. 9.18j, k, m, the frontal surface of the detonation product gas bubble bulged and bubble clouds were generated.

9.4.2.2 Shallow Eccentric Circular Reflectors

Figure 9.18a shows a reflection of shock wave generated by exploding 4 mg PbN_6 pellet at 50 mm away from a 35 mm radius circular shallow reflector. If a spherical sound wave is emitted at this off-centered point, the sound wave will focus at the conjugate focal point of this reflector.

Figure 9.18 shows the evolution of the shock wave reflected from the shallow reflector at 50 mm away from the 35 mm radius reflector. As seen in Fig. 9.18b–g, the reflected shock wave is converging at the position closer to the reflector (Esashi 1983).

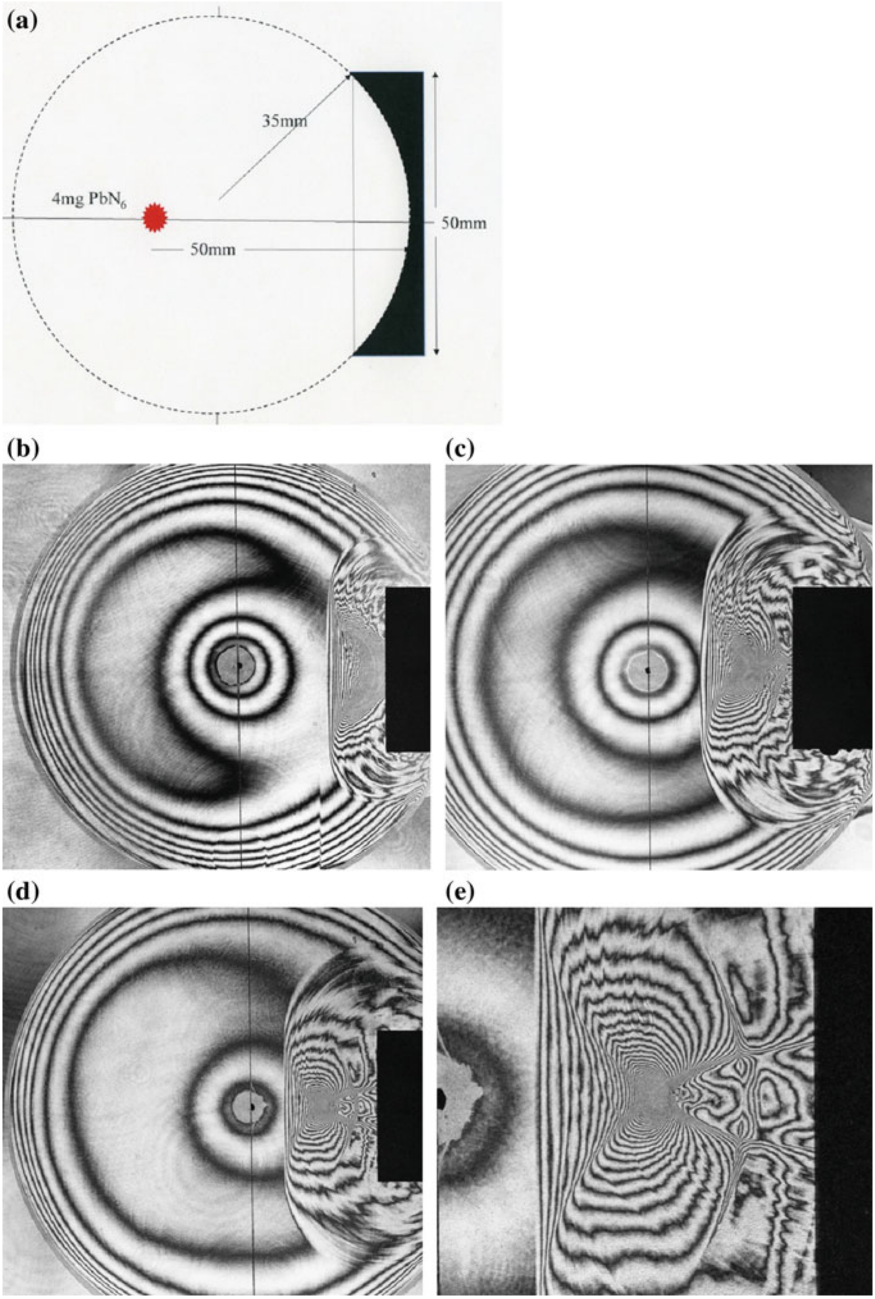

Fig. 9.18 Focusing of shock wave generated by exploding a 4 mg PbN_6 pellet at 50 mm from the reflector at 287 K: **a** experimental setup; **b** #83011906; **c** #83011907; **d** #83011905; **e** enlargement of (**d**); **f** #83011908; **g** enlargement of (**f**)

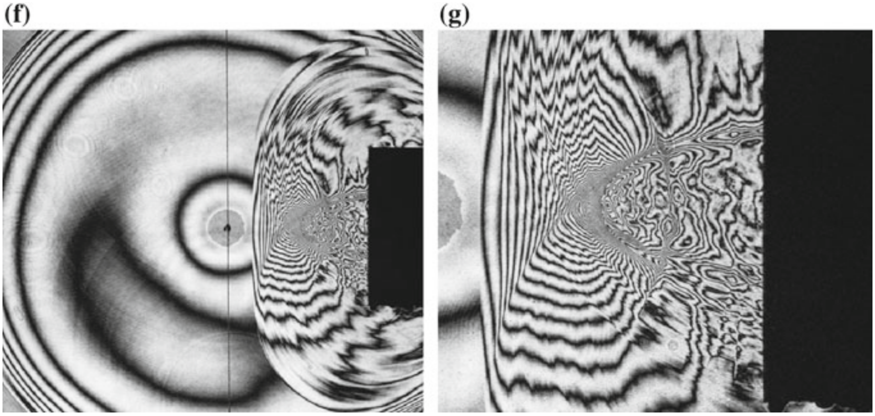

Fig. 9.18 (continued)

Figure 9.19a shows a reflection of shock wave generated by exploding a 10 mg PbN_6 pellet at the off-centered position at the 30 mm away from the 35 mm radius circular shallow reflector and 25 mm aside position. Figure 9.20b–e shows the evolution of the shock wave reflection from the shallow reflector and focusing at the off-centered position (Esashi 1983).

Figure 9.20a shows a reflection of shock wave generated by exploding a PbN_6 10 mg pellet at the 40 mm distance from the 35 mm radius circular shallow reflector and 25 mm aside position. Figure 9.20b–e shows sequential observation of focusing occurring at the conjugated point of the explosion center (Esashi 1983).

Figure 9.21a shows a reflection of shock wave generated at the off-centered position by exploding a 9 mg PbN_6 pellet at 50 mm away from the 35 mm radius circular shallow reflector and 25 mm aside position. Figure 9.21b–e shows focusing occurring at the conjugated point of the explosion center (Esashi 1983).

Figure 9.22a shows the reflection of shock wave generated by exploding a 9 mg PbN_6 pellet at 100 mm away from the 35 mm radius circular shallow reflector and 25 mm aside position. Figure 9.22b–g shows sequential interferograms. The reflected shock wave merges at a neighborhood to the conjugated focal point. However, the fringes coalesce not necessarily as sharply as what observable in Fig. 9.22 (Esashi 1983).

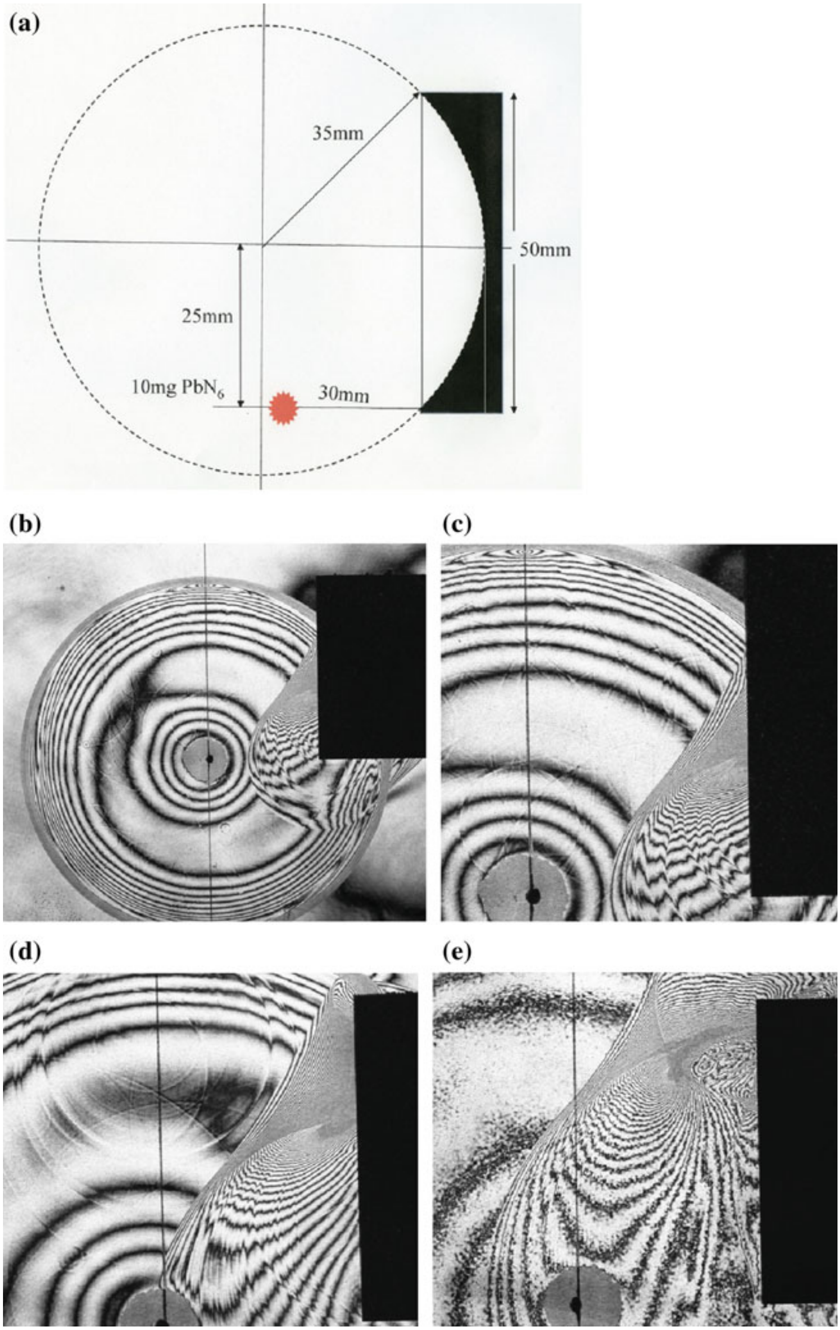

Fig. 9.19 Focusing of shock wave generated by exploding 10 mg PbN$_6$ pellet at 30 mm away from the 35 mm radius reflector and 25 mm aside position at 280.3 K: **a** experimental setup; **b** #84030909; **c** enlargement of (**b**); **d** #84030911; **e** #84030916

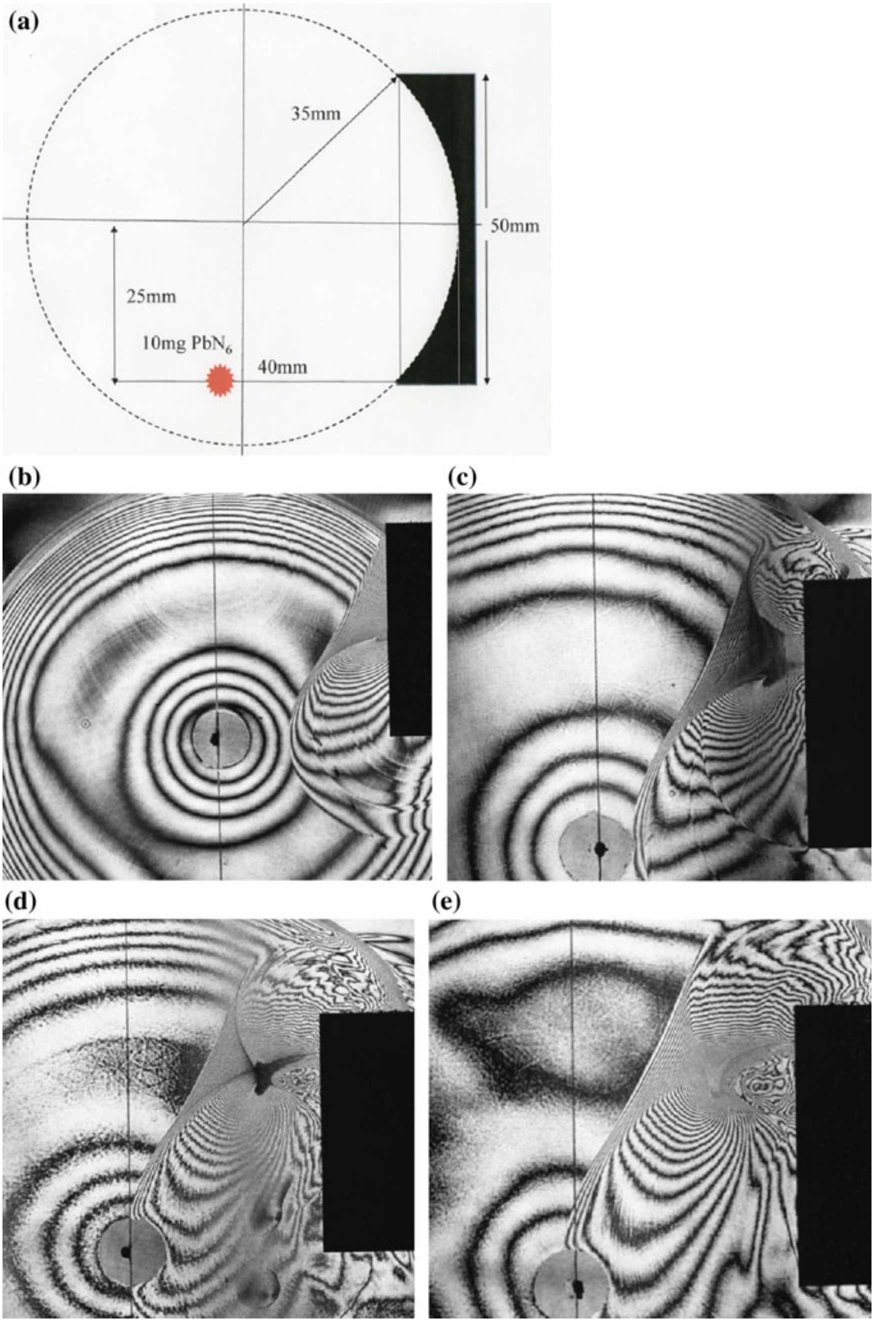

Fig. 9.20 Focusing of shock wave generated by exploding a 10 mg PbN_6 pellet at 40 mm from the reflector and 25 mm aside position: **a** experimental setup; **b** #84030902; **c** #84030907; **d** #84030908; **e** #84030905

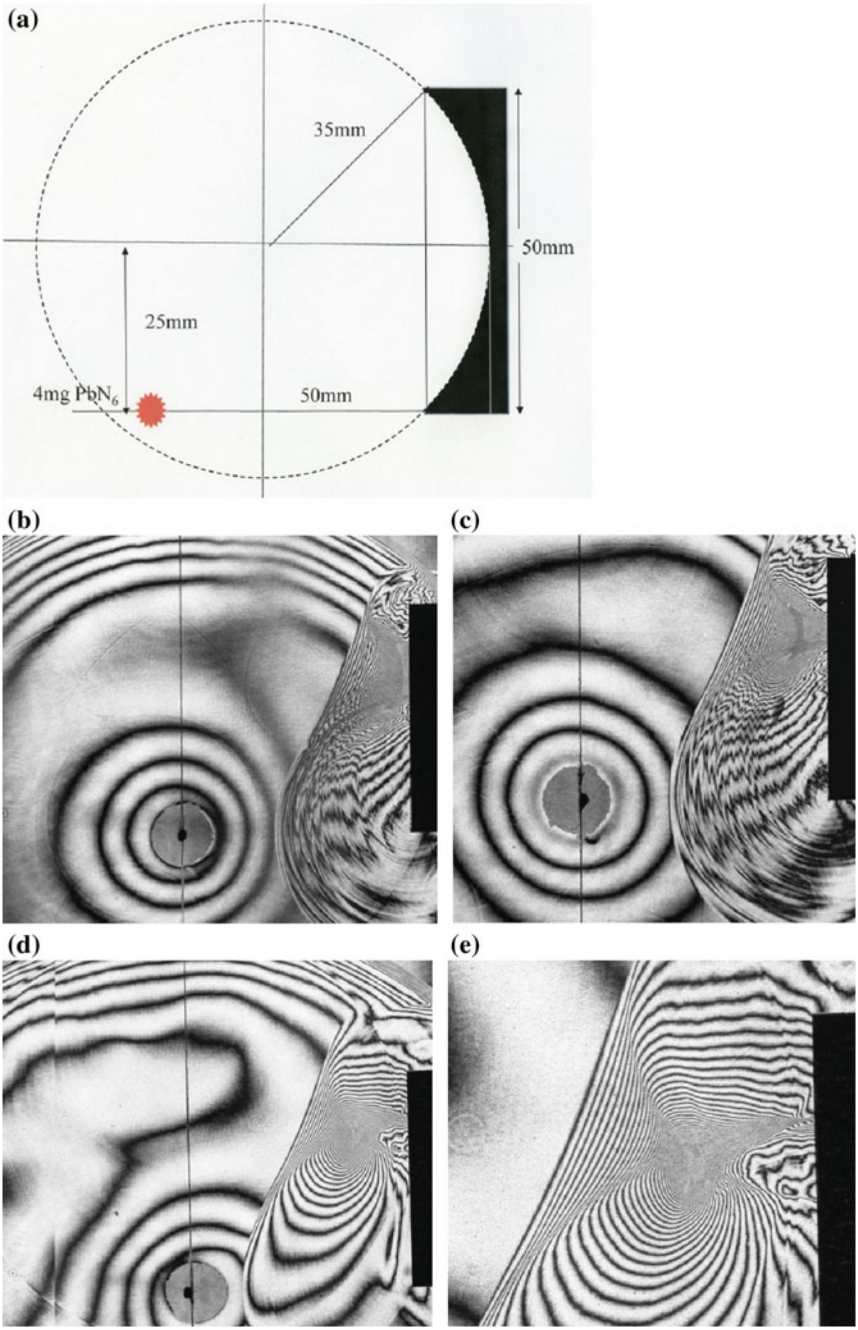

Fig. 9.21 Focusing of shock wave generated by exploding a 9 mg PbN$_6$ pellet at 50 mm away from reflector and 25 mm aside position, at 285 K: **a** experimental setup; **b** #8403081; **c** #84030812; **d** #84030901; **e** enlargement of (**d**)

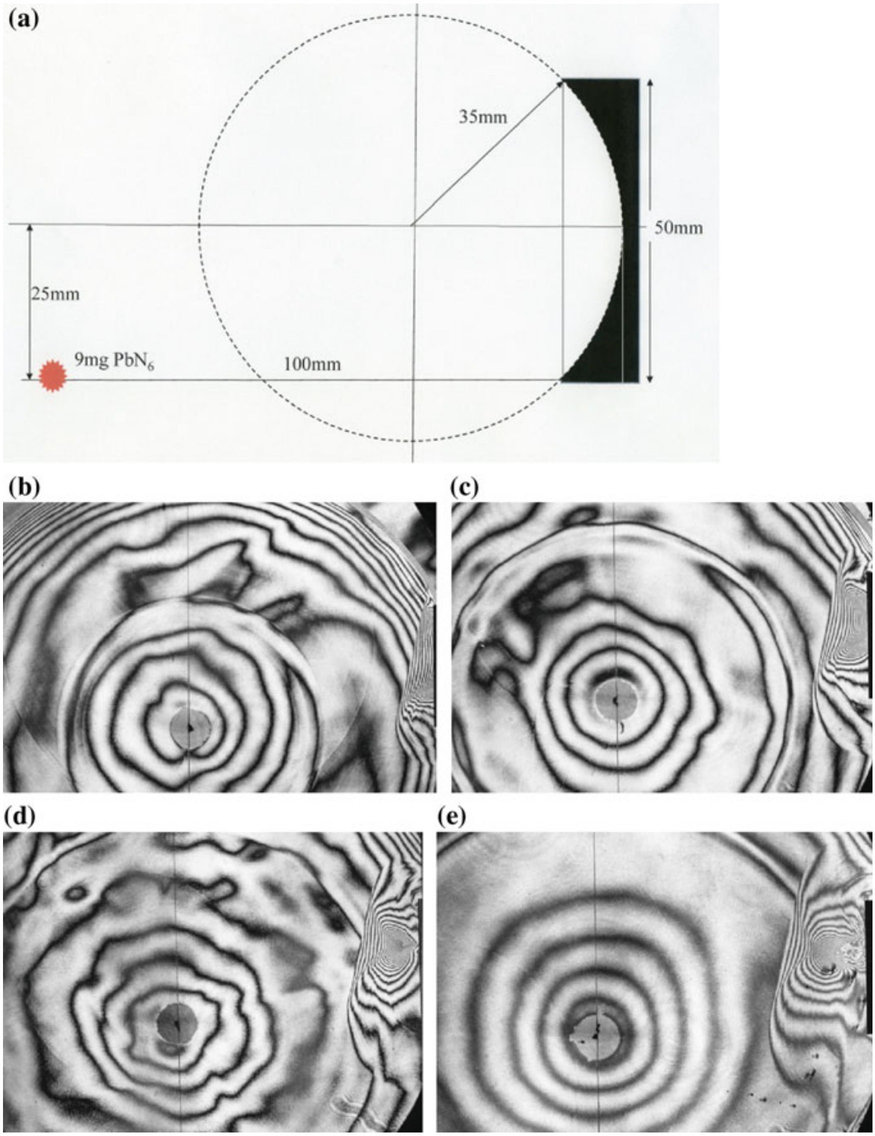

Fig. 9.22 Focusing of shock wave generated by exploding a 9 mg PbN$_6$ pellet at 100 mm away from the reflector and 25 mm aside position: **a** experimental setup; **b** #84031209; **c** #84031210; **d** #84031211; **e** #84031215; **f** enlargement of (**e**)

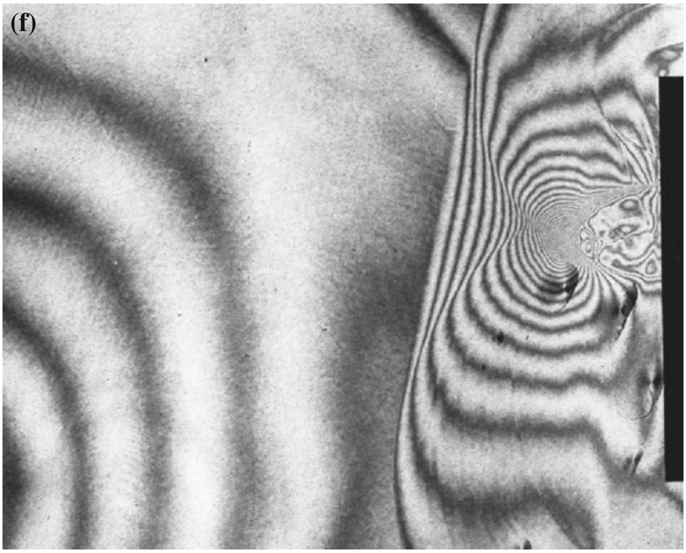

Fig. 9.22 (continued)

9.4.3 Shallow Circular Reflectors from 100 mm from the Explosion Point on the Center Line

Figure 9.23a shows the reflection of a shock wave generated by exploding a 4 mg PbN_6 pellet installed at 100 mm from the reflector. Figure 9.23b–k shows the evolution of the focusing of the reflected shock wave generated by explosion of PbN_6 4 mg from the 50 mm diameter reflector.

9.4.4 Shallow Ellipsoidal Reflector

Figure 9.24a shows a truncated 90 mm × 128 mm ellipsoidal reflector. A spherical shock wave generated by exploding a 4 mg PbN_6 pellet placed at the first focal point outside the truncated reflector is focused at the second focal point close to the reflector. Figure 9.24b–m shows the evolution of the shock wave focusing. In Fig. 9.24, fringe distributions show the whole sequence of propagation, reflection and focusing of the spherical shock wave (Esashi 1983).

As seen in Fig. 9.24, when a spherical shock wave is generated at the first focal point of the truncated 90 mm × 128 mm ellipsoidal reflector, the part of the diverging shock wave is recovered by focusing from the 50 mm diameter reflector. Only a 1.2% of the energy carried by the shock wave energy is recovered. If the shock wave would have been generated at a focal point inside a truncated

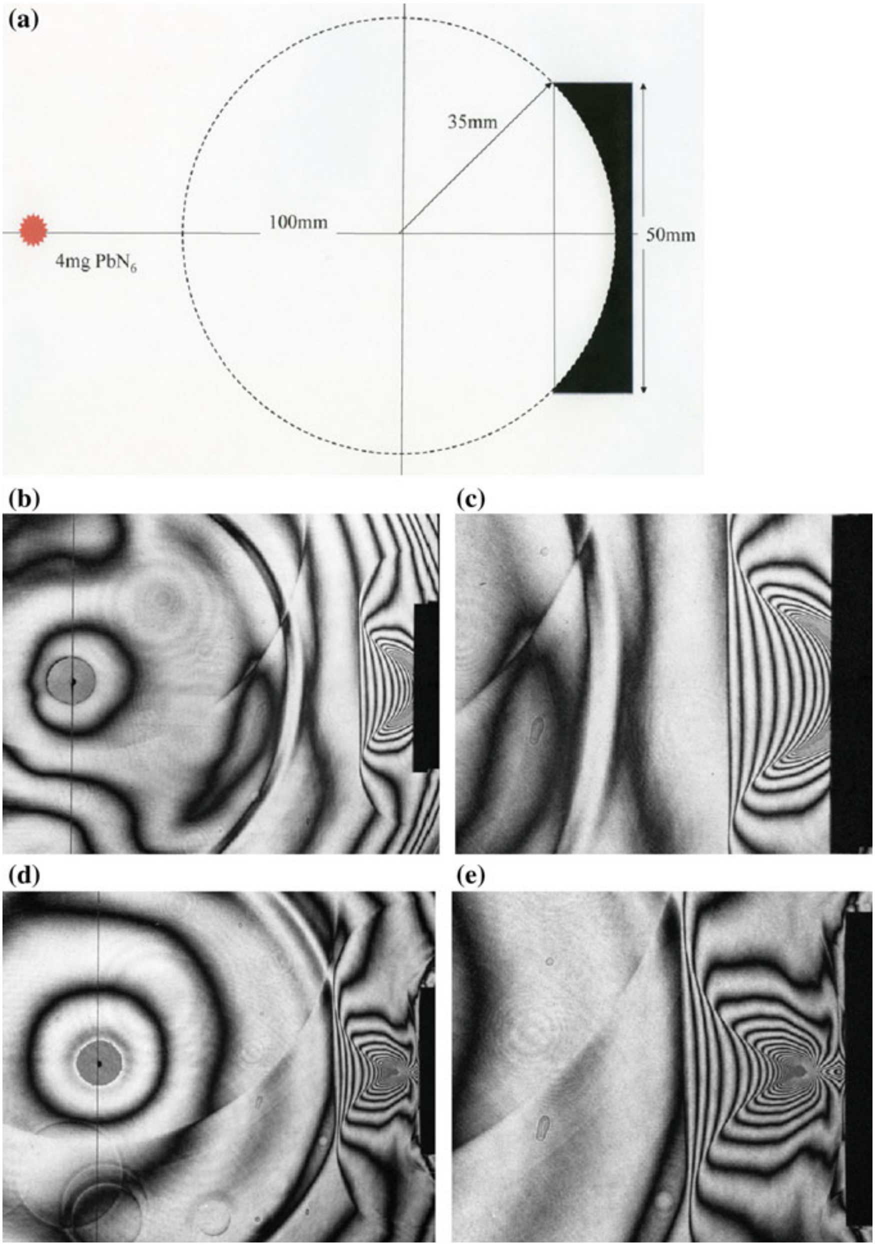

Fig. 9.23 Shallow circular reflectors from 100 mm away from point explosion on the center line, 4 mg PbN_6: **a** experimental setup; **b** #83012122; **c** enlargement of (**b**); **d** #83012103; **e** enlargement of (**d**); **f** #83012104; **g** enlargement of (**f**); **h** #83012105; **i** enlargement of (**h**); **j** #83012108

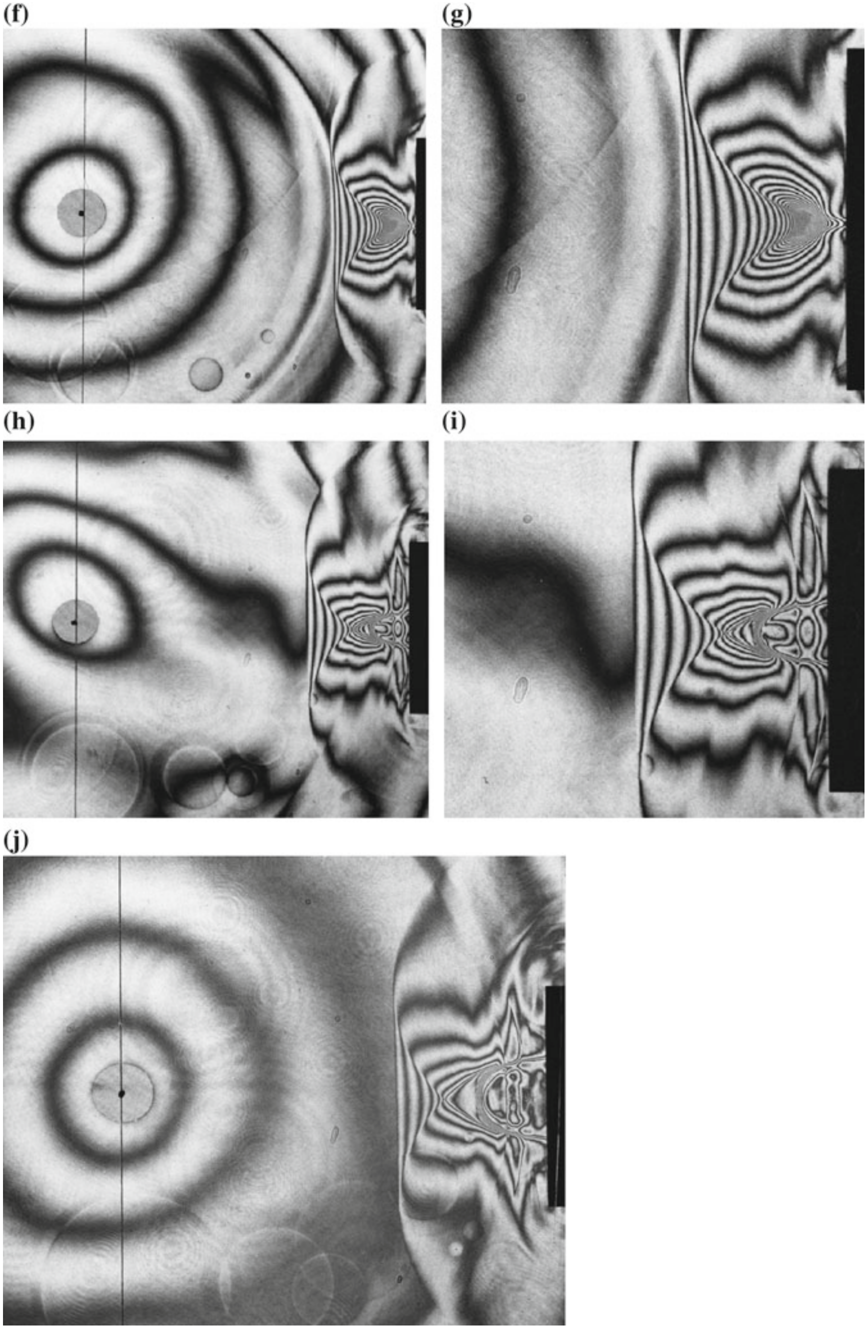

Fig. 9.23 (continued)

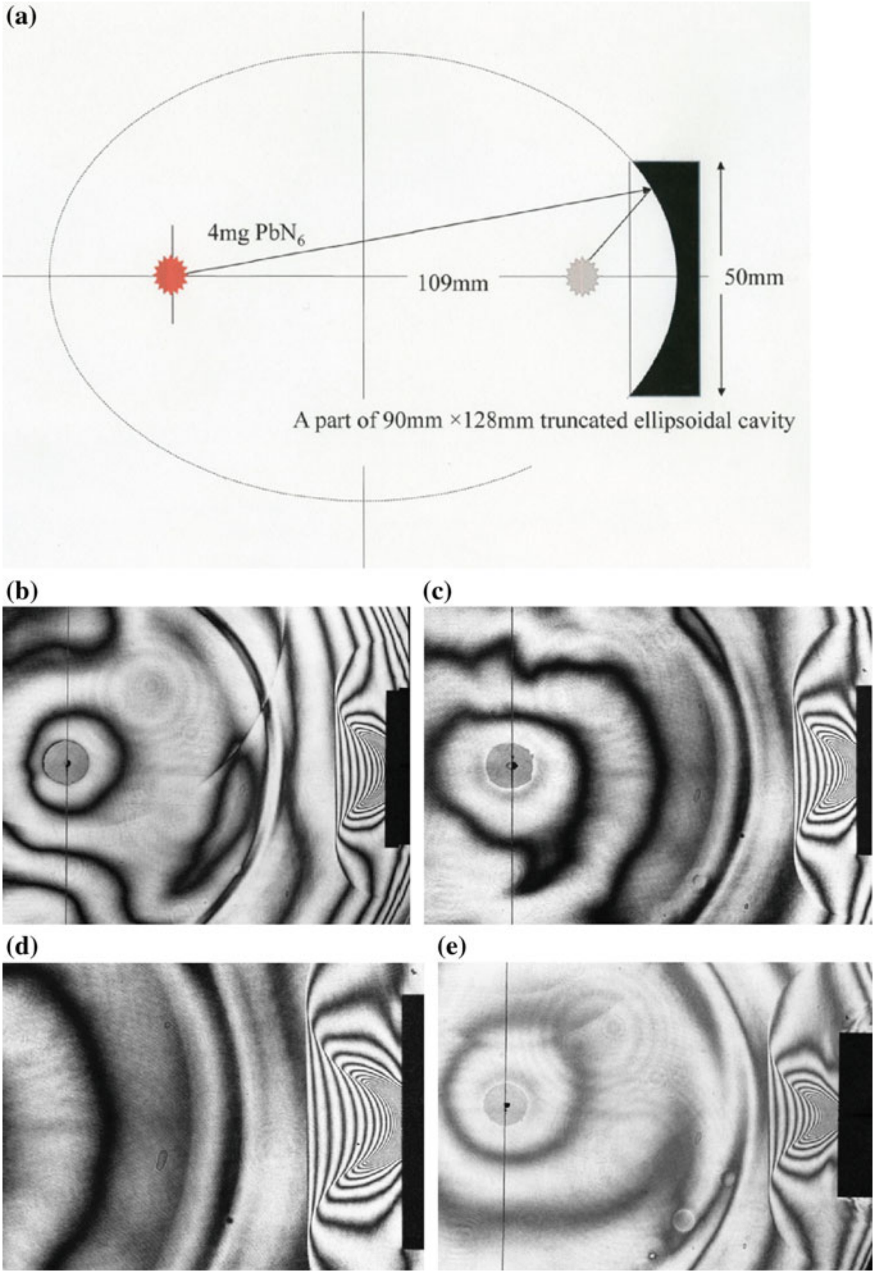

Fig. 9.24 Shock wave generation at the first focal point of a truncated 90 mm × 128 mm ellipsoidal reflector by exploding a 4 mg PbN_6 pellet and its focusing at the second focal point: **a** experimental setup; **b** #83012122; **c** #83012121; **d** enlargement of (**c**); **e** #83012120; **f** #83012103; **g** #83012104; **h** enlargement of (**g**); **i** #83012105; **j** #83012128; **k** enlargement of (**j**); **l** #83012123; **m** enlargement of (**l**)

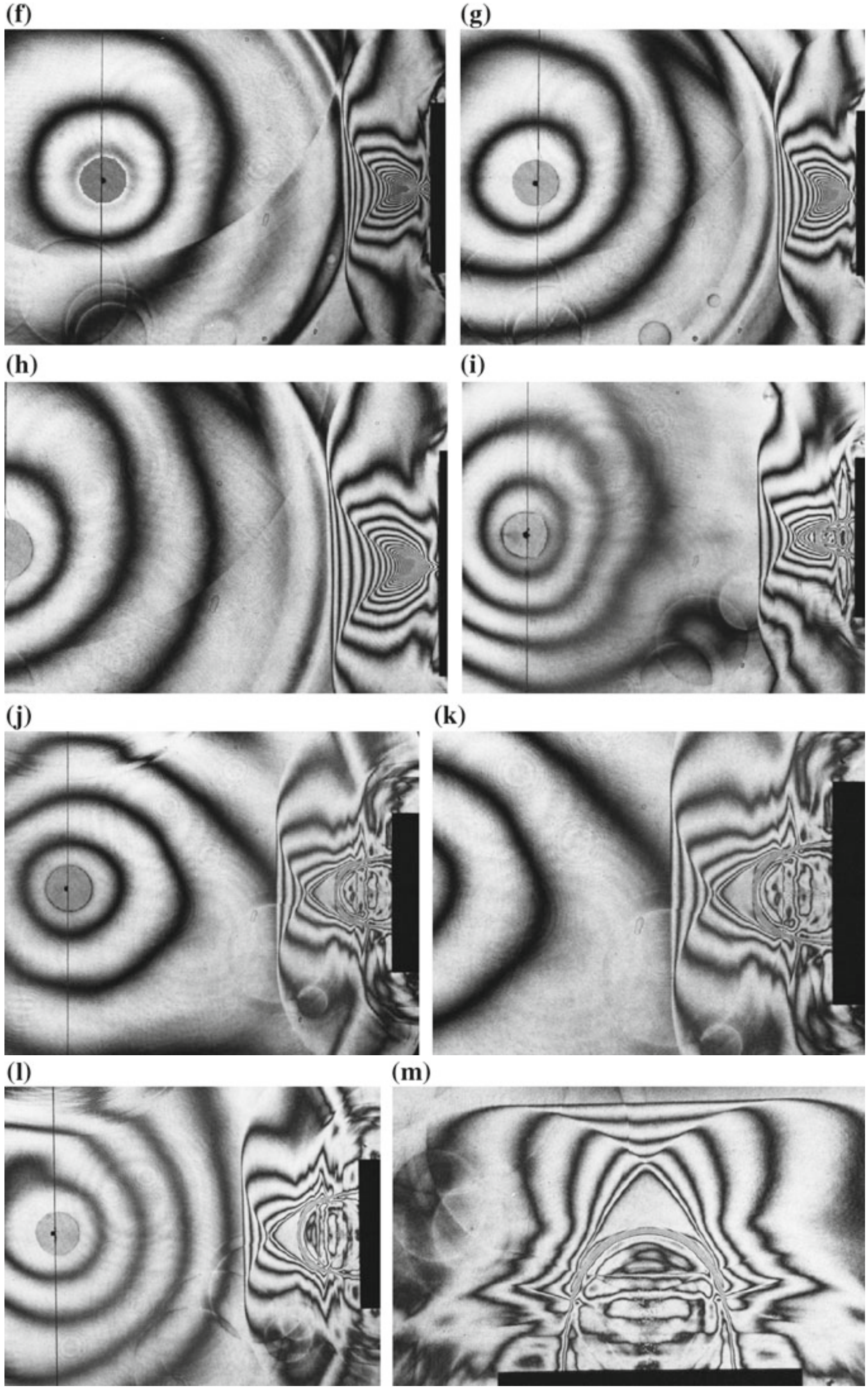

Fig. 9.24 (continued)

ellipsoidal cavity of the same geometry, the rate of energy recovered at the second focal point would have been much higher than this value (Esashi 1983).

9.4.5 Deep Ellipsoidal Reflectors

9.4.5.1 Diffuse Holographic Observation of Truncated Acrylic Reflector

When the shock wave is generated at a focal point inside a truncated 90 mm 128 mm ellipsoidal reflector, the reflected shock wave is focused at the second focal point outside the reflector. To visualize the wave motion inside the reflector, the truncated reflector was made of acryl and was visualized the wave motion using diffuse holographic interferometry, in which diffuse *OB* passed the transparent test section. The diffuse *OB* passed through the transparent reflector and carried holographic information onto the holographic film. Combining the optical arrangement with that of shadowgraph, the change in phase angles between the double exposures can be recorded as image holograms. A spherical shock wave was generated by exploding PbN_6 pellet attached on the edge of optical fiber and was inserted through a thin hole at the end wall of the reflector as shown in Fig. 9.25a.

A direct shock wave was released from the opening. The rest of the shock wave was transmitted into the acrylic reflector. For the given ratio of the acoustic impedance between the acryl and water, assuming, for the sake of simplicity one-dimensional waves, the ratio of the transmitted wave energy I_t to the incident wave energy I_i and the ratio of the reflected shock energy I_r to I_i. $I_t/I_i = 4\mathrm{m}_1\mathrm{m}_2/(\mathrm{m}_1 + \mathrm{m}_2)^2$, $I_r/I_i = (\mathrm{m}_2 - \mathrm{m}_1)^2/(\mathrm{m}_1 + \mathrm{m}_2)^2$, where m_1 and m_2 are acoustic impedance of acryl and water, respectively. However, this relation is valid only to one linear waves.

For reference, as stress waves in acryl propagate at 2.9 km/s and its density being 1.18, then the ratio $\mathrm{m}_{\mathrm{acryle}}/\mathrm{m}_{\mathrm{water}}$ is 2.28 and hence $I_r/I_i = 0.152$ and $I_t/I_i = 0.848$. A fraction of energy is reflected into the acryl. In Fig. 9.25, a transmitted shock wave in acryl is visible as a discontinuous grey line. Compression stress waves in acryl are released into the water as grey lines. The dark irregularly shaped circle at the focal point inside the reflector is a detonation product gas. The direct wave passes outside through the opening, whereas the rest of waves is reflected from the curved wall and converges toward the second focal point. Vague grey shadows along the center axis visible in Fig. 9.25g–j are bubble clouds.

9.4.5.2 Focusing from a Truncated Ellipsoidal Cavity Made of Brass

Spherical shock waves created at a focal point inside a truncated 90 mm × 128 mm ellipsoidal reflector are focused at the second focal point outside the reflector and fringe concentration at the second focal point was observed. Figure 9.26a–l

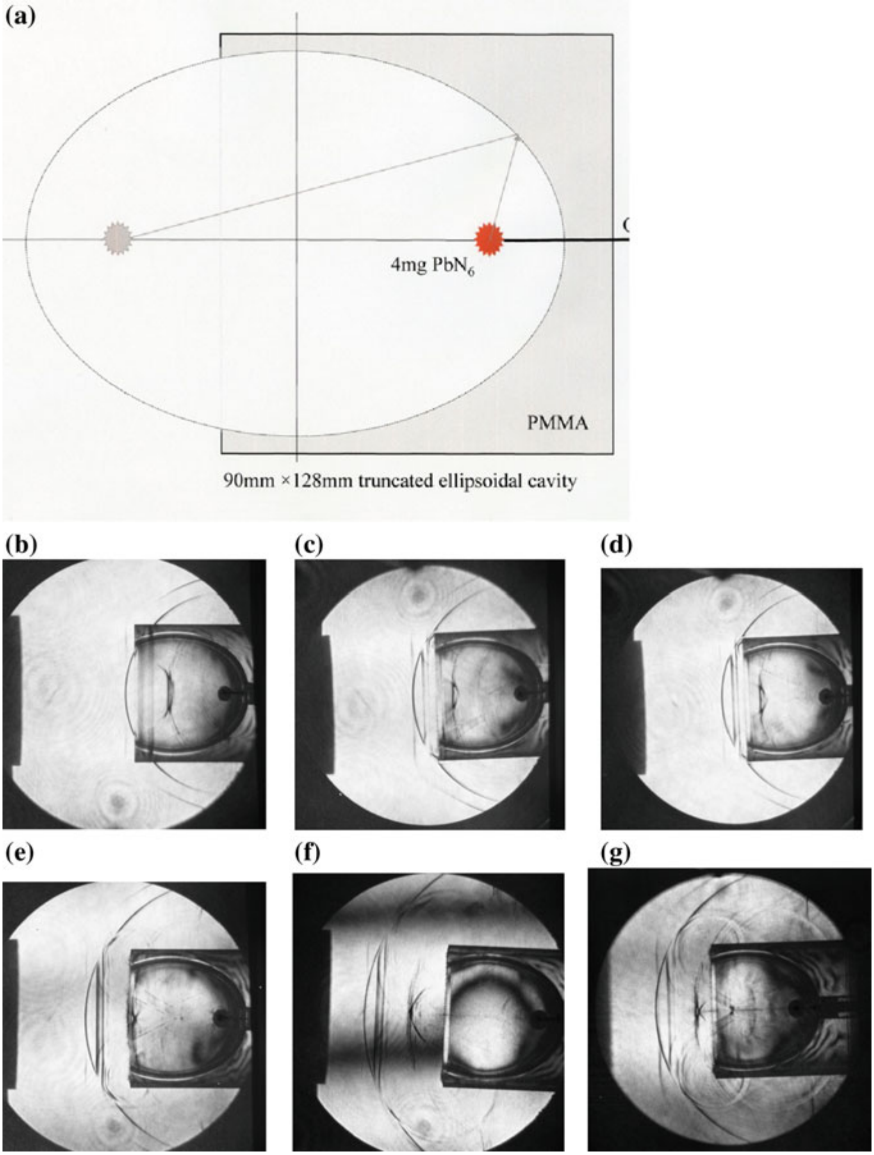

Fig. 9.25 Shock wave focusing from a deep reflector made of acryl, PbN$_6$ pellets weighing from 11.7 to 12.8 mg: **a** experimental setup; **b** #83070406, 55 μs from trigger point; **c** #83070405, 60 μs: **d** #83070404, 65 μs; **e** #83070503, 70 μs; **f** #83070403, 75 μs; **g** 83071317, 80 μs; **h** 83071204, 86 μs; **i** 83071314, 90 μs; **j** 83071302, 96 μs

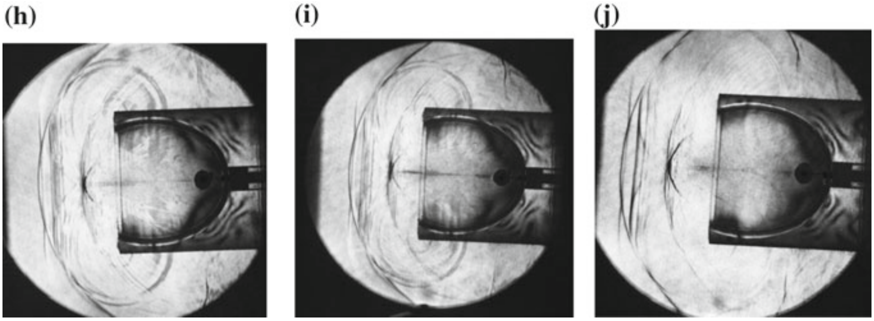

Fig. 9.25 (continued)

show sequential double exposure interferograms of shock wave focusing from a 90mm ×128mm truncated ellipsoidal reflector made of brass. When a 3.7mg to 5.6mg PbN6 pellet was ignited at the focal point inside the reflector, the direct shock wave came out first. Then the resulting reflected shock wave gradually focused at the focal point outside the reflector.

9.4.5.3 Shock Wave Focusing in a Closed Ellipsoidal Reflector

A stainless steel ellipsoidal reflector 500 mm × 700 mm and 100 mm wall thickness was manufactured (Takayama 1990). Figure 9.27a shows a schematic diagram of the ellipsoidal reflector. Figure 9.27b is a photograph of the facility. Figure 9.27c shows a PETN pellet supported by a thin optical fiber and placed at one of the focal points. The total weight of explosives including a PETN pellet and an igniter was well over 110 mg so that the reflector wall was very thick which was expected to withstand the high pressure and also to minimize the wall deformation. However, many pin holes were found densely populated on the upper part of the reflector. These pit holes were created due to cavitation erosion which were induced by disappearance of high pressure in very short time.

The PETN pellets had a cylindrical shape and had a 2 mm diameter hole as shown in Fig. 9.27c. A 10 mg AgN_3 pellet glued on the edge of 0.6 mm core diameter optical fiber was an igniter and inserted into the hole. The transmission of a Q-switch Nd:YAG laser beam through the optical fiber ignited the AgN_3 pellet and simultaneously exploded the PETN. The resulting spherical shock wave was so far generated inside the ellipsoidal cavity and focused at another focal point. The pressures at the focal point was measured with PVDF (poly vinyl denefluoride) pressure transducers manufactured in house. The pressure transducers were calibrated by comparison with Kistler pressure transducers Model 601H. Measured pressure history along the center axis recorded by the home-made transducers were compared with those obtained from the Kistler pressure gauge.

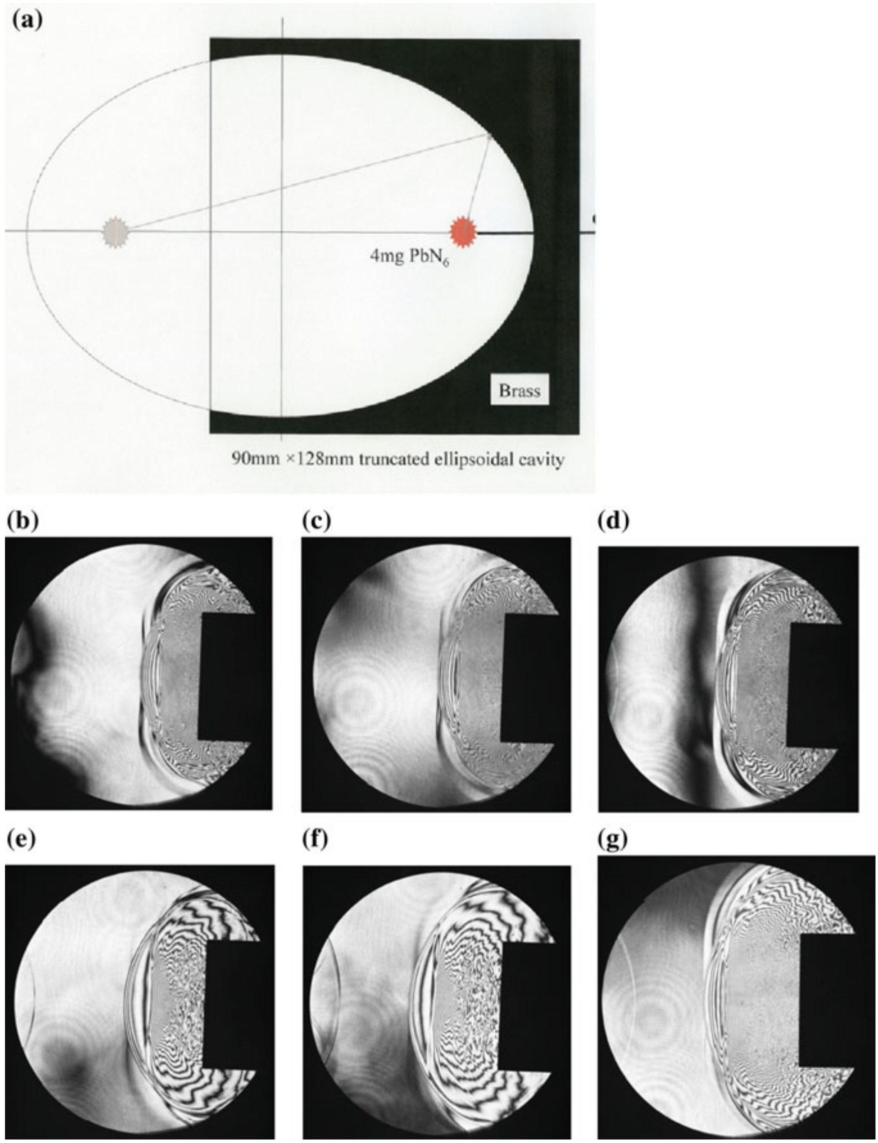

Fig. 9.26 Shock wave focusing from a truncated 90 mm × 128 mm ellipsoidal reflector made of brass. Shock waves were generated by exploding PbN_6 pellet weighing from 3.7 to 5.6 mg: **a** #83090710, 65 μs; **b** #83090709, 70 μs; **c** #83090708, 75 μs; **d** #83090707, 80 μs; **e** #83090706, 86 μs; **f** #83090705, 88 μs; **g** #83090704, 90 μs; **h** #83090703, 92 μs; **i** #83090702, 95 μs; **j** #83090701, 100 μs; **k** #83090607, 105 μs

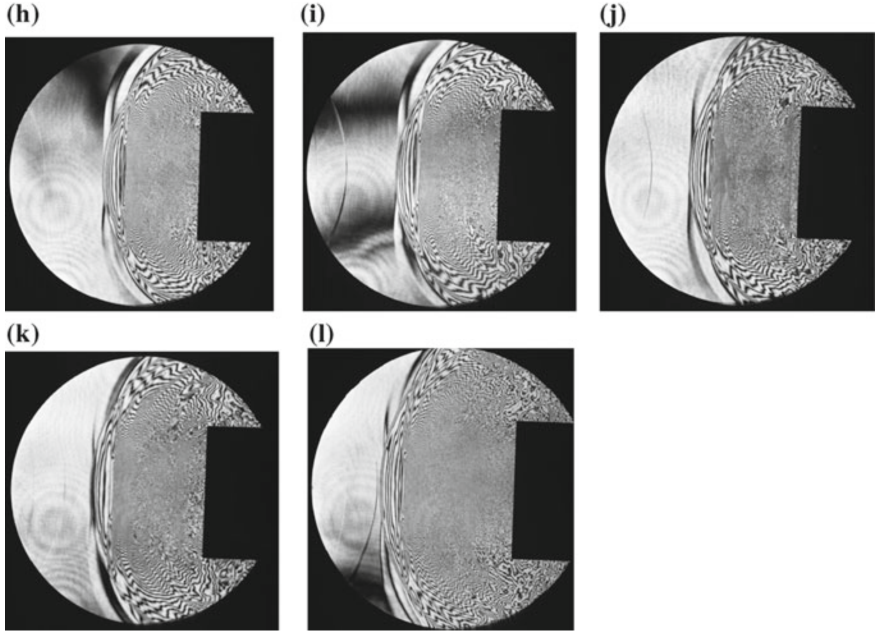

Fig. 9.26 (continued)

Three PETN pellets were tested. Figure 9.28a shows the peak pressure distribution in the neighborhood of the second focal point. The ordinate denotes the peak pressure in MPa and the abscissa denotes the distance from the second focal point in mm. A solid line denotes the result of the TVD numerical simulation (Shitamori 1990). Peak pressures at the second focal point and the measured pressure distributions agree well between the numerical simulation and the experiments. Figure 9.28b summarized the results. The ordinate denotes the peak pressures at the second focal points in MPa and the abscissa denotes weight of PETN and 10 mg AgN_3 in mg. So far tested the peak pressure of about 800 MPa.

9.4.6 Focusing of Underwater Shock Wave Generated by a Pulse Laser Beam

Figure 9.29a shows a schematic diagram of irradiation of a diverging Q-switched laser beam of 1 J intensity of 25 ns pulse width on a 60 mm diameter truncated 90 mm × 128 mm ellipsoidal dish shaped reflector. When the diverging laser beam irradiated the surface of the reflector, a hemi-spherical weak shock wave was created from the concave reflector surface. The shock wave created from the curved surface and propagated toward the focal point as shown in Fig. 9.28b. With

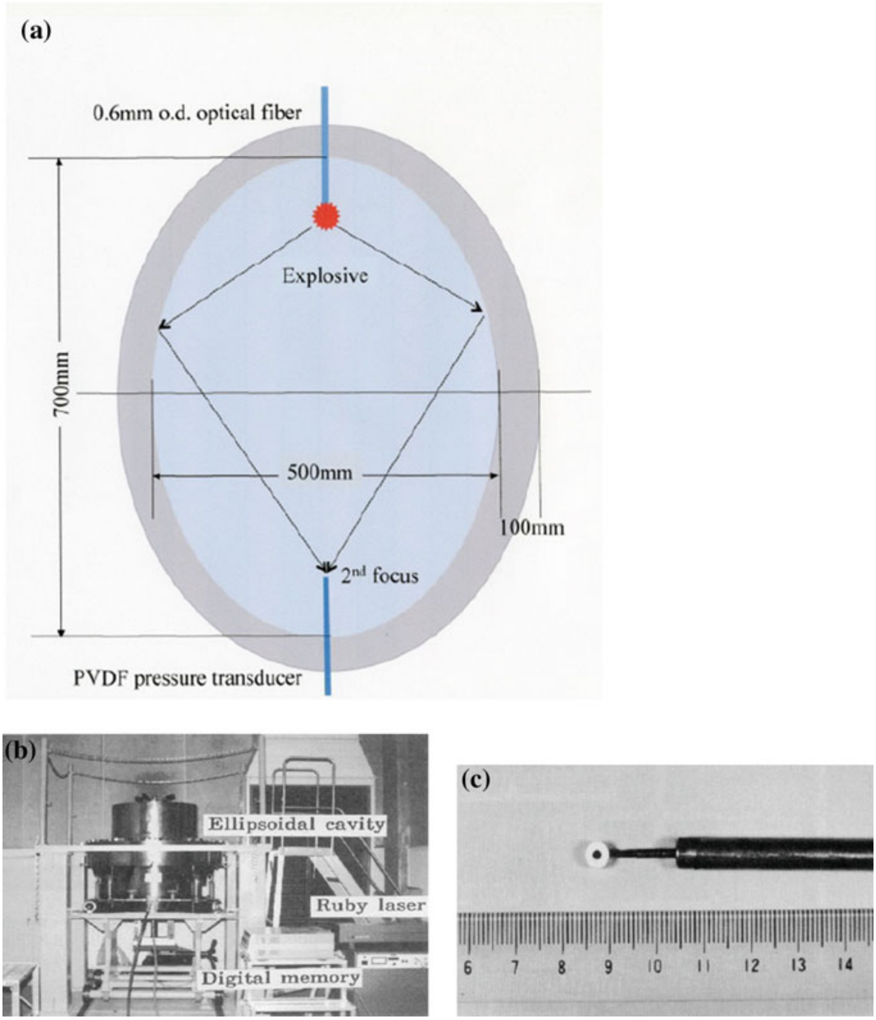

Fig. 9.27 Underwater shock wave focusing from a complete ellipsoidal reflector: **a** principle of underwater shock wave focusing; **b** facility; **c** explosive, PETN triggered by 10 mg AgN_3 igniter

elapsing time, the shock wave created from the curved wall followed the hemi-spherical shock wave and diffracted at the edge of truncated reflector. Figure 9.29b–k shows the evolution of the spherical shock wave propagation and focusing toward the focal point of the reflector. The laser induced shock wave was so weak that the cavitation bubbles were not created during the focusing.

Fig. 9.28 Shock wave focusing in ellipsoidal cavity: **a** peak overpressure along the axis; **b** peak overpressure against mass of PETN pellet and 10 mg AgN_3

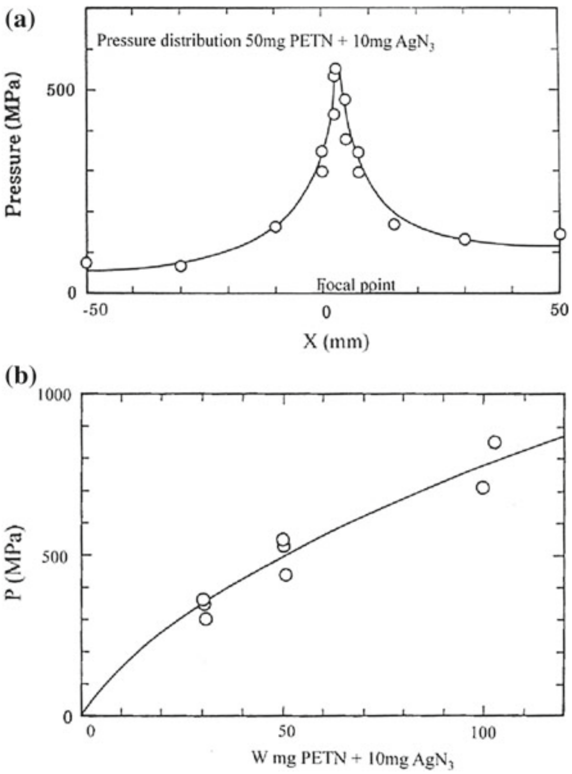

9.4.7 Focusing of a Single Pulse Strong Sound Wave Generated by Oscillation of a Piezo-ceramics

Figure 9.30a shows a 300 mm diameter barium titanium dish. The dish was a part of a 600 mm diameter sphere and composed of 24 segments, each of which was driven at maximum amplitude of 30 μm operated in precisely synchronized fashion in water. With properly tuning the electric impedance of the power supply circuit, the dish was oscillated only once and the second and third oscillations were damped very quickly. Hence, the electric energy was converted to drive the dish segments with higher efficiency (Okazaki 1989).

The impulsive motion of 24 segments of the ceramic dishes generated concavely shaped intense sound waves converging toward the center of the spherical dish as illustrated in Fig. 9.30a. The magnitude of acceleration was in the order of magnitude of $10^3 g$ so that a train of compression waves was generated. Figure 9.30b shows the train of compression waves converting to a shock wave in approaching close to the center. Then, the compression wave eventually turned into a shock wave that is intense enough to disintegrate kidney stones as observed in Fig. 9.30e. At the same time expansion waves generated from the edge of the ring shaped dish

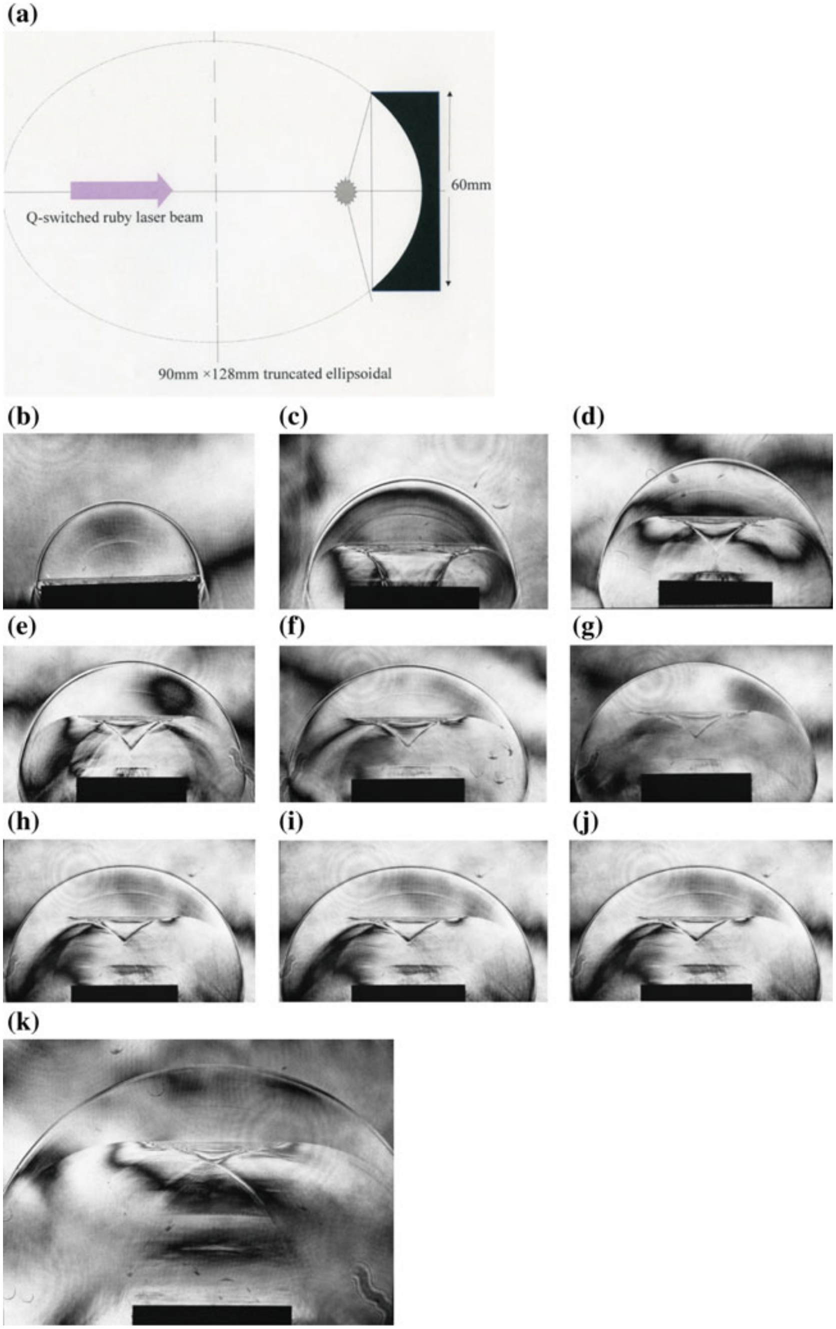

Fig. 9.29 Focusing of shock wave created by irradiation of a Q-switched laser beam of 1 J onto a truncated ellipsoidal reflector: **a** experimental arrangement: **b** #84030712, 15 μs elapsed time from trigger point; **c** #84030711, 25 μs; **d** #84030710, 35 μs; **e** #84030719, 36 μs; **f** #84030716, 37 μs; **g** #84030715, 37 μs; **h** #84030717, 40 μs; **i** #84030714, 41 μs; **j** #84030713, 43 μs; **k** #84030708, 55 μs

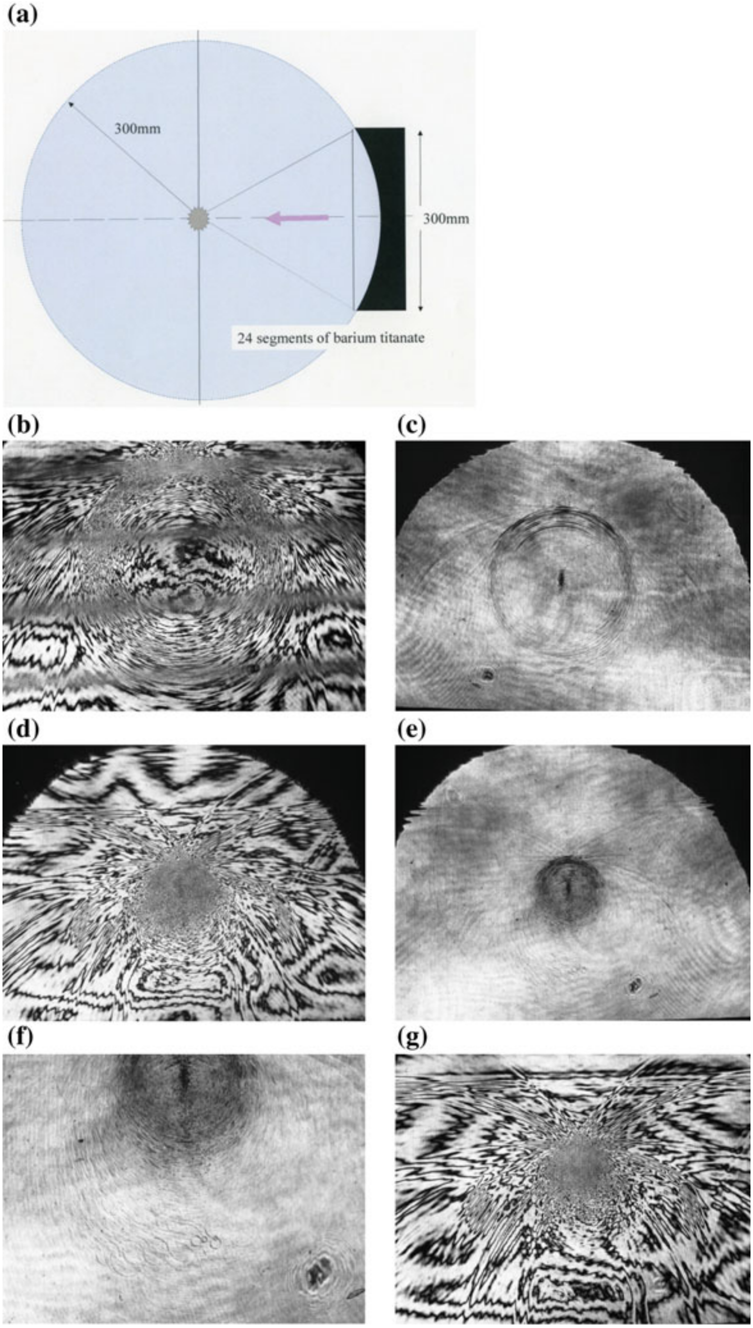

Fig. 9.30 Focusing of ultrasound waves: **a** experimental setup; **b** #88012205, 331 μs from trigger point; **c** #88012211, 331 μs; **d** #88012204, 351 μs; **e** #88012210, 351 μs; **f** enlargement of (**g**); #88012201, 358 μs; **h** enlargement; **i** #88012216, 358 μs; **j** #88012215, 358 μs; **k** #88012214, 358 μs; **l** enlargement of (**k**); **m** #88012206, 358 μs; **n** #88012202, 365 μs; **o** #88012203, 385 μs; **p** enlargement of (**m**); **q** enlargement of (**o**)

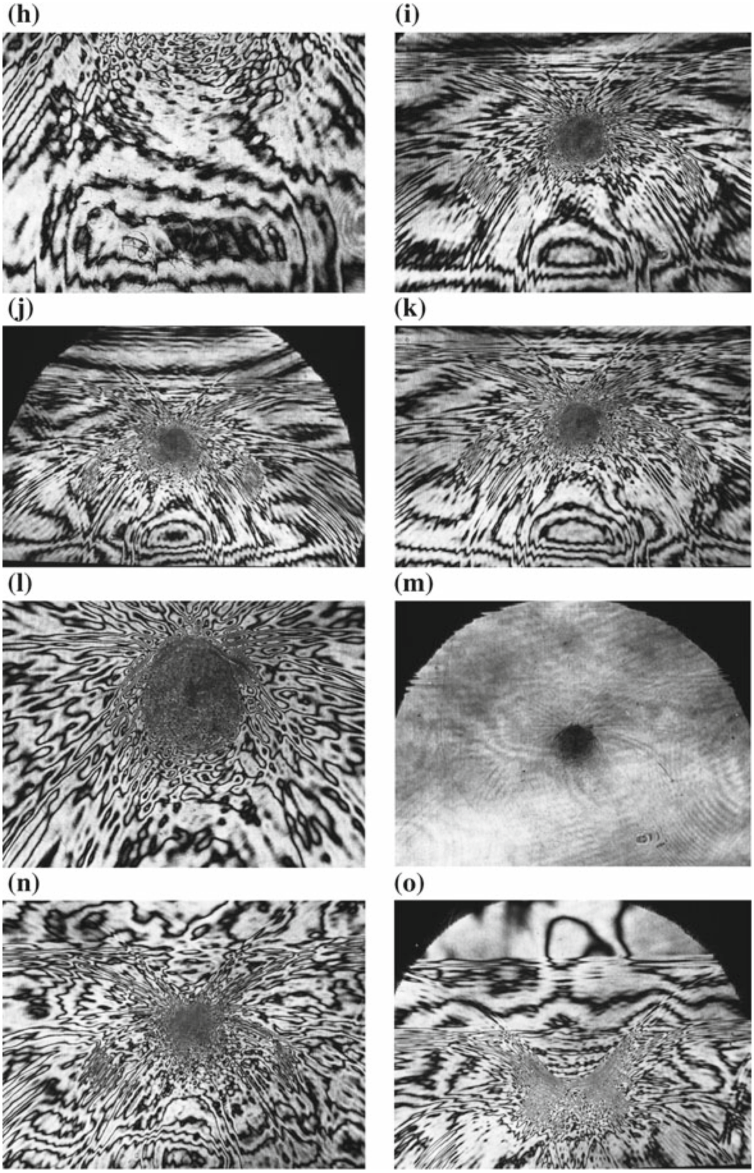

Fig. 9.30 (continued)

decreased the high pressures. The interferometric image clearly visualizes a high pressure spike appearing at the focal point, which would effectively crack kidney stone.

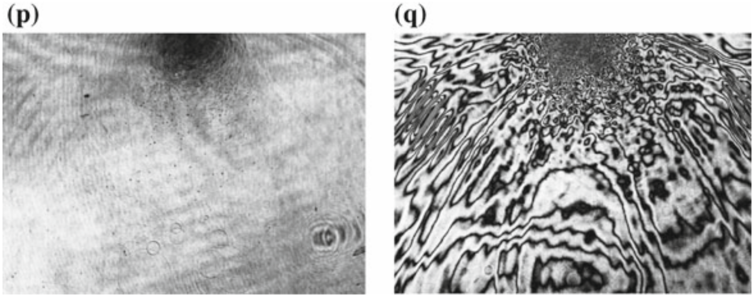

Fig. 9.30 (continued)

A train of compression waves driven by 24 segments eventually formed dense fringe accumulation at the center of the dish. Figure 9.30 shows sequential observations of a single oscillation of 2.7 kV input energy at the trigger time from about 330 to 385 μs. Figure 9.30c, e shows single exposure interfrograms. Fringe concentrations show localized pressure enhancements at focal area. The peak pressure so far measured were well over 100 MPa. When the expansion waves caught up the high pressures, a very sudden disappearance of high pressures induced a high tensile force, which spontaneously exceeded well over the so-called spalling pressure in water. Then, cavitation bubbles were generated and the bubbles immediately collapse generating secondary bubbles as seen in Fig. 9.30e, g. Figure 9.30f, h shows their enlargement. Figure 9.30p, q are enlargements of Fig. 9.30m, o, respectively. Figure 9.30b, c are double exposure interferograms and single exposure interferograms taken at the same delay time of 331 μs. Figure 9.30d, e are pairs taken at 351 μs. Figure 9.30k, l are pairs taken at 358 μs. In single exposure interferograms, the cavitation bubbles and secondary shock waves were observed, whereas in double exposure interferograms the density variations were readily estimated.

9.5 Underwater Shock Wave/Bubble Interaction

The interaction of underwater shock waves with bubbles is a fundamental research topic not only in the shock wave dynamics but also in the bubble dynamics (Shima 1997). The shock wave/bubble interaction is one of the mechanisms closely related to tissue damages occurring during the extracorporeal shock wave lithotripsy, ESWL.

9.5.1 A Single Spherical Air Bubble

In the hydrodynamic research, ot is known that cavitation phenomena occur not only in high-speed water flows but also are initiated by a sudden pressure decrease.

The so-called cavitation erosion was one of the important topics in the research of hydraulic machineries (Shima 1997). Tissue damages occurring during the ESWL treatments are generated by shock wave/bubble interactions (Chaussey et al. 1982; Kuwahara et al. 1986). Then an investigation of observing the shock wave interaction with a single bubble became a basic research topic.

A bubble placed in a quiescent water starts to oscillate exposed to a pressure fluctuation. Then such a symmetric bubble motion was summarized by Shima (1997). However, a bubble impinged by an underwater shock wave, unlike a symmetric bubble motion. Induced its complex deformation and eventually a micro-jet is generated.

If defining u the speed of the micro jet, a the sound speed in water, and ρ the water density, the resulting stagnation pressure p_{st} can be written as $p_{st} = a\rho u$. In particular, the diameter of the bubbles produced during the ESWL treatments is sub-millimeter diameter. If the jet speed is assumed to be 100 m/s, then this jet would create a stagnation pressure over 150 MPa, which would readily penetrate any tissues.

A slurry explosive comprises of thin shell glass balloons containing air mixed evenly in dissolved ammonium nitrate grains in kerosene. The glass balloons had diameters ranging a few 100 μm diameter containing air. When a detonation wave propagated in the slurry explosive and collapsed the thin shell glass balloons just like what observed during shock wave/air bubble interaction, the air in glass balloons had minimal volume, then the gas temperature enhanced high at a singular spot inside the bubble. The successively created high temperature maintained the detonation. The hot spots are not necessarily produced due to adiabatic compressions of contracting air bubble but created by the shock wave focusing from a concavely shaped air/liquid boundary. The shock wave/bubble interaction sustained the propagation of the detonation in slurry explosives. Shima (1997) assumed hot spot generations during due to adiabatic compression. However, it is the shock compression that enhanced the temperature much more efficiently than the adiabatic compression.

In order to sequentially observe a shock wave/bubble interaction, an analogue experiment was conducted. A 1.7 mm diameter air bubble interacted with a shock wave generated at 20 mm stand-off distance by exploding a 4 mg PbN_6 pellet attached on the edge of a 0.6 mm diameter optical fiber. The transmitted a Q-switched Nd:YAG laser beam thorough the optical fiber exploded the pellet. The experiment was conducted in a 500 mm × 500 mm × 500 mm stainless steel chamber. The air bubble was released from its bottom. The volume of the air bubble was determined by measuring from the length of air filled in a 0.3 mm diameter capillary tube prior to releasing it in the test chamber. A When the air bubble arrived at the 20 mm stand-off distance from the position of the explosive. The overpressure of the shock wave generated at the 20 mm stand-off distance was approximately 25 MPa.

The mechanism of the jet formation inside a contracting bubble is related to the generation of the so-called Neumann jet. When a cylindrical explosive was ignited from its flat surface, a plane transmitted detonation wave propagated through the explosive, for example, as seen in Fig. 8.2. If another surface had a reversely conical cavity, the transmitted detonation wave was diffracted from the concave

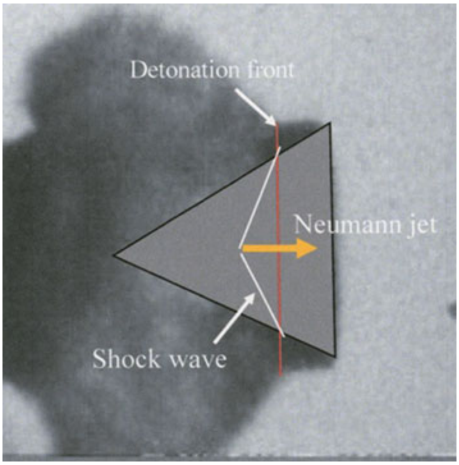

Fig. 9.31 The explanation of the Neumann effect

cavity wall and focused at the center axis creating a jet moving to the direction of the detonation wave propagation. At the same time, the detonation product gas at the top of the conical cavity was ejected to the same direction. Figure 9.31 shows the enlargement of exploding a 10 mg AgN_3 pellet shown in Fig. 8.2. A detonation wave propagated inside a cylindrical explosive shown in a red line and was diffracted at the concave wall. It focused at the center axis and the jet so far combined there was shown in a thick yellow arrow. The jet formation is called the Neumann effect which has an identical physical background as micro-jet formation inside the contracting air bubble. The Neumann effect is one of the representations of shock wave interactions at a fast/slow interface and its physical background is analogous to the jet formation occurring at the bubble collapse.

In Fig. 9.32, the evolution of shock wave interaction with a single bubble are shown. Visualizations were conducted by double exposure and single exposure holographic interferograms. In the double exposure interferograms, the first exposure recorded undisturbed bubble, the second exposure recorded the bubble deformed by the shock wave loading, and these two images were superimposed on one film. The double exposures were conducted at about 1 ms interval hence the bubble looked slightly blurred, whereas in a single exposure interferogram, the bubble shape was clearly observed.

When a shock wave hit a bubble, it started to contract and simultaneously the expansion wave was reflected from its surface as seen in Fig. 9.32b. The time allocated to individual double exposure interferograms indicates elapsed time from the explosion. The bubble continued to contract. When it reached a minimal volume, the pressure at its frontal stagnation point became maximal. The densely concentrated fringes at the frontal stagnation point show the pressure enhancement. At the next moment, when the high pressures were released into water, trains of compression waves propagated and coalesced into a secondary shock wave as shown in Fig. 9.32c–g.

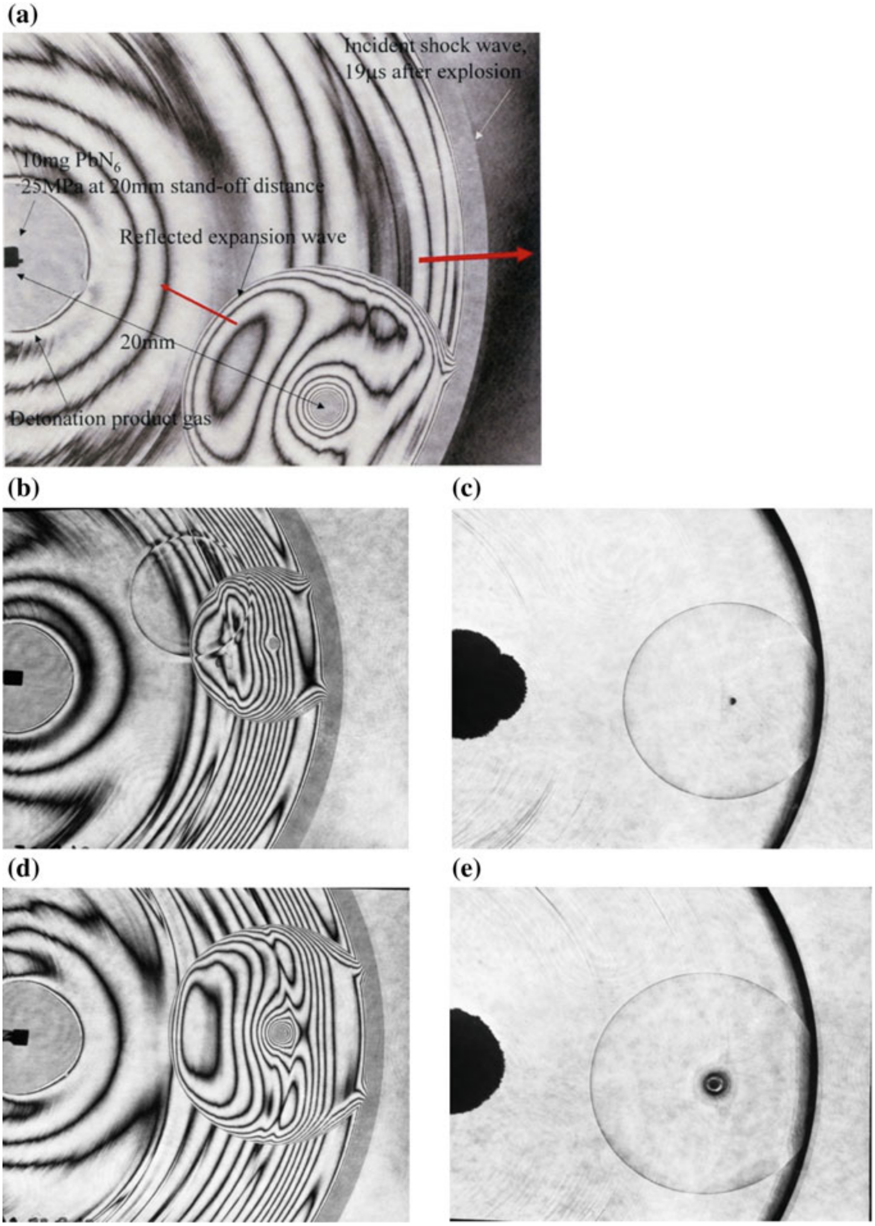

Fig. 9.32 Interaction of a shock wave with a single bubble of 1.7 mm diameter positioned at the 20 mm stand-off distance from the position of a 10 mg PbN_6 pellet at 296 K: **a** #86082608, 19.0 μs after shock wave impingement. The bubble rising speed was v = 0.187 m/s; **b** #86082507, 18.4 μs, v = 0.165 m/s; **c** #86082610, 23 μs, single exposure; **d** #86082506, 20.1 μs, v = 0.184 m/s; **e** #86082609, 25 μs, single exposure; **f** #86082505, 22.1 μs, v = 0.164 m/s; **g** #86082615, 25 μs, single exposure; **h** #86082504, 23.2 μs, v = 0.224 m/s; **i** #86082613, 26 μs, single exposure; **j** #86082606, 23.5 μs, v = 0.187 m/s (Ikeda et al. 1999)

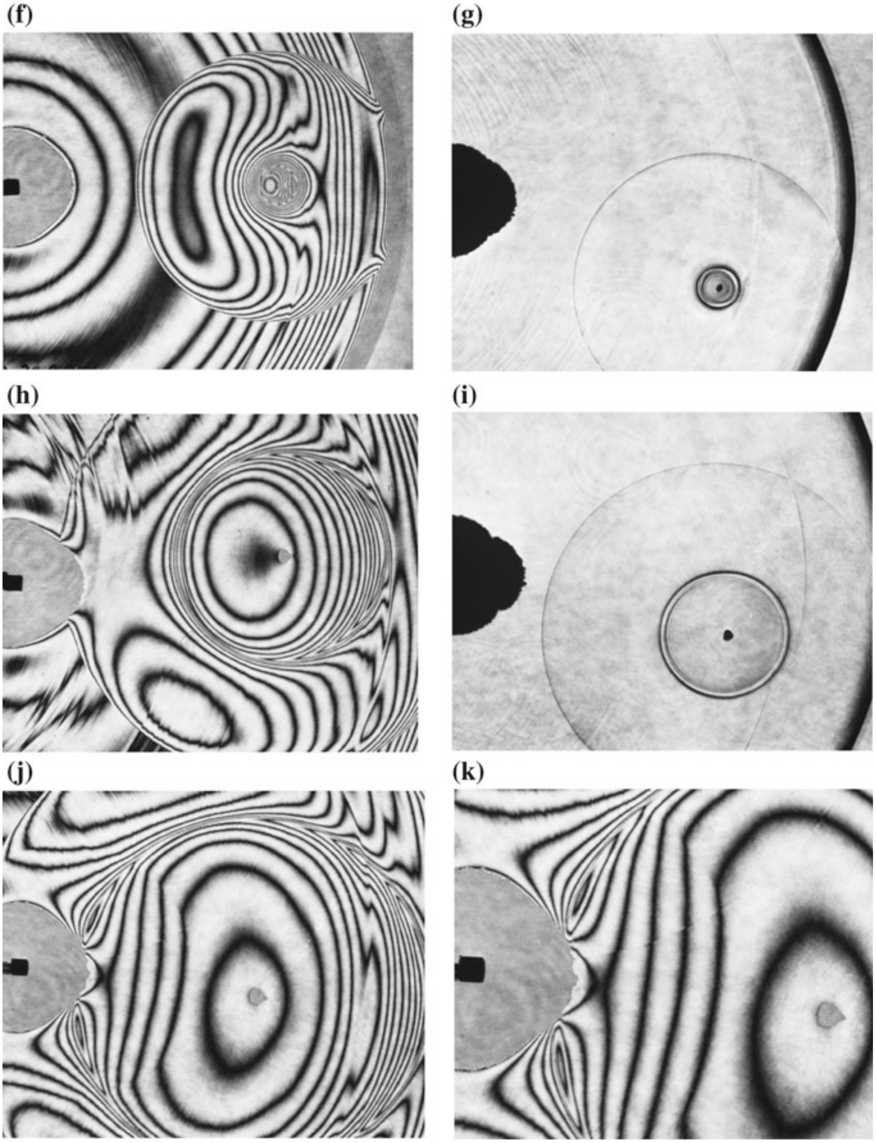

Fig. 9.32 (continued)

Following to the analogous mechanism to the Neumann effect as already explained in Fig. 9.31, a jet was formed inside the contracting bubble. Its formation depends on parameters such as the bubble size which is expressed in terms of the ratio of the deviated bubble radius to the perfectly spherical one and the ratio of sound speeds in the gas bubble to the liquid. Figure 9.32j, k show a later stage of the secondary shock wave impingement on the detonation product gas bubble.

The bubble surface showed an irregular shape because the interfacial instability occurred on the shock impinged bubble surface.

As the density gradient across the expansion wave is opposite to that across the shock wave in the double exposure interferograms, the direction of fringe shift across the expansion wave is different from that across the shock wave. Assuming that the fringe distributions in Fig. 9.32 are axial symmetry, the density distribution behind shock waves and expansion waves are readily determined by evaluating fringe distributions. Assuming isentropic flows, the pressure distribution is readily obtained from the density distribution (Abe 1989). Figure 9.33a–d are the pressure profiles along the distance from the center of explosion evaluated from the images presented in Fig. 9.32b, d, f, h, each of which was taken at 18.4, 20.1, 22.1, and 23.2 μs from the ignition, respectively. The ordinate denotes the pressure in bar and the abscissa denotes the distance normalized by the stand-off distance of 20 mm. Figure 9.33a shows the presence of a reflected expansion wave. Open circles denote experimental results estimated from fringe distributions. Figure 9.33b shows the generation of the peak pressure analogous to the pressure profile occurring at a point explosion. In Fig. 9.33c, d, a train of compression waves coalesced forming a secondary shock wave. The propagation of and the attenuation of the secondary shock wave are clearly observed in Fig. 9.33b–d.

When a bubble placed in a quiescent liquid responds to a pressure fluctuation caused by wavelets passing over the liquid surface and starts to symmetrically oscillate. Eventually, when it reached to a minimal volume, due to an adiabatic compression, the temperature inside the bubble reached maximal. Then the bubble emitted luminescence. This is the so-called sono-luminescence.

Another extreme case is that when a shock wave hit the bubble, the bubble responded sharply to the shock wave and started deforming asymmetrically. The degree of its deformation and the direction of the motion were governed by the shock wave strength. Regarding the wave motion inside the deforming bubble, a little is known. A numerical simulation would be possible approach to resolve asymmetrical wave motion inside contracting bubbles.

In the adiabatic compression, the dimension-less temperature T/T_0 normalized by the ambient temperature T_0 and dimension-less pressure p/p_0 normalized by the ambient pressure p_0 are related to,

$$T/T_0 = (p/p_0)^{2/7} \quad \text{for}\, \gamma = 1.4, \tag{9.10}$$

whereas in the shock compression, the temperature increases proportional to the pressure ratio as following,

$$T/T_0 \propto p/6p_0 \quad \text{for}\, p/p_0 \gg 1. \tag{9.11}$$

For example, in order to achieve $T/T_0 = 17$ by the adiabatic compression, p/p_0 can be 19,000, whereas in the shock compression, p/p_0 is only about 100, which can be obtained behind a shock wave of Ms = 8.3 in ideal diatomic gases.

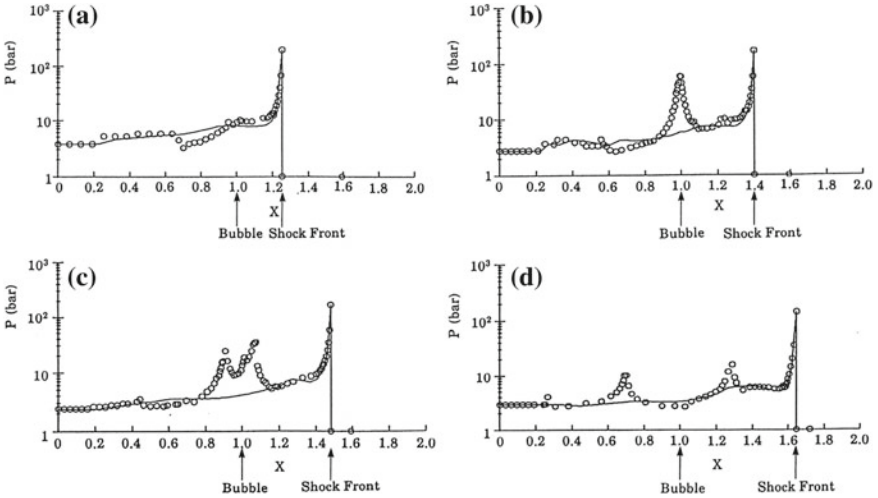

Fig. 9.33 Pressure distributions estimated from Fig. 9.32b, d, f, h: **a** 18.4 μs from the ignition; **b** 20.1 μs; **c** 22.1 μs; **d** 23.2 μs (Abe 1989)

In Fig. 9.32, the optical arrangement is based on, in principle, a direct shadowgraph. Hence holographic films are facing to the test section. Then although the luminous emission from the hot spot could be readily recorded, it was not recorded at all because the present holo-films were insensitive to the wavelength of the luminosity emission.

9.5.2 A Single Non-spherical Air Bubble in Water

Figure 9.34 shows sequential shadowgraphs of the shock wave interacting with a disk shaped air bubble having its aspect ratio of 1.5 mm × 2.5 mm. The images are recorded by ImaCon D-200. 14 images are recording for time interval ranging from 9.9 to 22.9 μs at 1 μs interval and the exposure time of 10 ns. The pressure is measured on the end wall by an optical fiber pressure transducer at the stand-off distance of 2 mm from the center of the air bubble. The shock wave is generated by exploding a 10 mg AgN_3 pellet at the 20 mm stand-off distance from the center of the bubble. The overpressure measured at 20 mm stand-off distance is about 25 MPa. The bubble starts to contract upon the shock wave loading. Although the reflected expansion wave is not distinctly visible but the secondary shock wave is observed from the moment when the bubble reached a minimal volume as seen in Fig. 9.34j, k. A sign of luminous emission was observed in Fig. 9.34i. The emission became brighter in Fig. 9.34j and maintained for about 1 μs. Figure 9.34j shows that the brightest point is slightly shifted toward the upstream, which implies that the luminous emission is caused due to wave motion occurring inside the

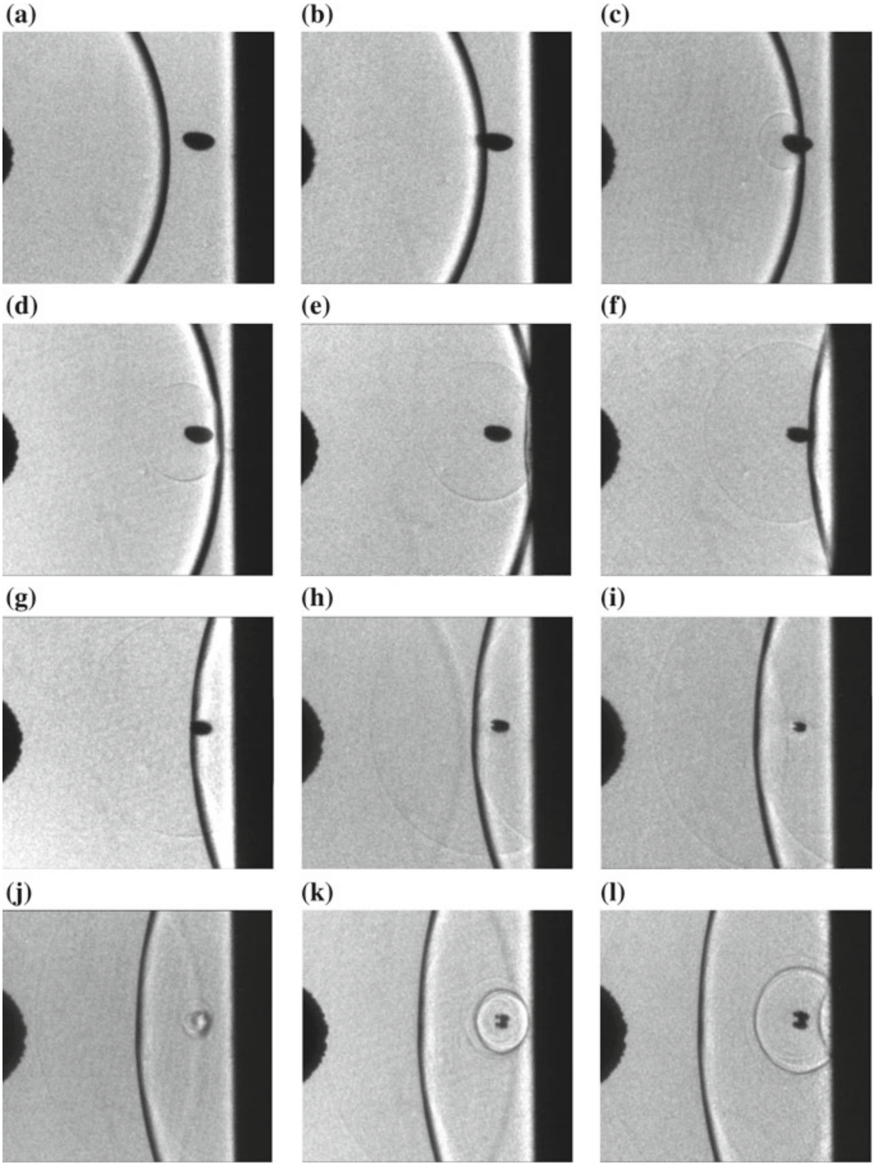

Fig. 9.34 Sequential observation of interaction of a non-spherical air bubble with an underwater shock wave generated by exploding a 10 mg AgN_3 pellet at stand-off distance of 20 mm: **a** 9.9 µs; **b** 10.9 µs; **c** 11.9 µs; **d** 12.9 µs; **e** 13.9 µs; **f** 14.9 µs; **g** 15.9 µs; **h** 16.9 µs; **i** 17.9 µs; **j** 18.9 µs; **k** 19.9 µs; **l** 20.9 µs; **m** 21.9 µs; **n** 22.9 µs; **o** time variation of pressure measured on the end wall (Courtesy of Dr. Ohtani)

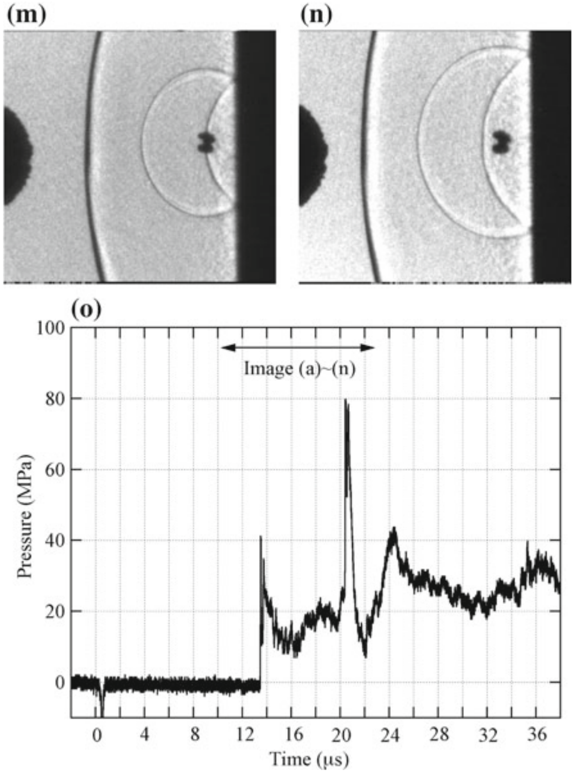

Fig. 9.34 (continued)

bubble. Figure 9.34o shows the pressure variation as a summary of the sequential visualization. The ordinate denotes pressure in MPa and the abscissa denotes elapsed time of shadow pictures in μs. At 13.5 μs shown in Fig. 9.34e, the incident shock wave arrived at the wall. At about 20.5 μs, the secondary shock wave arrived at the wall and its peak pressure reached about 80 MPa.

9.5.3 Luminous Emission

Figure 9.35 shows sequential observations of shock wave/bubble interaction recorded by a high speed video camera Shimadzu SH100 at the frame rate of 10^6 frame/s and exposure time of 125 ns. A 2.0 mm diameter spherical air bubble is impinged by a shock wave generated by exploding a 10 mg AgN_3 pellet at the stand-off distance of 20 mm. The black shadow on the right is an explosion product gas bubble, the so-called fire ball in the case of explosions in air. In Fig. 9.35b, a reflected expansion wave is shown as a faint grey circle. In Fig. 9.35d, faintly

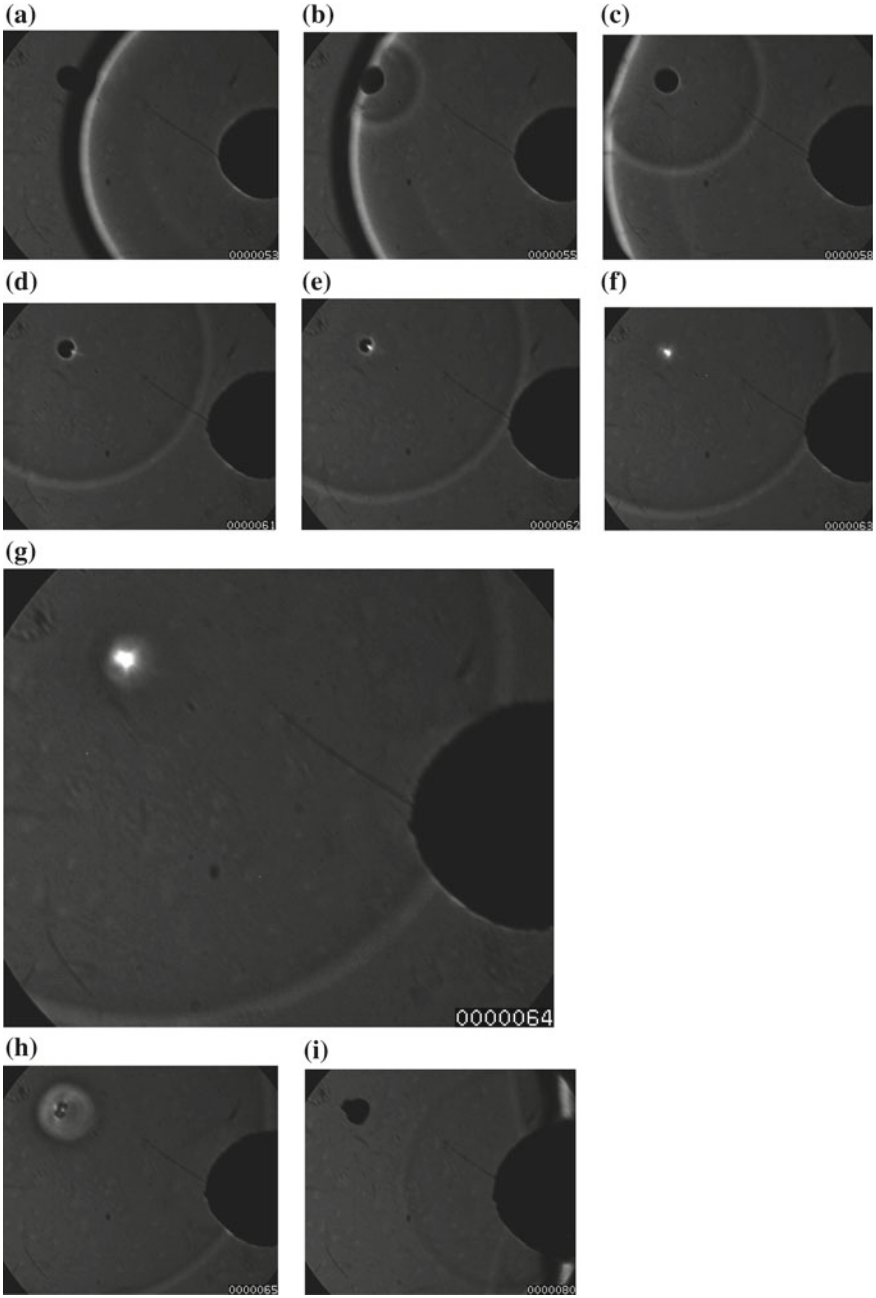

Fig. 9.35 Interaction of a 2.0 mm dia. Air bubble with a shock wave generated by exploding a 10 mg pellet at the stand-off distance 20 mm: **a** frame #53; **b** frame #55; **c** frame #58; **d** frame #61; **e** frame #62; **f** frame #63; **g** the brightest emission, frame #64; **h** frame #65; **i** frame #80 (Takayama et al. 2015)

shining point is observed at a frontal stagnation point. With elapsing time, the bubble contracts and its volume becomes minimal as seen in Fig. 9.35f. Then, the bubble started expanding and a secondary shock wave appeared in Fig. 9.35g, h. In Fig. 9.35g the luminosity is the brightest and the initiation of the secondary shock wave is faintly observed. The hot spot is located at the frontal side of the expanding bubble, which indicates that the hot spot is created by the wave interaction inside the bubble. An appropriate numerical simulation will reveal that the wave interaction decisively contributes to the hot spot formation.

Figure 9.36 summarizes the temporal variation of the brightness intensity of luminosity along the center axis. The ordinate denotes the brightness intensity of luminosity in arbitrary unit from the frame #60 to #67 for elapsed time from 60 to 67 μs. The abscissa denotes the distance between the center of the bubble and the center of the explosive in mm. The brightness of luminosity was maximal at the moment when the bubble volume was minimal at 65 μs and the secondary shock

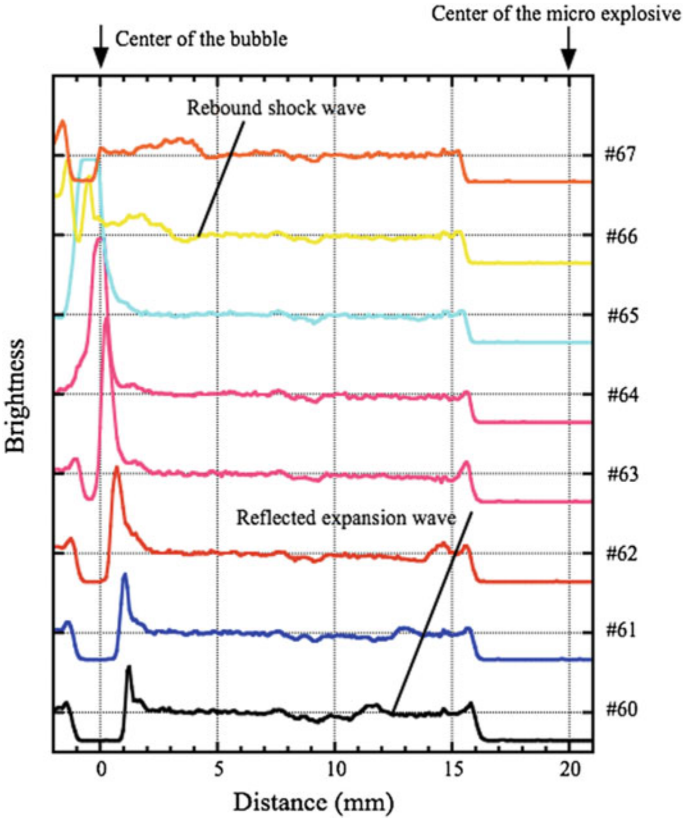

Fig. 9.36 Time variation of brightness of a luminous point in shock/bubble interaction. Shock wave was generated by exploding a 10 mg AgN_3 pellet at stand-off distance 20 mm (Takayama et al. 2015)

wave is initiated. At elapsed time of 67 μs, the luminous point moved toward the rear part of the bubble.

9.5.4 Shock Wave/Air Bubble Interaction in Silicone Oil

Figure 9.37 shows sequential observation of shock wave/bubble interaction in 1cSt, 10cSt, 100cSt and 1000cSt PDMS. The experiments were conducted in a 300 mm diameter and 300 mm wide test chamber by filling silicone oil of 1cSt, 10cSt, 100cSt and 1000cSt at 290 K in it.

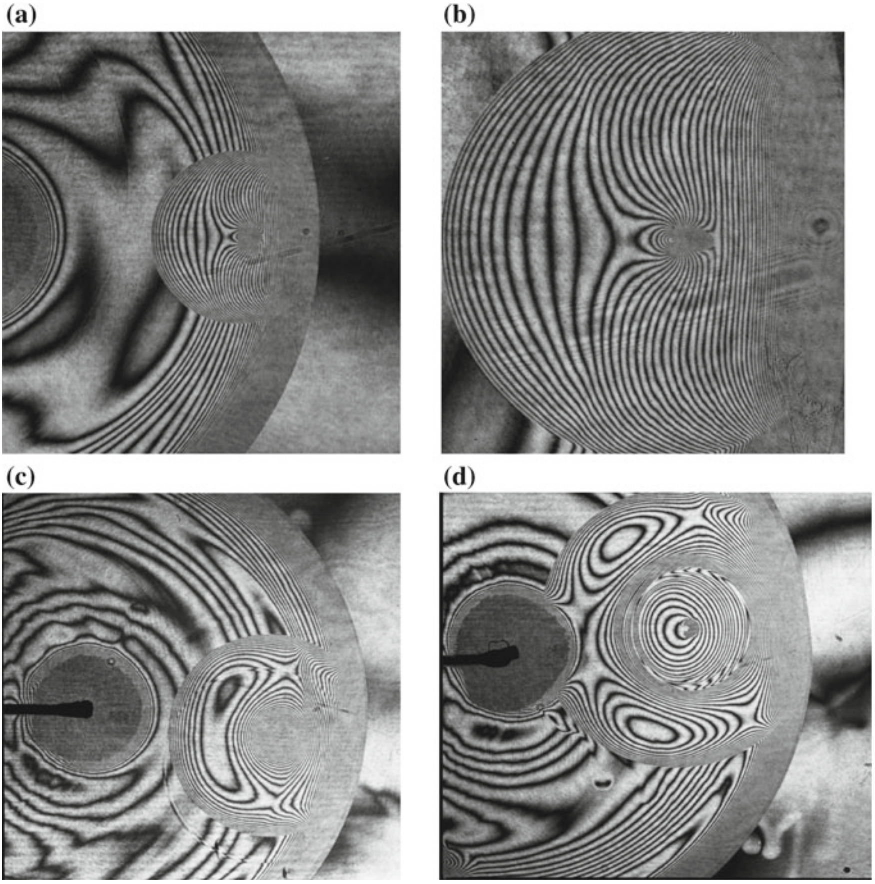

Fig. 9.37 Shock wave/air bubble interaction in 1cSt PDMS. Bubble diameter is 2.04 mm, at 297.9 K. A shock wave is generated by exploding a 10 mg AgN_3 pellet at stand-off distance 20 mm: **a** #91031103; **b** enlargement of (**a**); **c** #91031115; **d** #91031109

9.5.4.1 1cSt PDMS

Figure 9.37 shows sequential observations of a 2.04 mm air bubble in 1cSt PDMS interacting with shock waves generated by exploding a 10 mg AgN_3 pellet at the stand-off distance of 20 mm. The evolution of bubble motion is similar to the case of a 1.7 mm air bubble interacting with an underwater shock wave as seen in Fig. 9.32. Figure 9.37b is an enlargement of Fig. 9.37a, in which the bubble has a slightly ellipsoidal shape, whereas in Fig. 9.32, the bubbles were truly spherical. The slightly ellipsoidal bubble motion slightly differs from that of truly spherical one. In Fig. 9.37d, the final shape of the collapsing bubble had a convex shape (Hayakawa 1987).

9.5.4.2 10cSt PDMS

Figure 9.38 shows a sequential observation of shock wave/air bubble interaction of a 1.5 mm diameter air bubble in 10cSt PDMS. Shock waves were generated by exploding a 10 mg AgN_3 pellet at the stand-off distance of 20 mm (Hayakawa 1987). In Fig. 9.30f, at long time later the bubble reached almost a minimal volume again. The secondary shock wave interacted with the detonation product gas bubble. The expansion wave was reflected and the jaggedly shaped bubble surface were observed due to interfacial instability.

9.5.4.3 100cSt PDMS

Figure 9.39 shows the evolution of shock wave interaction with a 1.5 mm diameter spherical air bubble in 100cSt PDMS. The shock wave is generated by the explosion of a 10 mg AgN_3 pellet at stand-off distance 20 mm. The interaction of the bubble with the shock wave is very similar to that in 10cSt PDMS as seen in Fig. 9.38 (Hayakawa 1987). In Fig. 9.39a, the bubble reached a minimal volume and a very dense fringe accumulation was observed.

9.5.4.4 1000cSt PDMS

Figure 9.40 shows the evolution of shock wave interaction with a 1.5 mm diameter spherical air bubble in a highly viscous 1000cSt PDMS. The shock wave is generated by exploding a 10 mg AgN_3 pellet at stand-off distance of 20 mm. The bubble deformation is slightly retarded than that of less viscous PDMS (Hayakawa 1987).

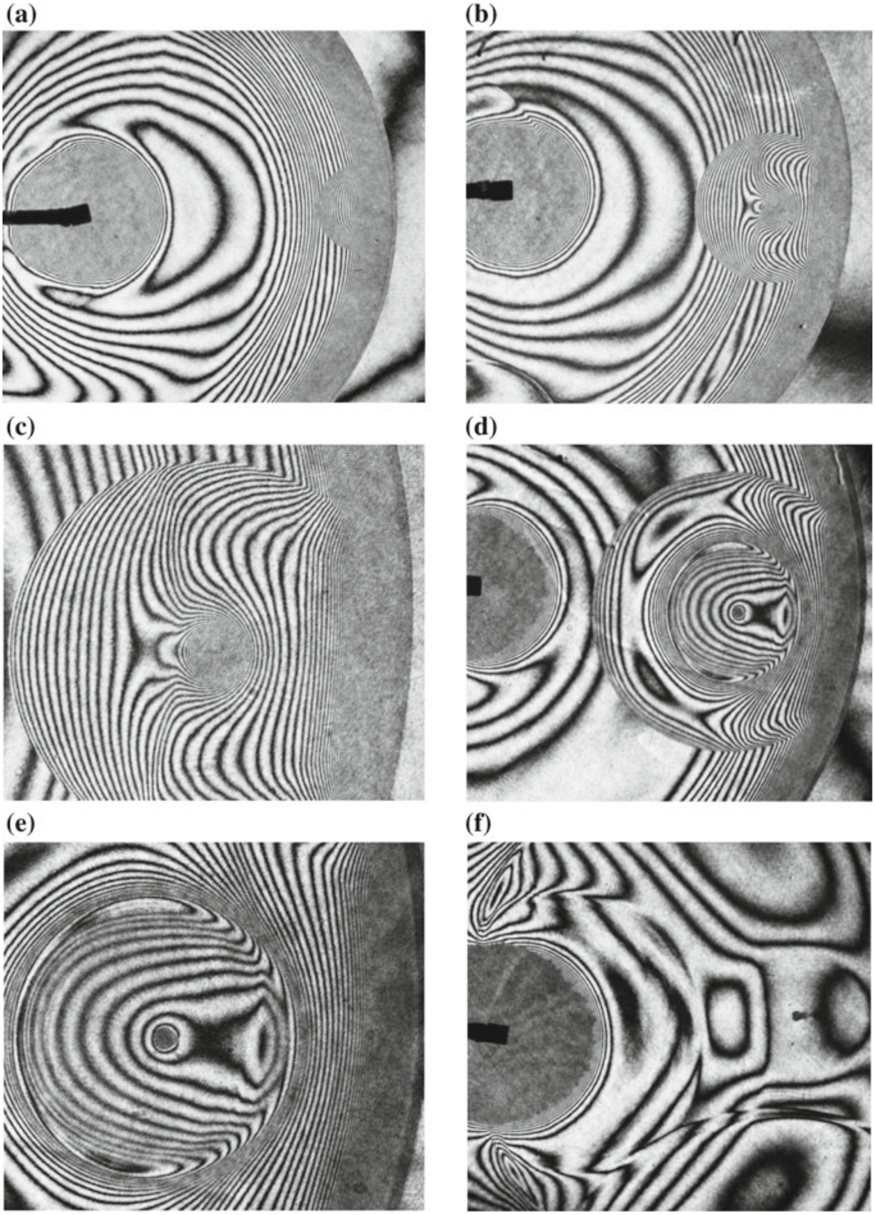

Fig. 9.38 Shock wave/air bubble interaction in 10cSt PDMS. Bubble diameter is 1.5 mm, at 298 K. A shock wave is generated by exploding a 10 mg AgN_3 pellet at stand-off distance 20 mm: **a** #98012102; **b** #98012003; **c** enlargement of (**b**); **d** #98012004; **e** enlargement of (**d**); **f** #98012006

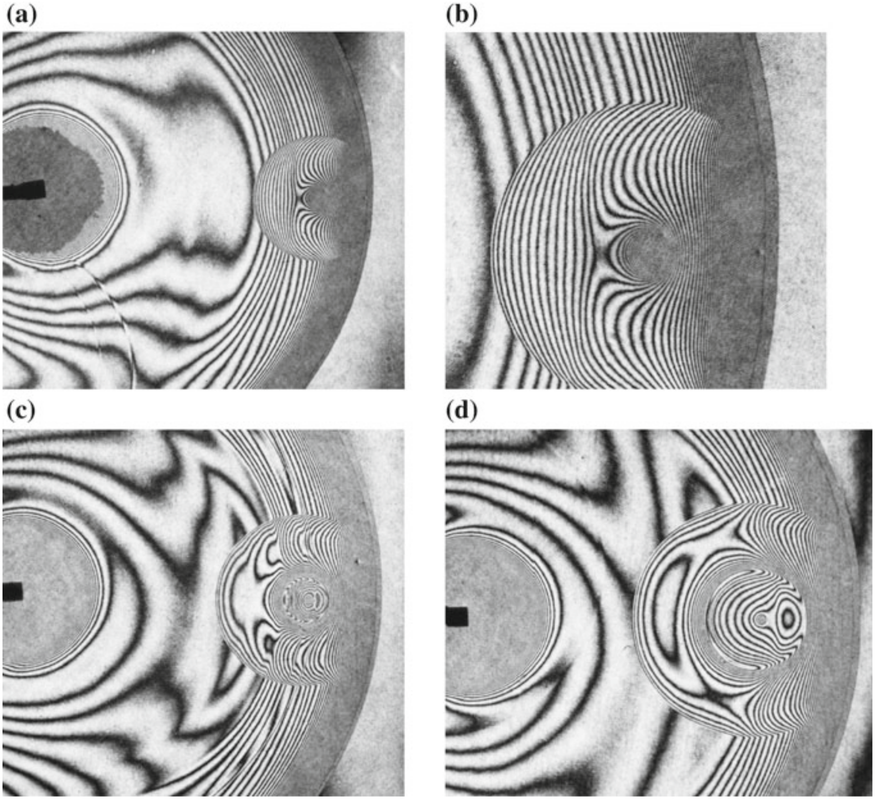

Fig. 9.39 Shock wave/air bubble interaction in 100cSt PDMS. Bubble diameter is 1.5 mm, at 298 K. A shock wave is generated by exploding a 10 mg AgN_3 pellet at stand-off distance 20 mm: **a** #98012104; **b** enlargement of (**a**); **c** #98012105; **d** #98012103 (Takayama et al. 2015)

9.5.5 Golden Syrup

Figure 9.41 shows the evolution of the shock wave interaction with a 2.0 mm diameter air bubble in 70 wt% golden syrup. The golden syrup contains 30% of water in weight and 70% of golden syrup in weight. The viscosity of this 70 wt% golden syrup is close to that of 1000cSt PDMS. The shock wave was generated by exploding a 10 mg AgN_3 pellet at the stand-off distance of 20 mm. The direct shadowgraph images were recorded with a high-speed video camera Shimadzu SH100 at framing rate of 10^6 frame/s and exposure time of 125 ns.

In Fig. 9.41, the shock wave propagates from right to left. A dark circular shadow on the right is the fire ball of a 10 mg AgN_3 pellet. A faintly grey circle surrounding the air bubble is a reflected expansion wave and the detonation product gas bubble is seen on the right hand side. In Fig. 9.41c, the air bubble contracts and the reflected expansion wave develops. In Fig. 9.41d, the air bubble has a minimal volume emitting luminosity. In Fig. 9.41e, the luminosity is emitted at the point

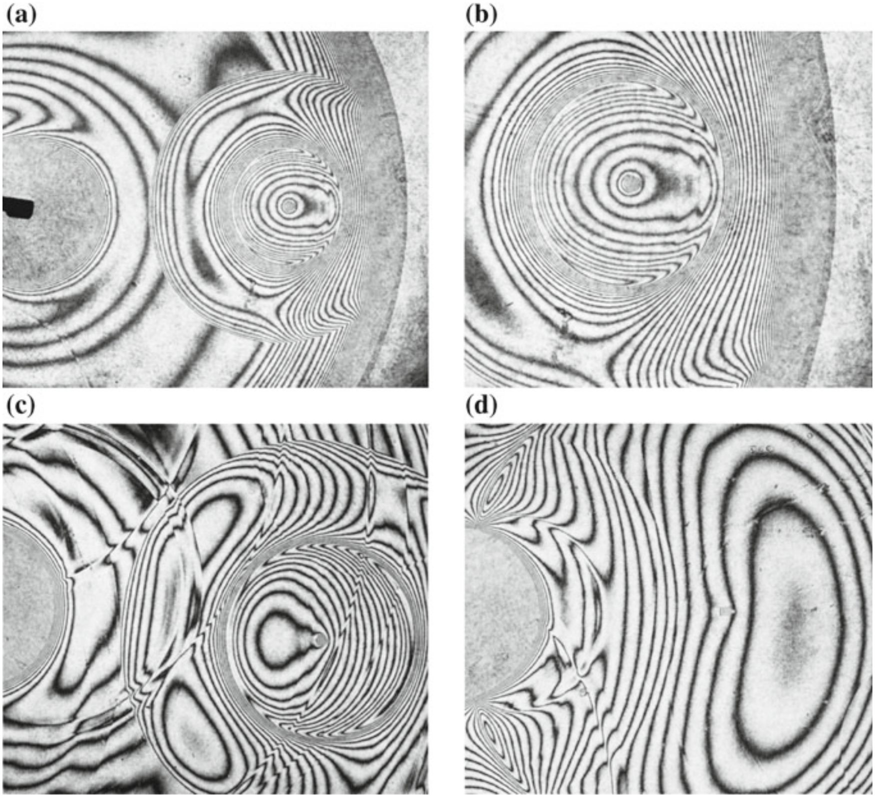

Fig. 9.40 Shock wave/air bubble interaction in 1000cSt PDMS. Bubble diameter is 1.5 mm, at 298 K. A shock wave is generated by exploding a 10 mg AgN_3 pellet at stand-off distance 20 mm: **a** #98032508; **b** enlargement of (**a**); **c** #98032509; **d** #98032510

located bubble's frontal side. This indicates that the hot spot is formed by a wave focusing inside the bubble (Takayama et al. 2015).

Figure 9.42 summarizes the time variation of luminosity along the distance between the bubble and the center of the explosive presented in Fig. 9.41. The ordinate denotes brightness of luminosity in arbitrary unit measured from the frame #52 to #61. The abscissa denotes elapsed time from 52 to 61 µs. At 57 µs corresponding to Fig. 9.41d, the luminosity is the brightest and the secondary shock wave is just generated at this time instant.

9.5.6 Helium Bubble in Silicon Oil

The wave motion inside the bubble impinged by a shock wave is governed by the ratio of the sound speed in a gas bubble to that in a liquid. Hence, the deformation

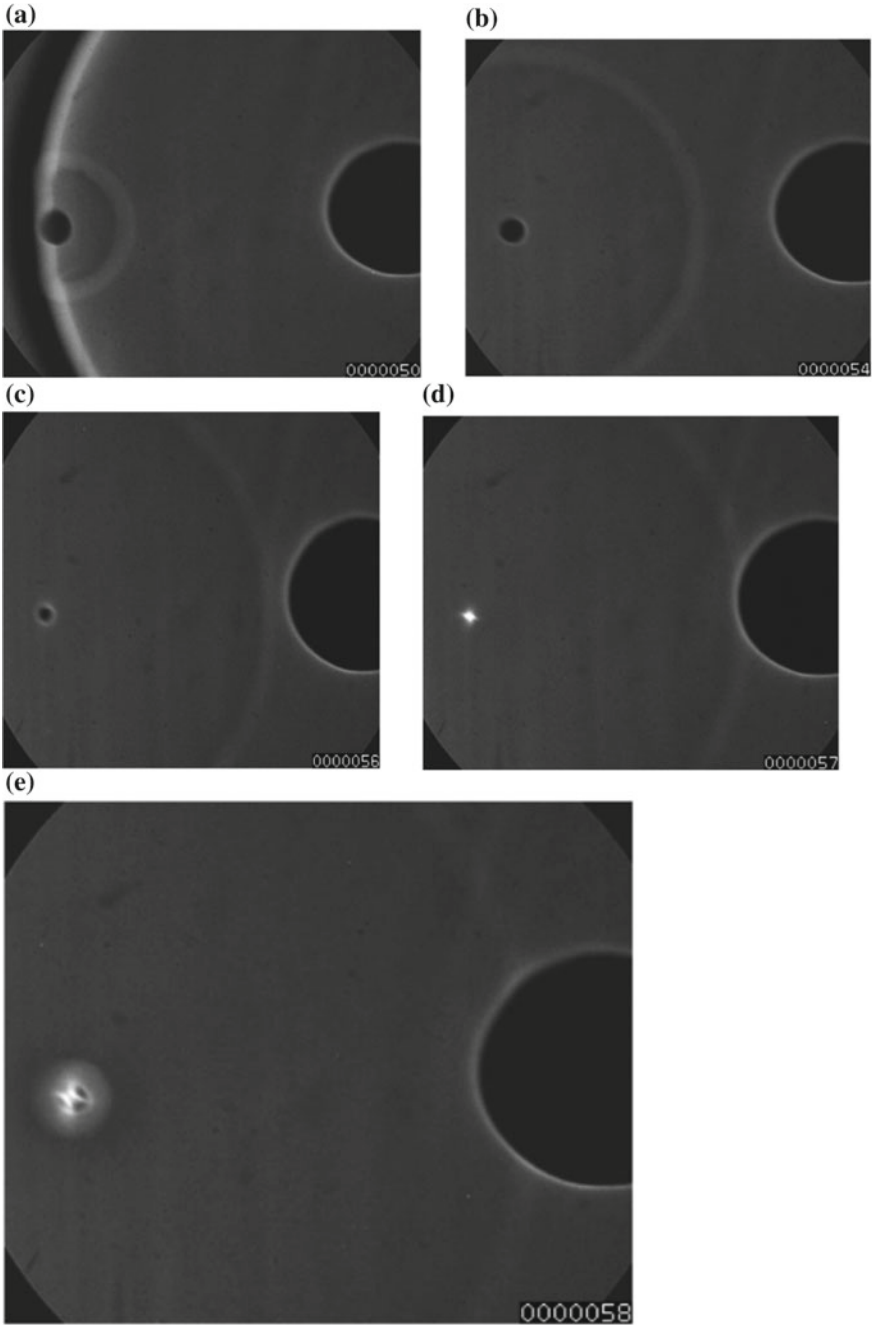

Fig. 9.41 Shock wave bubble interaction in a golden syrup of 70 wt%: **a** #53; **b** #55; **c** #56; **d** #57; **e** #58; **f** #59; **g** #60 (Hirano 2001)

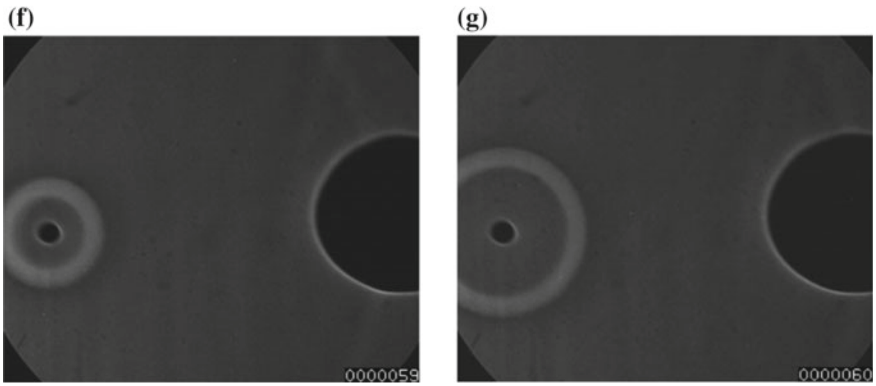

(f) (g)

Fig. 9.41 (continued)

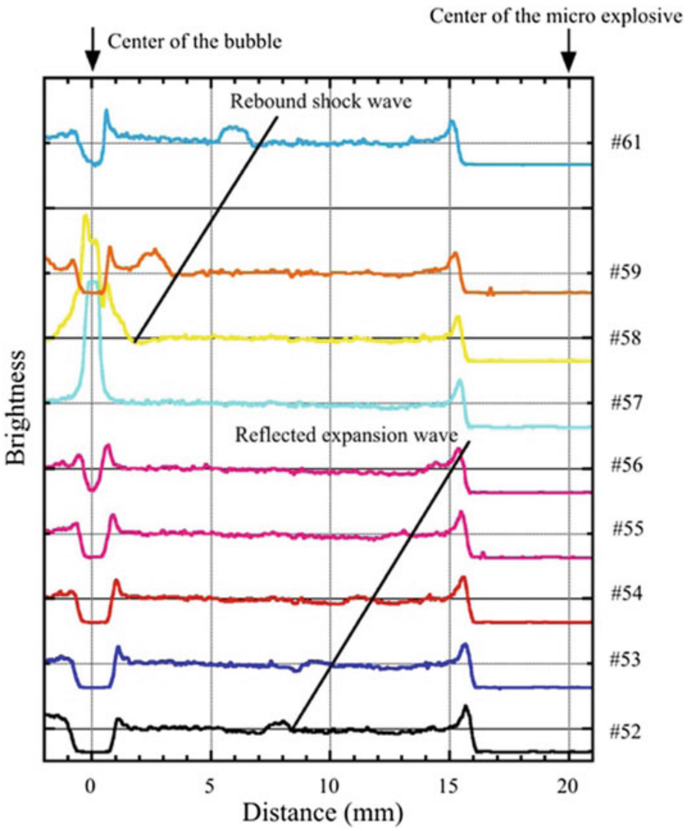

Fig. 9.42 Time variation of brightness of a luminous point in shock/bubble interaction in golden syrup. The summary of Fig. 9.41 (Hirano 2001)

of the gas bubble would be affected to this ratio. The interaction of an underwater shock wave with an air bubble is a typical fast/slow interaction. The ratio of the sound speed in air to that in water is about 0.23. Therefore, in the case of a slow/fast interaction, upon the impingement of a shock wave in a liquid having a slower sound speed, a gas bubble having a faster a sound speed would deform differently from that in the fast/slow interaction.

Yamada (1992) visualized the interaction of a helium bubble with a shock wave in a 1.0cSt PDMS using Ima Con 790 (John Hadland Ltd.) at the framing rate of 10^5 frame/s. The sound speed in helium is 970 m/s, whereas that in 1cSt PDMS is 901.3 m/s. However, the helium filled in the bubble is contaminated with air 50% in volume, then the ratio of the sound speed in the 50% helium-air mixture bubble to that in 1.0cSt PDMS is about 0.6.

The ratio of the acoustic impedance in air bubble to that in water is about 0.007, whereas that in a 50% helium-air mixture to that in 1cSt PDMS is 0.012. Figure 9.43 shows direct shadowgraphs of sequential interactions of a bubble containing a 50% helium-air mixture with a shock wave in 1.0cSt PDMS. The shock wave is generated by exploding a 10 mg AgN_3 pellet. Three sequential pictures were taken at the delay time of 596, 600, and 602 µs, respectively. Inter-frame time of these framing pictures was 2.5 µs. In Fig. 9.43a, the shock wave interacted with a 5% helium-air mixture bubble at the stand-off distance of 10 mm. The reflected expansion wave was observed. The frontal side moved into the bubble and the fain shadow of a reflected shock wave is observed in the seventh frame. The frontal side of the bubble is slightly fattened in the eighth frame. This time instant at which the eighth frame was taken was almost identical with the time instant at which the second frame in Fig. 9.43b was taken.

The bubble had a minimal volume as seen in the second frame in Fig. 9.43b. The bubble explosively expanded in the third frame, which indicates that the shock wave propagating in side the bubble focused at a point, when the bubble volume became minimal at a time instant between the second and third frames. The temperature at the focal point reached high enough to emit luminosity. At the same time, pressures at the focal point became high and spontaneously coalesced into a secondary shock wave. The point at which the secondary shock wave was originated and the point at which the luminosity emitted were almost identical points. This indicates that the reflected shock wave from the curved interface focuses at a point enhancing not only high pressures but also a high temperature enough to spontaneously emit luminosity. From the fourth to the fifth frames, the high pressures explosively blow the bubble as if the high pressures shatter its main structure. Although the main structure of the bubble is deformed and move away from the focal point, a part of the bubble stays at the focal point at which the particle speed is negligibly low. As the main structure of the bubble quickly moves away from the focal point, Therefore, this part looks like a counter jet ejected from the main structure of the bubble. This is not a counter jet but a finger. The slow/fast interaction never agrees with the Neumann effect that is valid only for a fast/slow interface. In conclusion, the sound speed ratio between gas and liquid can decisively govern the wave motion inside the gas bubble (Yamada 1992).

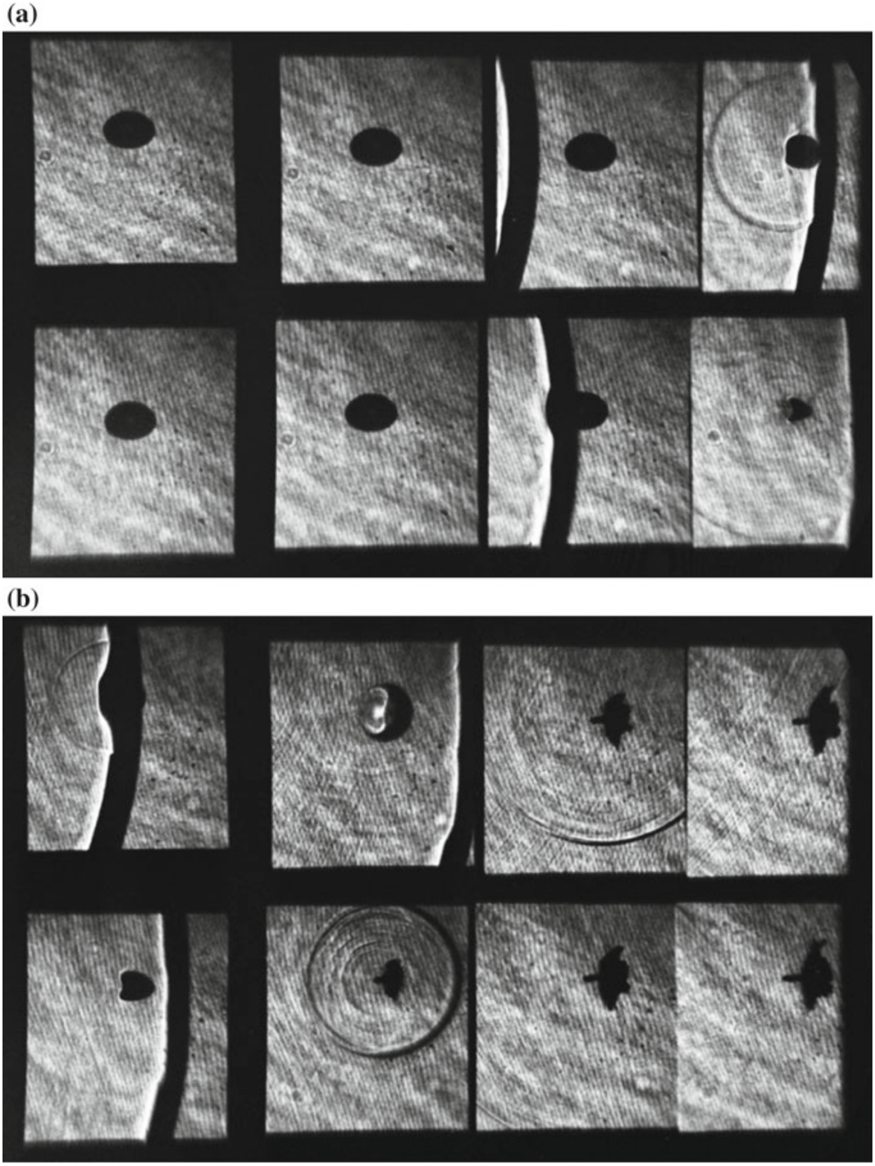

Fig. 9.43 Shock wave interaction with a helium/air bubble in 1cSt PDMA at stand-off distance 10 mm. The shock wave was generated by exploding a 10 mg AgN_3 pelelt. Images were recorded by ImaCon 790 at framing rate of 10^5 frame/s: **a** #92073005, 596 μs after trigger; **b** #92073003, 600 μs after trigger; **c** #92073001, 602 μs after trigger (Yamada 1992)

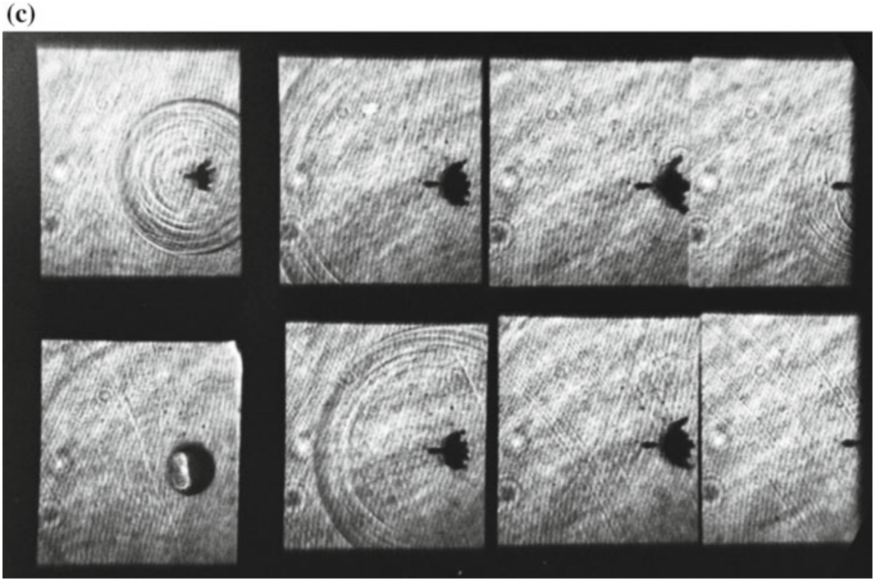

Fig. 9.43 (continued)

In order to demonstrate the slow/fast interaction as seen in Fig. 9.43 in a finer resolution, a sequential observation was carried out (Ohtani and Takayama 2010). Figure 9.44 shows a sequential interaction of a 0.87 mm × 1.22 mm helium bubble with a shock wave generated by exploding a 10 mg AgN_3 pellet in 1cSt PDMS at the stand-off distance of 20 mm. The visualization was conducted in shadowgraph and resulting images were recorded by Ima Con D200 for time interval ranging from 19.6 to 22.0 μs at 250 ns frame interval and at exposure time of 20 ns. Figure 9.45 shows sequential images ranging from 22 to 32 μs at the time interval of 1 μs and exposure time of 20 ns. In Fig. 9.44, the bubble had a minimal volume at 20.5 μs and emitted luminosity and at the same time generated the secondary shock wave. As seen in Fig. 9.43, when a high pressure generated at a focal point shattered the main structure of the bubble, a part of the bubble remained at the focal point forming a stretched finger which resembled a counter jet. The concept of the Neumann effect no longer applicable to interpret the formation of a stretched finger. Wave motions inside the helium-air bubble is only rudely speculated. It is expected that an appropriate numerical simulation would reproduce the formation of a stretched finger.

Figure 9.45 shows the interaction of helium-air bubble with a shock wave generated by exploding a 10 mg AgN_3 pellet in 1cSt PDMS at 1.0 μs frame interval. The jet formation to the stretched finger from the bubble was observed.

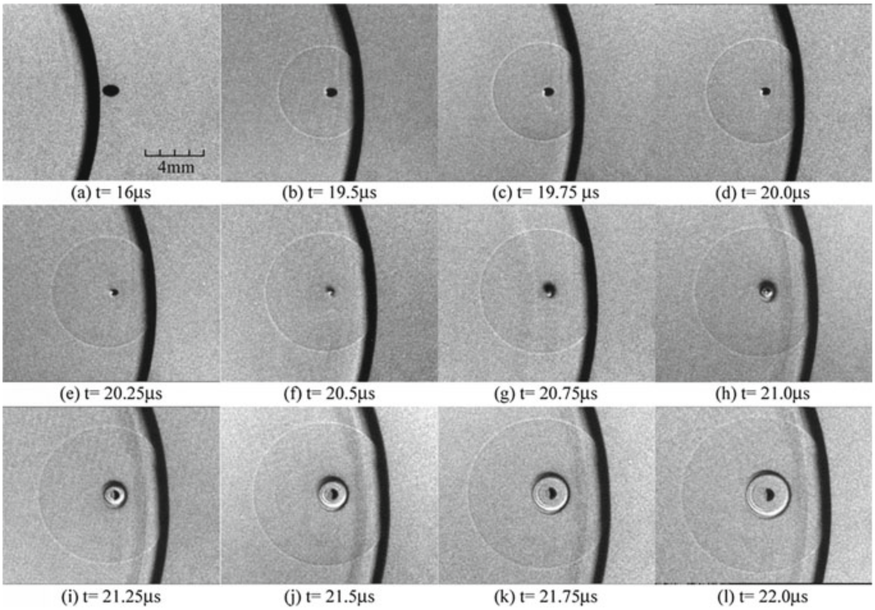

Fig. 9.44 Helium-air bubble interaction with a shock wave generated by exploding a 10 mg AgN_3 pellet in 1cSt PDMS at 500 ns frame interval (Ohtani and Takayama 2010)

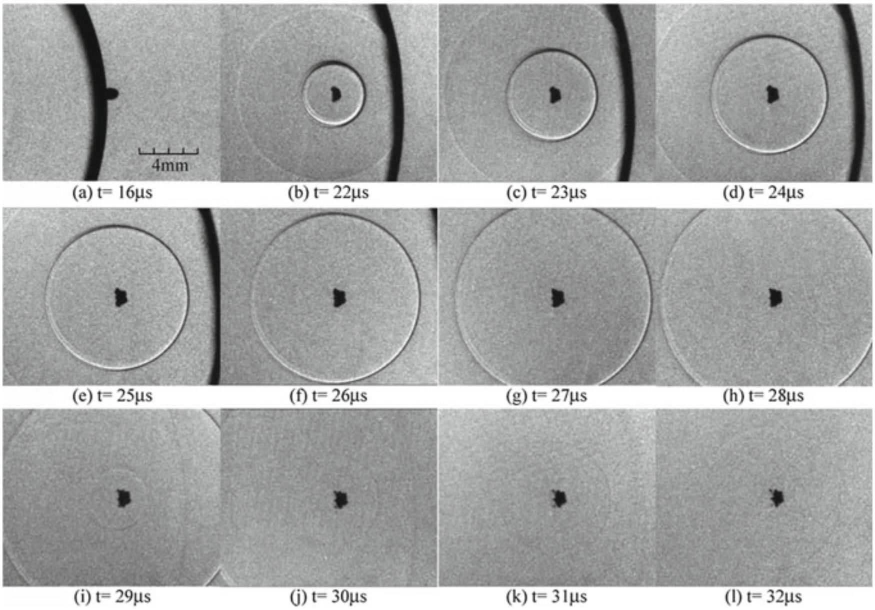

Fig. 9.45 Helium-air bubble interaction with a shock wave generated by exploding a 10 mg AgN_3 pellet in 1cSt PDMS at 1.0 μs frame interval (Ohtani and Takayama 2010)

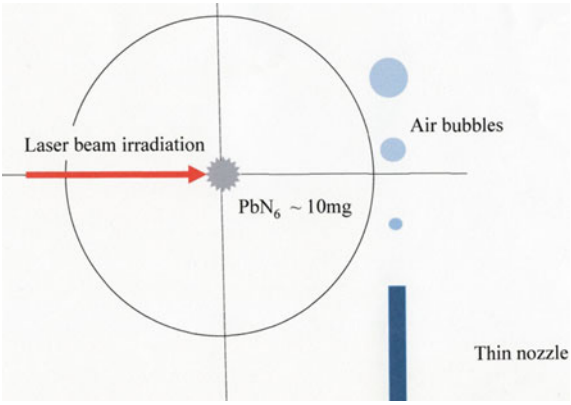

Fig. 9.46 Experimental arrangement of a shock wave interaction with bubble clouds at the stand-off distance 50 mm

9.5.7 *Shock Wave Interaction with Bubble Cloud*

Bubbles were randomly released into water from a capillary tube placed at the bottom of a test chamber and interacted with shock waves generated by exploding a 10 mg PbN_6 pellet. Figure 9.46 illustrates an experimental arrangement. A shock wave was generated at 50 mm stand-off distance from the center of rising bubbles.

Figure 9.47 shows a shock wave interaction with bubble clouds at the stand-off distance 50 mm: single exposure; double exposure interferograms; and their enlargements. Reflected expansion waves were observed only in the double exposure interferograms. The deformation of individual bubbles and the resulting wave interaction dissipated energy and eventually attenuated the shock wave. It is widely known that in maritime engineering and civil engineering, underwater blast waves are bubble effectively attenuated in passing a bubble curtain. Depending on the bubble size and their spatial distributions, an optimal combination of these parameters exists for mitigating underwater blast waves. This analogue experiment is aimed at searching for a similarity parameter between small scale laboratory experiments and field tests. Figure 9.47b, d, f, h are enlargements of Fig. 9.47a, c, e, g, respectively. It is observed that the bubbles are collapsed by the exposures of shock waves generated by neighboring bubble collapses. Smaller diameter bubbles respond quickly but larger diameter ones take time before their collapse.

9.5.8 *Shock Wave Propagation in Bubbly Water*

Japan imports crude oil from Middle East countries. On the way to the Middle East, the oil tankers carry hundred thousand tons of ballast water which contain an abundance of micro marine creatures. Their release into foreign sea water will cause a serious environmental pollution. The International Maritime Organization (retrieved from http://www/imo/home.asp) agreed to explore a technology for

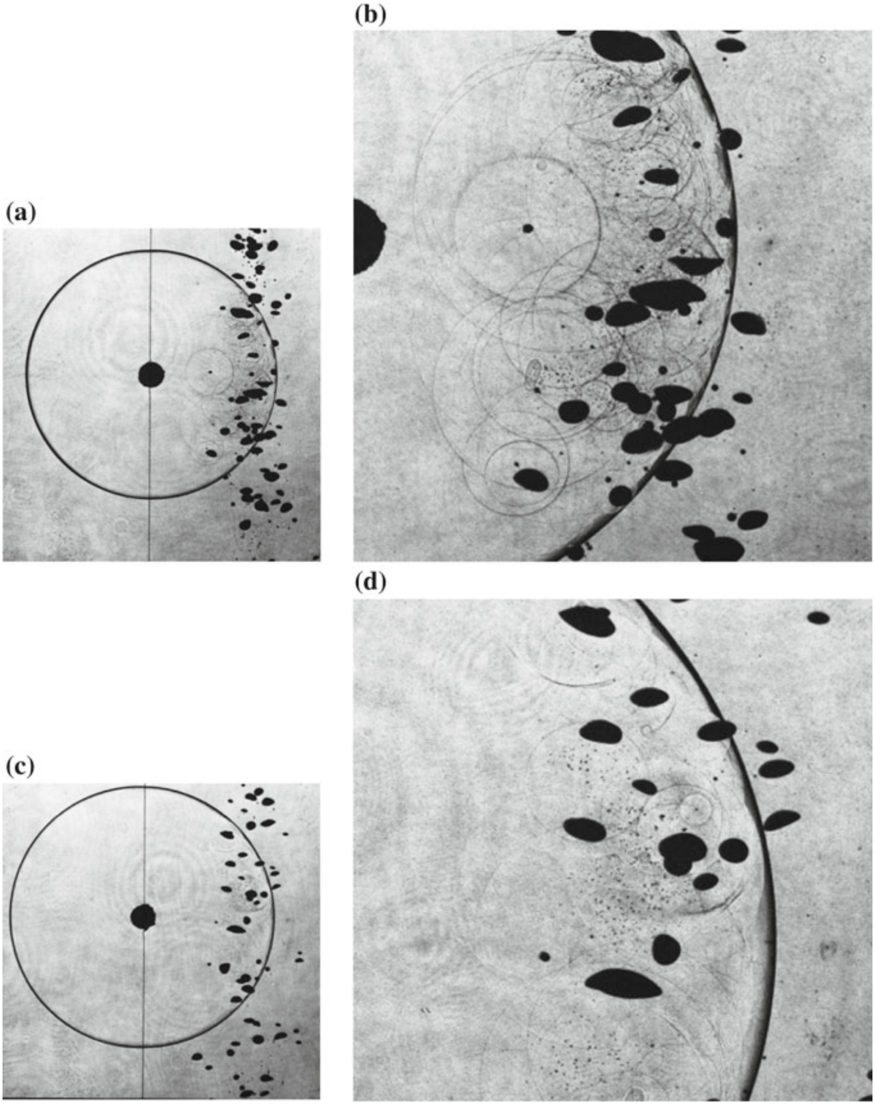

Fig. 9.47 Underwater shock wave interaction with bubble clouds at stand-off distance of 50 mm. Shock waves are generated by exploding a 10 mg PbN_6 pellet: **a** #83013117, 27 μs from trigger point, single exposure; **b** enlargement of (**a**); **c** #83013115, 30 μs shock wave/bubble interaction, single exposure; **d** enlargement of (**c**); **e** #83013113, 32 μs; **f** enlargement of (**e**); **g** #83013103, 40 μs; **h** enlargement of (**g**)

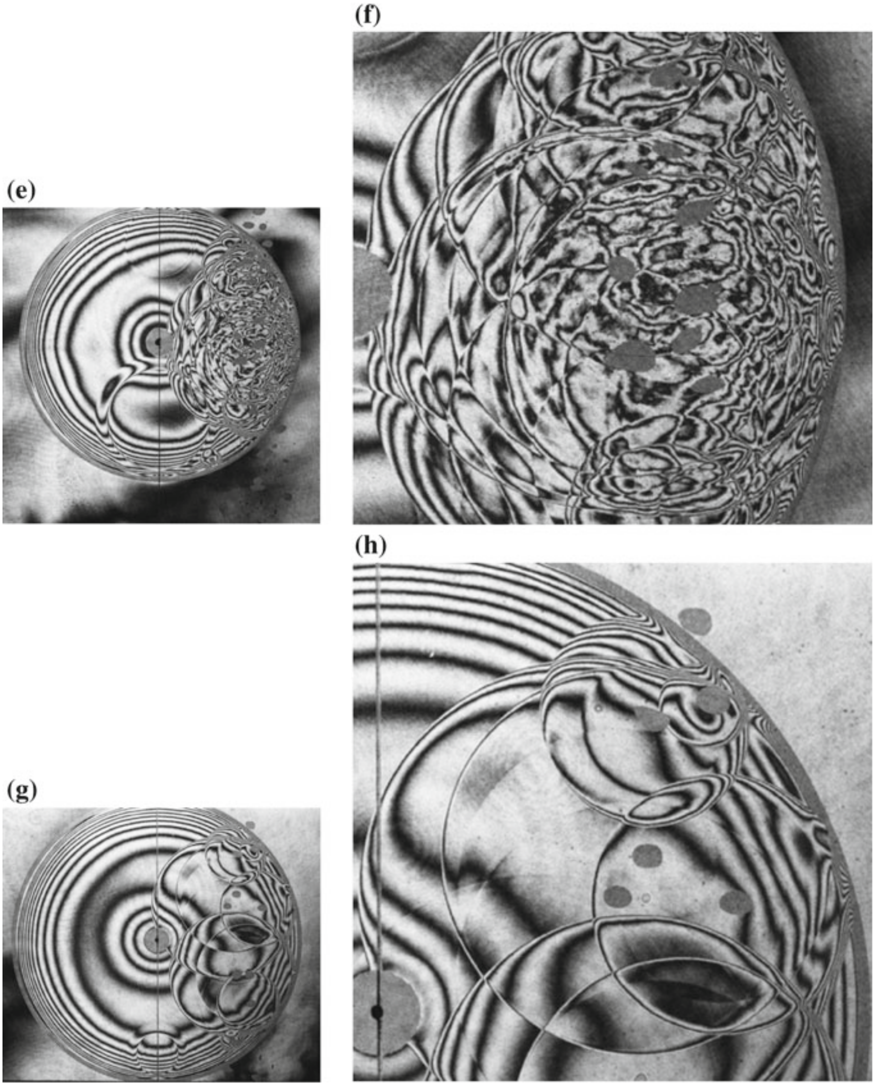

Fig. 9.47 (continued)

efficiently inactivating marine micro-creatures when releasing ballast water in foreign water. Professor Abe in Kobe University proposed a novel method of treating ballast water for inactivation of marine micro-creatures. An analogue experiment was conducted as illustrated in Fig. 9.48a. Micro-air bubbles were generated by swirling water at reasonably high-speed. Resulting micro-air bubbles were stored in a salty water chamber and then circulated into the test section. Figure 9.48b is a histogram of micro-bubbles. The ordinate denotes the production

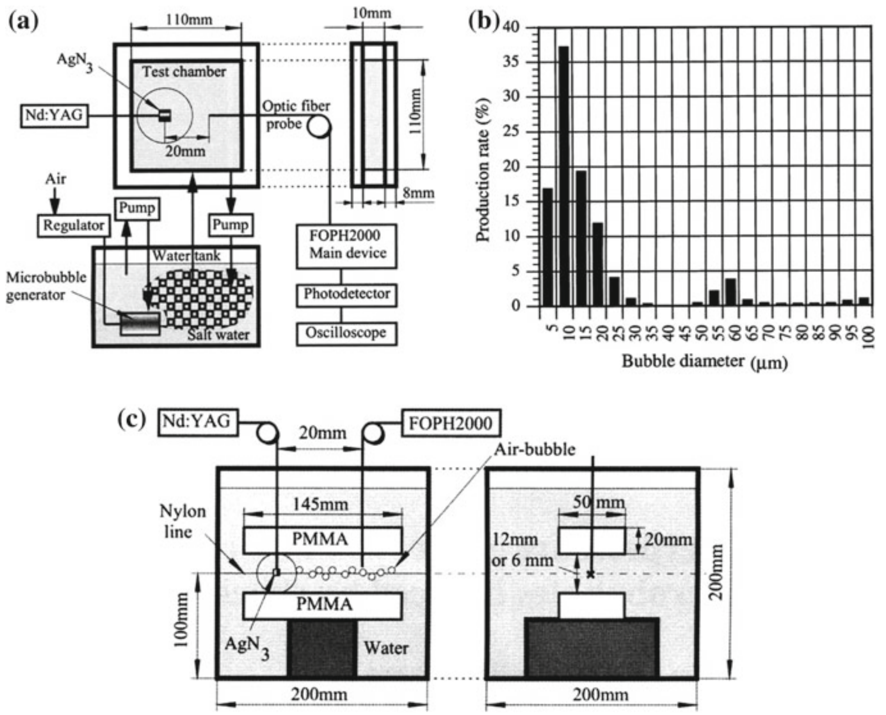

Fig. 9.48 Experimental setup: **a** experimental setup; **b** histogram of micro-bubbles; **c** a test section of 50 mm in width and 6 or 12 mm in height (Abe et al. 2010)

rate, which is a percentage of the bubbles having a specified bubble diameter. The abscissa denotes the bubble diameter in μm. The bubble diameters were distributed from 5 to 25 μm. 35% of the bubbles had a peak diameter of about 10 μm. Underwater shock waves were generated by exploding a 10 mg AgN_3 pellet in a 10 mm wide test section as shown in Fig. 9.48c. Over-pressures were measured with an optical fiber pressure transducer Model FOPH 2000. Shadowgraphs were taken and the images were recorded by Ima Con D200 at the framing rate of 5×10^6 frame/s. Figure 9.48c shows the test section having two 20 mm thick acrylic plates having dimension of 50 mm × 145 mm and the interval was selected either 6 mm or 12 mm.

Figure 9.49a shows a sequential observation of the shock wave propagation in a bubbly water. The shock wave was generated by exploding a 10 mg AgN_3 pellet at the stand-off distance of 20 mm as shown in Fig. 9.48a. The shock wave propagated from right to left. A spherical shock wave generated inside a 10 mm wide channel. The shock wave was spherical until it touched the side walls. The spherical shock wave repeatedly reflected and eventually became a cylindrical shock wave. In Fig. 9.49a, the two coaxial rings were projections of repeatedly reflected spherical shock waves from the side wall and were gradually flattened with elapsing time.

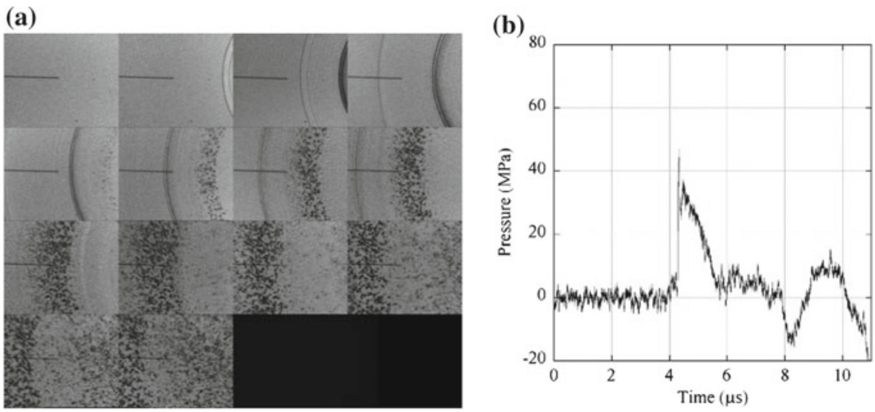

Fig. 9.49 The sequential observation of shock wave propagation in a bubbly water shown in Fig. 9.48a: **a** #090227001 shock wave interaction with bubbly water framing rete of 5 × 10^6 frame/s; **b** pressure profile at early stage (Abe et al. 2010)

Hence, their interval became narrower and eventually merged into a distinct ring shape, which indicated the completion of a two-dimensional cylindrical shock wave. The cylindrical shock wave then interacted with micro-bubbles. Although not observed by shadowgraph, the bubbles quickly collapsed and generated the secondary shock waves. In the third frame, dark double rings indicated the secondary shock waves. Even if they were thick, the side walls were bulged upon the spherical shock wave loading. The degree of the deformation of the side walls were negligibly minute but generated cavitation bubbles. The cavitation bubbles responded to the cylindrical shock wave and instantaneously collapsed. Figure 9.49b shows the time variation of pressures at earlier stage measured by the pressure transducer shown in Fig. 9.49a. The ordinate denotes the pressure in MPa and the abscissa denotes elapsed time in μs. The peak value of the pressure jump at the shock wave was about 40 MPa. The envelop of reflected expansion wave arrived at the pressure transducer at 4 μs after the shock wave and its peak value of expansion wave reached about 15 MPa.

Figure 9.50 shows sequential observations of shock wave/bubble interaction in the test section having 6 mm interval as shown in Fig. 9.48c. A spherical shock wave created by exploding a 10 mg AgN_3 pellet immediately became a two-dimensional shock wave. An arrow marked CS indicate a transient shock wave from a spherical to a two-dimensional cylindrical shock wave. Hence the wave front is slightly broadened. The frame interval is 1.5 μs and the first frame was taken at 6 μs after the ignition. A circular ring shown by an arrow marked B1 was a spherical secondary shock wave generated at a collapsed bubble attached on a thin nylon line placed along the center line. A longitudinal stress wave is transmitted in an acrylic wall, propagating at 2.9 km/s. Then, it was released into water as a precursory wave as shown by an arrow marked OS. Between the first and second frames, the reflection of the secondary shock wave reached the pressure transducer.

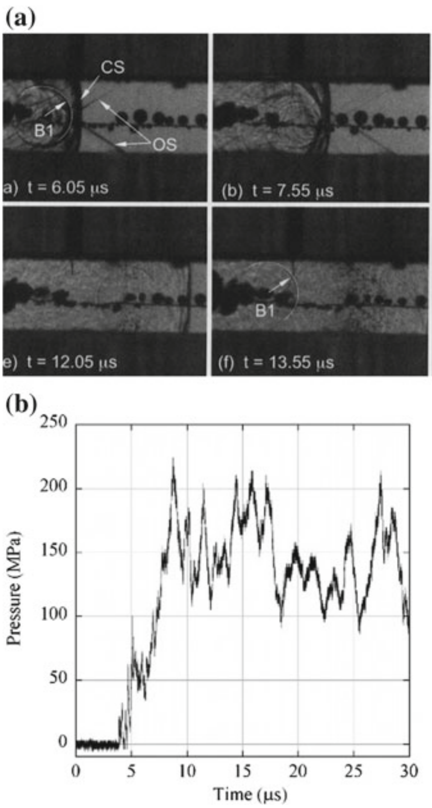

Fig. 9.50 Shock wave/bubble interaction in a two-dimensional duct having a 6 mm interval: **a** sequential observation with Ima Con D200. The shock wave propagated from left to right; **b** pressure variation (Abe et al. 2010)

The optical fiber pressure transducer was shown in the fourth frame. The shock wave successively impinged on air bubbles attached on the nylon line and created the secondary shock waves. In the meantime, its impingement on air bubbles created reflected expansion waves but these are not observed by shadowgraph. Blurred background noises show the reflected expansion waves and secondary shock waves generated by collapsing micro-bubbles. In the sixth frame it was shown by an arrow marked B1. But it was not as intense as that observed in the first frame shown by an arrow marked B1.

Figure 9.50b shows a result of pressure measured. The position of the pressure transducer is seen in the fourth frame in Fig. 9.50a. The ordinate denotes pressure in MPa and the abscissa denotes elapsed time in μs. The impingement of the direct shock wave enhanced pressure up to 60 MPa. However, the impingement of the reflected secondary shock waves from the wall eventually enhance over 200 MPa. If such a high-pressure is repeatedly exposed to micro-marine creatures, they would be gradually eradiated. In this analogue experiment, shock waves are generated by micro-explosions. Then the shock/bubble interaction resulted in the secondary shock wave. Its reflection from the wall of the confined space effectively produced high peak pressure well over 220 MPa. In conclusion, it would be possible to produce higher pressures exceeding 300 MPa, if the diameter and the number density of bubbles are optimized and the shock waves are repeatedly generated by frequent spark discharges in a relatively thin tube. When such an optimization can be achieved, the shock wave assisted eradication of micro-creatures would be practical.

9.5.9 Shock Wave Interaction with a Bubble on an Acrylic Plate

9.5.9.1 Flat Acrylic Plate

Figure 9.51 shows double exposure interferograms of sequential observations of shock wave interaction with a 5 mm diameter air bubble placed on a 7 mm thick acrylic plate. A shock wave was generated by exploding a 10 mg AgN_3 pellet at the stand-off distance of 50 mm (Yamada 1992). Upon a shock wave impingement on the bubble, it started to contract and its frontal side was flattened. The bubble shape was recorded twice firstly when it was set and secondly when synchronized with the event. The two images were superimposed. In Fig. 9.51c–l, the process of the bubble contractions is observed. Flattened bubbles show that the procedure of water jet formation and its impingement on the acrylic wall. The jet impingement on the acryl wall resulted in compression stress wave in Fig. 9.51g, h. Figure 9.51 demonstrates that the holographic interferometry gives quantitatively density distributions not only in water but also in acryl. Photo-elasticity can also produce fringes in photo-elastic materials but the fringes observed in a two-dimensional acrylic plate are iso-density contour lines.

Figure 9.52 shows a shock wave interaction with a 1.7 mm diameter air bubble placed on a 6 mm thick flat acrylic plate. Shock waves were generated by exploding a 10 mg AgN_3 pellet at stand-off distance of 15 mm. Figure 9.52a shows a single exposure interferogram. The expansion wave was reflected from the air bubble and propagated in water. The shock wave impinged on the acrylic plate and induced the stress wave which propagated faster than the transmitted shock wave in water. The reflected shock waves in water were accompanied by expansion wavelets which originated from small bubbles attached on the observation windows from the beginning. Figure 9.52d shows an enlargement of Fig. 9.52c. Figure 9.52f shows a double exposure interferogram: A transmitted shock wave in acryl and other waves were clearly observed but these were not visualized in single exposure interferograms. Figure 9.52g–h shows a later stage. The dark flattened shadow in the center indicates high pressures deforming the bubble surface toward the inside. This is a

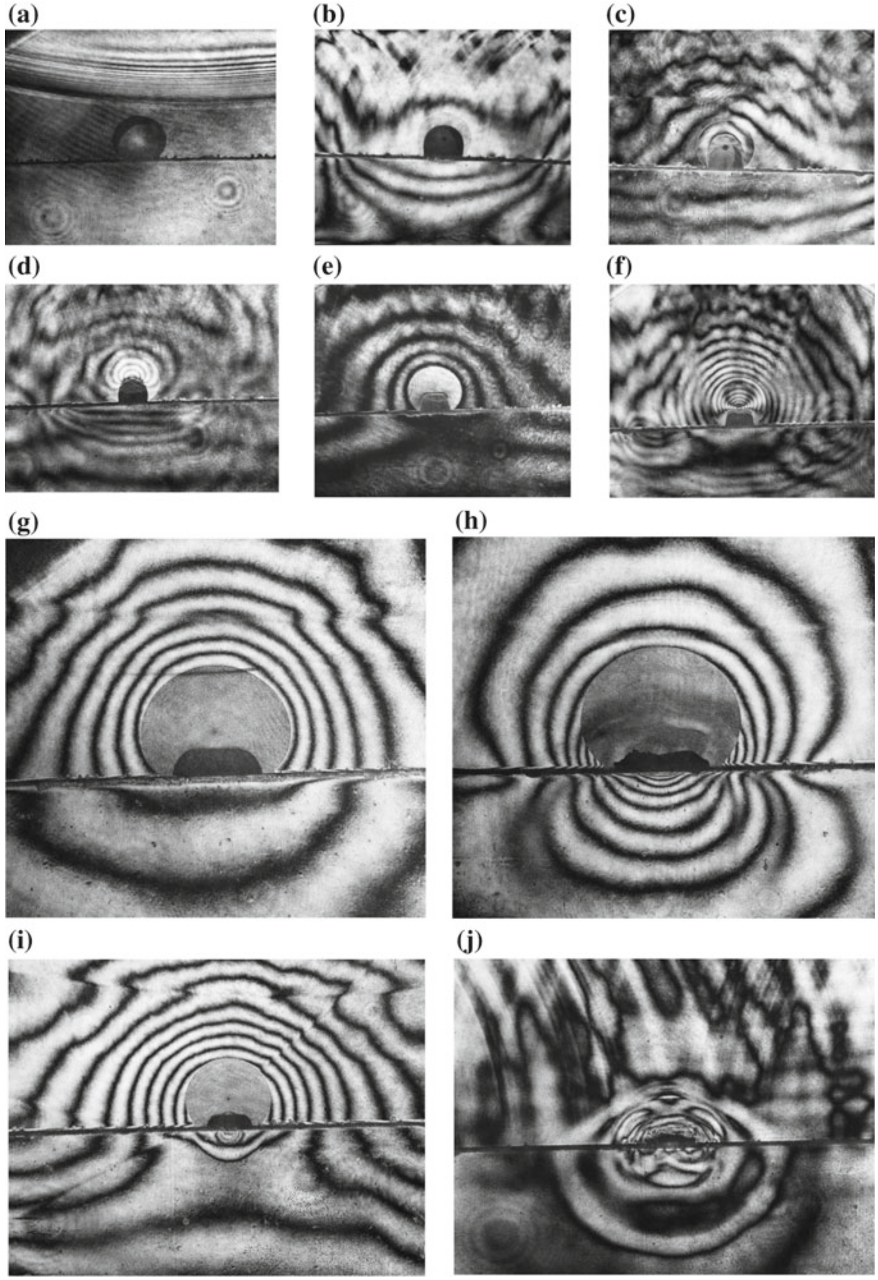

Fig. 9.51 Shock wave interaction with a 5 mm diameter air bubble placed on an acrylic plate and a 10 mg AgN_3 was detonated at stand-off distance of 50 mm: **a** #85012419; **b** #85012406; **c** #85012410; **d** #85012415; **e** #85012504; **f** #85012812; **g** #85012813; **h** #85012807; **i** #85012413; **j** #85012412; **k** #85012505; **l** #85012812

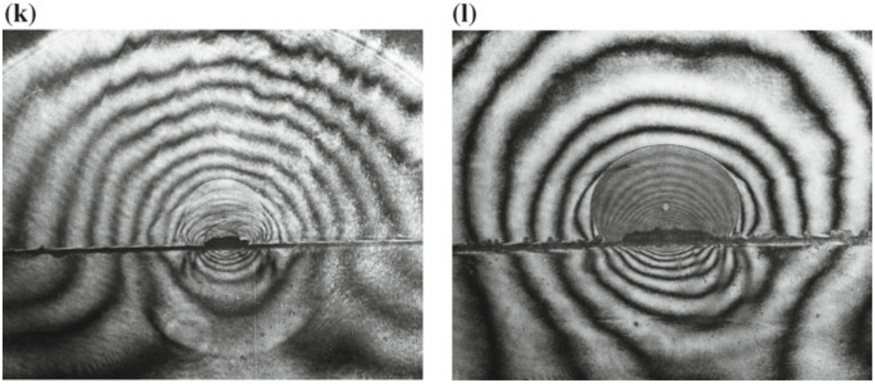

Fig. 9.51 (continued)

stage of jet formation. When the jet impinged the acrylic wall, a stress wave was transmitted in the acrylic plate. Reflected expansion waves and secondary shock waves propagated in water and also in acryl. Waves in acryl moved faster than that in water and was released in water forming an oblique wave. The similar shock wave/interface interaction was already observed when shock waves generated by exploding the explosive pellets interacted with the silicone oil/water interface.

9.5.9.2 V Shaped Groove

Figure 9.53 shows sequential shock wave/bubble interactions with a 1.7 mm diameter air bubble placed on a V-shape groove formed on a 6 mm thick acrylic plate. V shape angles are 45°, 100°, and 135°. A shock wave is generated by exploding a 10 mg AgN_3 pellet at stand-off distance of 15 mm. The bottom of the V shaped groove is a singular point. Hence, the response of the bubble would be unique.

9.5.9.3 Circular Groove

Figure 9.54a shows just before the shock impingement on a 1.7 mm diameter air bubble placed on the bottom of a 1.7 mm diameter two-dimensional groove on a 5 mm thick acrylic plate. Figure 9.54b shows the collapsing air bubble impinged by a shock wave generated by exploding a 10 mg AgN_3 pellet at the stand-off distance of 15 mm.

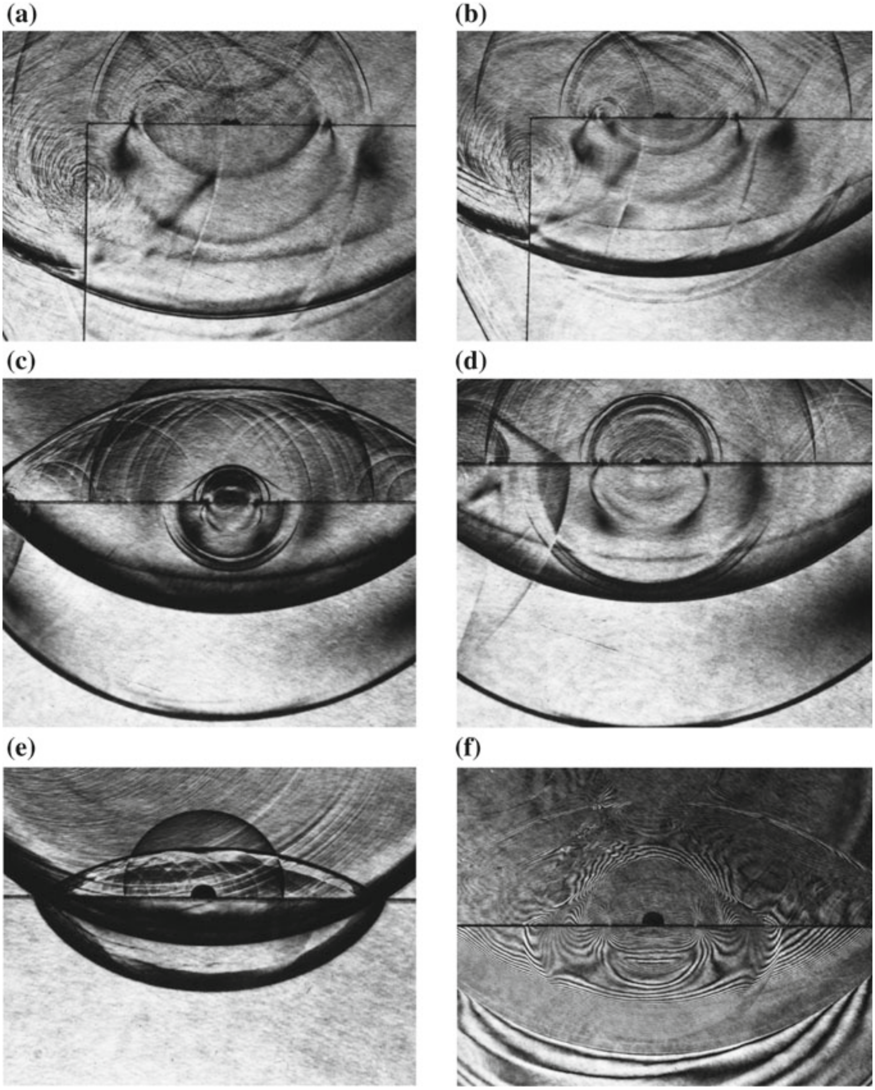

Fig. 9.52 Shock wave interaction with a 1.7 mm diameter air bubble placed on a 6 mm thick flat acrylic plate. Shock waves were generated by the explosion of a 10 mg AgN_3 pellet at stand-off distance of 15 mm, 295.0 K: **a** #86081104, 12 µs after shock wave impingement, single exposure; **b** #86081105, 11 µs, single exposure; **c** #86081106, 8 µs, stand-off distance of 30 mm, single exposure; **d** #86081108, 8 µs, stand-off distance of 30 mm, single exposure; **e** #86081107, 7 µs, single exposure; **f** #86081111, 8 µs; **g** #86081115, 8 µs; **h** enlargement of (**g**)

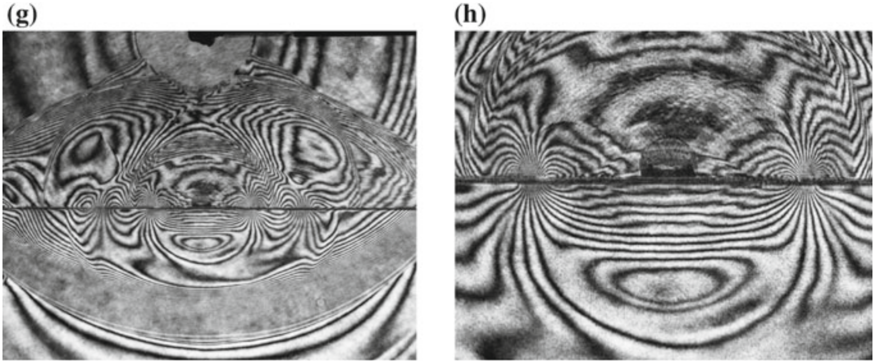

Fig. 9.52 (continued)

9.5.10 Two-Dimensional Bubble

The wave motion inside a spherical bubble cannot be visualized by a conventional visualization method. Then an analogue experiment was conducted to observe the deformation of a two-dimensional bubble impinged by a cylindrical shock wave. Figure 9.55 shows the motion of a 2-D air bubble impinged by a cylindrical shock wave (Yamada 1992). Figure 9.55a schematically shows a 2.2 mm diameter air bubble sandwiched between two acrylic plates separated 3 mm apart. The 2-D air bubble was positioned at 10 mm from the edge of the acrylic plates. A shock wave generated by exploding a 10 mg AgN_3 pellet at the stand off distance of 30 mm.

In Fig. 9.55b, a spherical shock wave impinged on two parallel acrylic plates separated 3 mm apart. The central part of the spherical shock wave propagated along the acrylic plates separated 3 mm interval and was diffracted and repeatedly reflected with its propagation. Eventually a cylindrical shock wave propagated inside the 2-D space. The longitudinal wave propagating in thin acrylic plates did not bother the 2-D bubble.

A ring shape seen in Fig. 9.55b is the edge of a 2-D bubble recorded at the first exposure. When the shock wave impinged, the bubble contracted and its frontal stagnation point was flattened. The deformation grew and eventually became a water jet penetrating the bubble.

In the two-dimensional observation, the fringe number N is given by

$$N = L\Delta n/\lambda, \tag{9.12}$$

where Δn is the variation of refractive index in the test section, L is the length of *OB* path which is 3 mm, and λ is the wavelength of ruby laser. The relationship between refractive index n and density ρ is defined as (Yamada 1992),

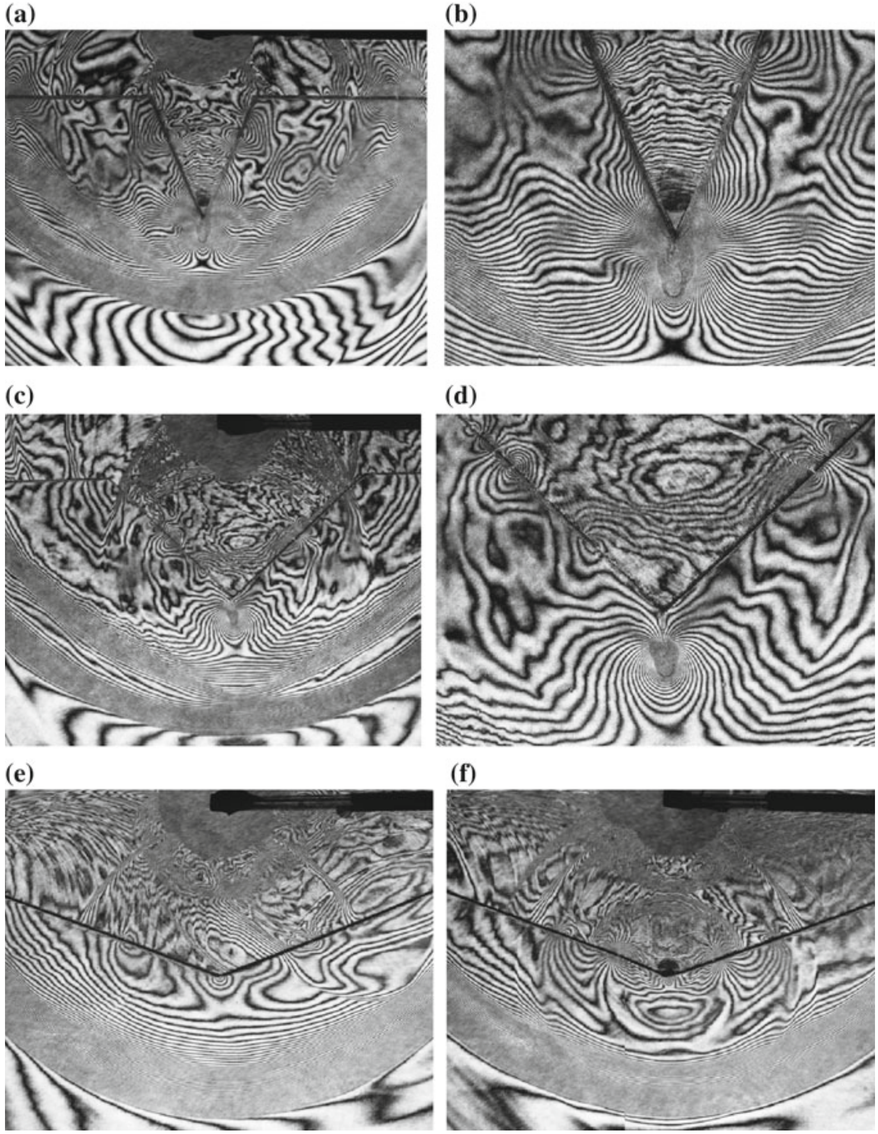

Fig. 9.53 The sequential observation of shock wave interaction with a 1.7 mm diameter air bubble placed at the bottom of V shaped grooves formed on a 6 mm thick acrylic plate. A shock wave is generated by explosion of a 10 mg AgN_3 pellet at stand-off distance of 15 mm, 295.0 K: **a** #86081204, 7 μs from trigger point, 45° groove; **b** enlargement of (**a**); **c** #86081201, 8 μs from trigger, 100° groove; **d** enlargement of (**c**); **e**#86081203, 8 μs from trigger time, 135° groove; **f** #86081202, 8 μs, 135° groove; **g** #86081205, 8 μs, 135° groove, single exposure; **h** #86081206, 8 μs, 135° groove; **i** enlargement of (**h**)

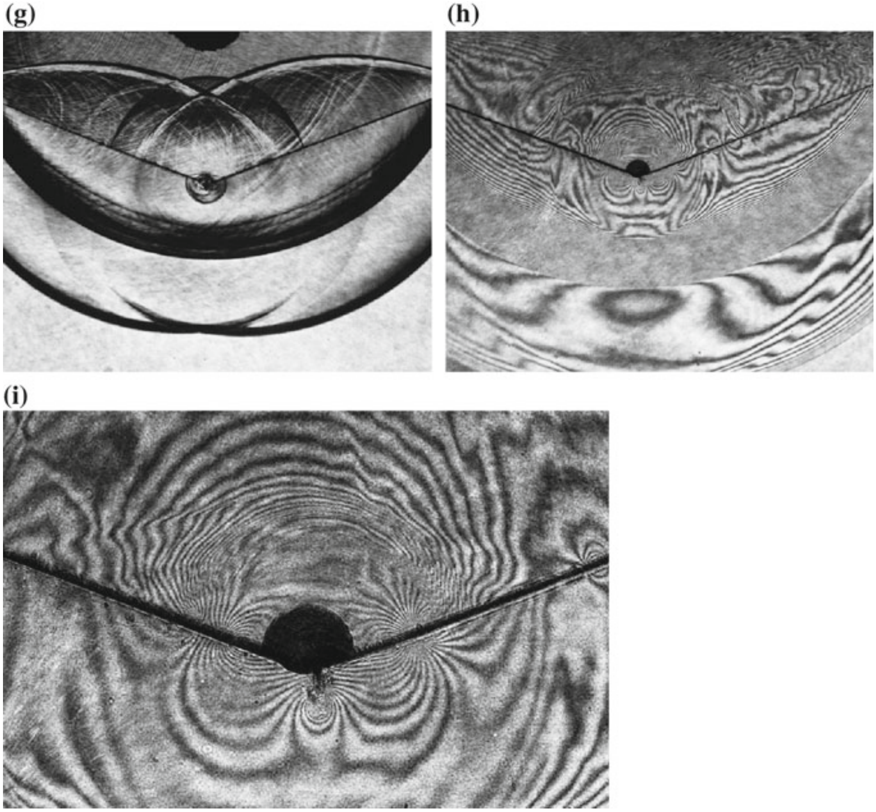

Fig. 9.53 (continued)

$$(n^2-1)/(n^2+2) \propto \rho. \tag{9.13}$$

Hence, one fringe shift in Fig. 9.55 is given by

$$\rho/\rho_0 = 1.266 \times 10^{-3}/\text{fringe}, \tag{9.14}$$

where ρ_0 is the water density at the room condition. Assuming the Tait equation, the density increment per a fringe can be rewritten in the form of pressure ratio p/p_0 per a fringe.

$$p/p_0 = 27.7/\text{fringe}, \tag{9.15}$$

where p_0 is ambient pressure. Hence, the fringe concentration seen in Fig. 9.55b corresponds to the total pressure increment of 13.5 ± 1.4 MPa. Unlike spherical bubbles, two-dimensional water jets do not penetrate the bubble. This is attributable to the fact that the stagnation pressure was too low to deform the 2-D bubble. A 2-D

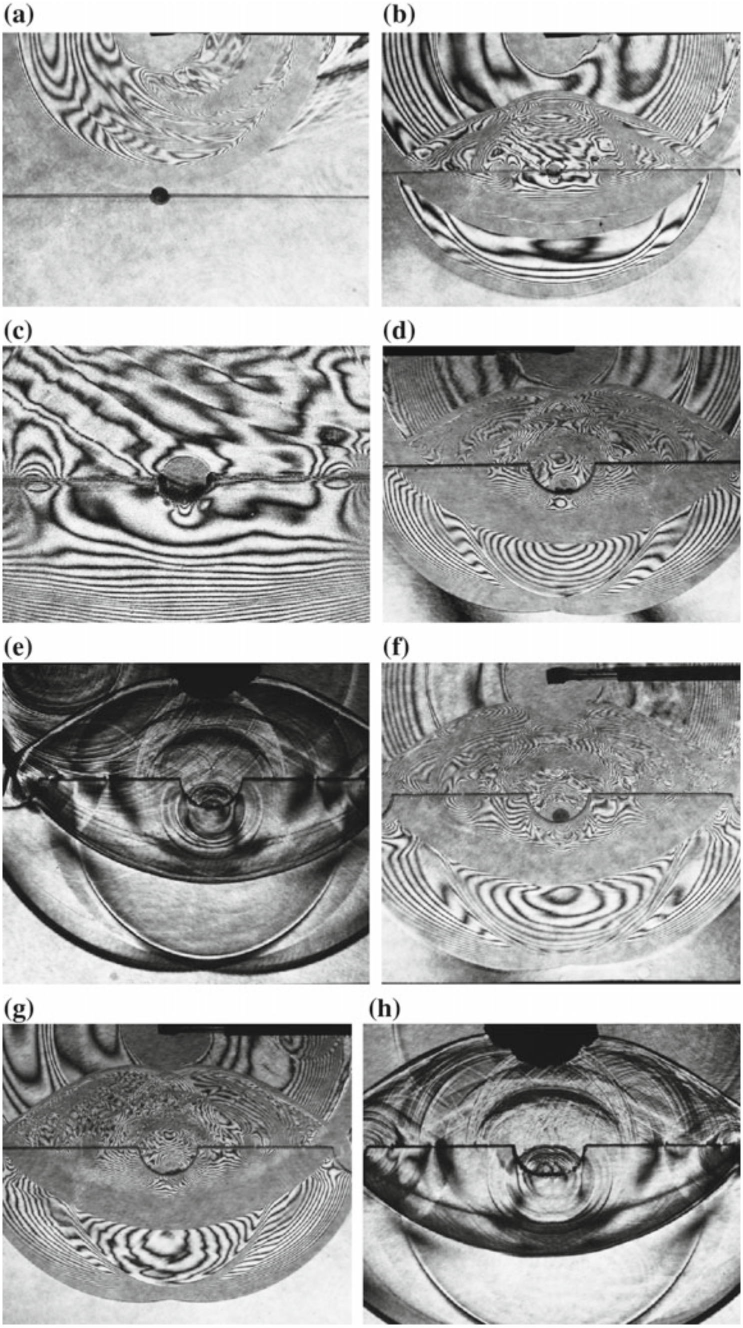

Fig. 9.54 The shock wave interaction with a 1.7 mm diameter air bubble placed on the bottom of a circular groove formed on a 5 mm thick acrylic plate. A shock wave was generated by explosion of a 10 mg AgN_3 pellet: **a** #86081802, 5 μs from trigger point; **b** #86081803, 7 μs; **c** enlargement of (**b**); **d** #86081213, 5 μs **e**; #86081210, 5 μs, single exposure; **f** #86081212, 5 μs; **g** #86081209, 6 μs; **h** #86081208, 6 μs, single exposure

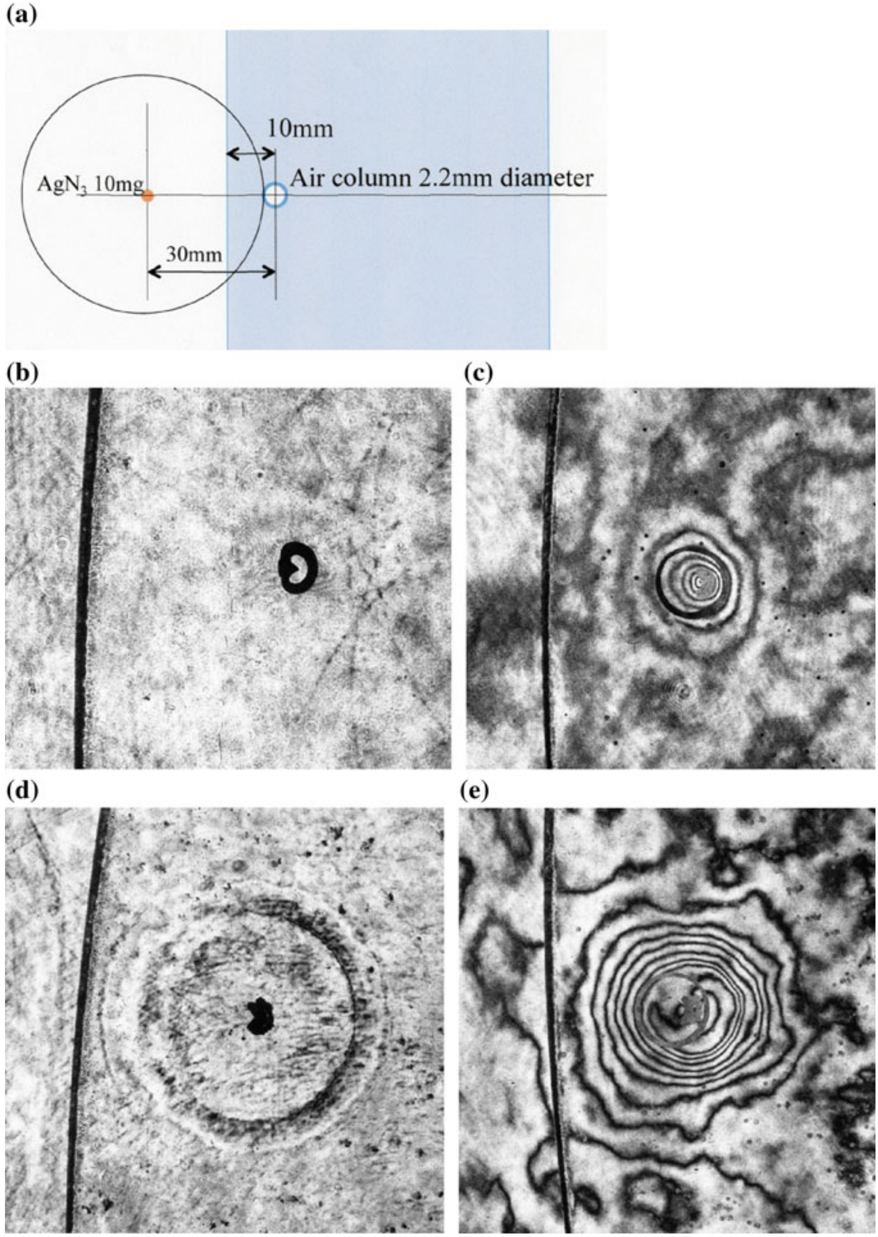

Fig. 9.55 2-D bubble interaction with a shock wave generated by exploding a 10 mg AgN_3 pellet at 1013 hPa, 288.5 K: **a** experimental arrangement; **b** #87031606, single exposure; **c** #87031630; **d** #87031604, single exposure; **e** #87031613

bubble expands more irregularly than a spherical bubble does (Takayama 1987). It should be noticed that although the 2-D bubble has 2.2 mm diameter and 3 mm high, their response to the shock wave exposure is different from an ideal 2-D air column. The edges of the 2-D bubble are stuck at the acrylic plate's surface and would not move as freely as a spherical bubble.

9.5.11 Sympathetic Explosion

If two explosives are in water and one of them was exploded, the resulting shock wave may ignite the neighboring explosive. This is the so-called sympathetic explosion (Nagayasu 2002). Depending on the stand-off distance between the two explosives, the ignition of the neighboring explosive hardly occurred. However, if air bubbles are attached on its surface, the explosive would be ignited spontaneously as soon as the shock wave of the neighboring explosive reached on its surface. Figure 9.56a demonstrates sympathetic explosions. Two PbN_6 pellets of 5.5 and 5.6 mg in weight were glued on a cotton threads at the stand-off distance of 4 mm. Air bubbles are attached on the lower one. The upper one was ignited first and about 2.6 μs later, the lower one detonated. The grey shadows are explosion product gas bubbles taken at the second exposure. The hot spot created inside the collapsing the air bubble triggered the lower explosive. The difference of the radii of the two spherical shock waves indicates the delay time of the ignition. Figure 9.56b shows a single exposure interferogram of sympathetic explosion of two PbN_6 pellets of about 6 mg in weight vertically arranged at stand-off distance of 8 mm. The upper one triggered the lower one. The shape of the detonation product gas bubble of the upper explosive became irregular initiated by the shock wave of the sympathetic explosion. Figure 9.56c shows a single exposure interferogram: two PbN_6 pellets of 6 mg each are positioned horizontally at the stand-off distance of 8 mm. The left one exploded first and the right one exploded. In Fig. 9.56d, two 5.4 mg PbN_6 pellets separated horizontally 8 mm apart. The right one exploded first and the left one exploded. Spherically shaped wavelets are remnants of secondary shock waves created by the collapse of small bubbles attached on the cotton thread. Figure 9.56e, f shows sympathetic detonation of explosives arrayed in a line on a cotton thread.

9.6 Ultrasonic Oscillatory Test

A preliminary study started in 1980 aiming at the development of Japan's geothermal power generation. An ultrasonic oscillatory test was adopted to test appropriate materials that would resist against corrosive steam and vapor mixtures extracted from underground heat sources. Metal pieces were oscillated in ultrasonic frequency in liquids for wide ranges of temperatures and pressures which would simulated such harsh environments (Sanada et al. 1983). Generations and collapses

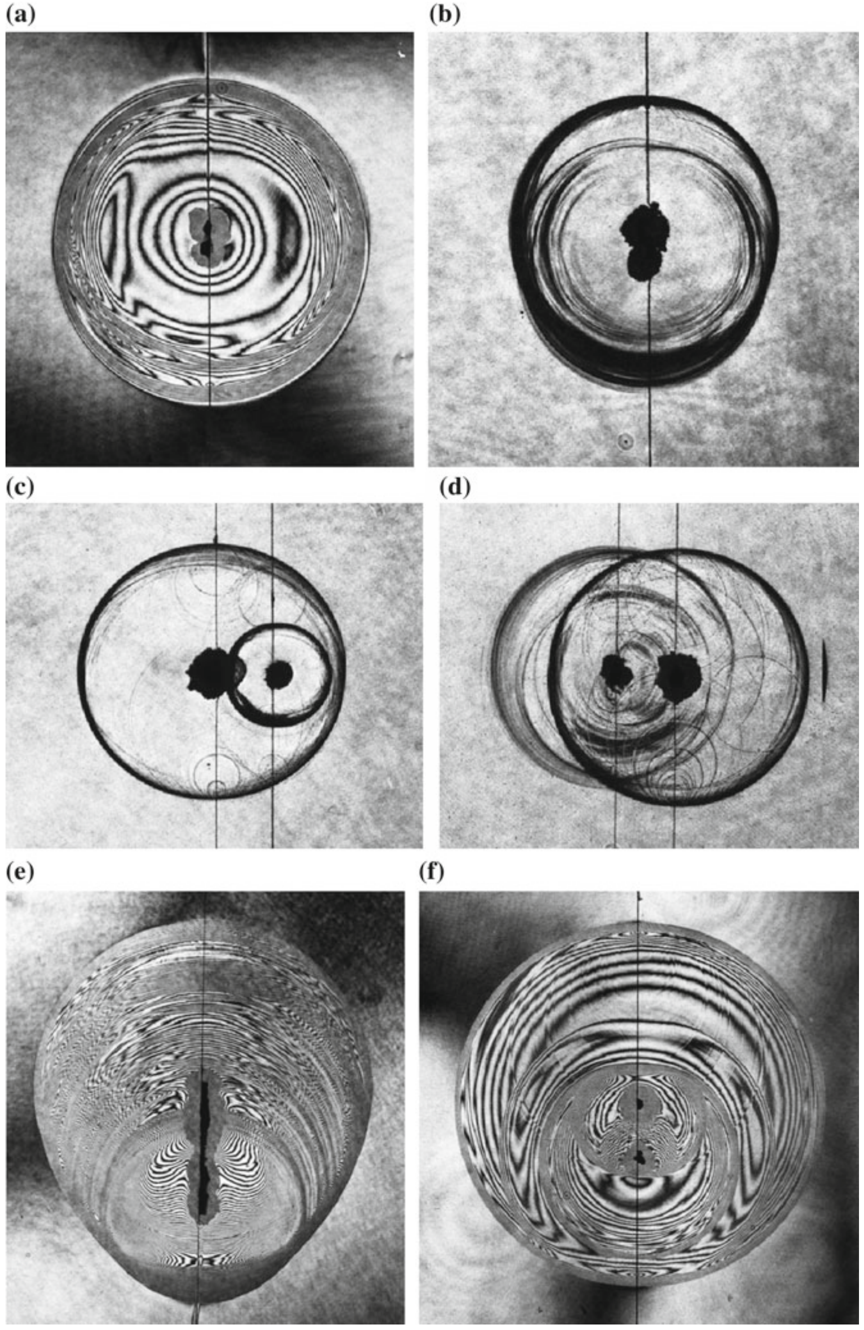
(a)
(b)
(c)
(d)
(e)
(f)

◂**Fig. 9.56** Sympathetic explosion caused by bubble collapse at 1013 hPa, 287.4 K: **a** #83112802, 16 μs from ignition, 5.5–5.6 mg PbN_6 pellets were glued vertically on a cotton thread at the stand-off distance of 4 mm; **b** #83112803, 9 μs from ignition, 5.8–5.9 mg PbN_6 pellets, vertically at the stand-off distance of 4 mm; **c** #83113004, 9 μs from ignition, 6.0–6.0 mg PbN_6 pellets, horizontally at stand-off distance of 8 mm; **d** #83120512, 7 μs from ignition, 5.4–5.4 mg PbN_6 pellets, horizontally at stand-off distance of 8 mm; **e** #83113007, 8 pieces of 5 mg PbN_6 pellets in a row; **f** #84031308, 5–5 mg PbN_6 pellets, vertically at stand-off distance of 8 mm, 25 μs

of bubbles on the metal specimens at a high-frequency are supposed to reproduce corrosive environments. Then ultrasonic oscillatory tests are extensions of shock/bubble interactions. Single exposure interferometry and high speed streak photography (ImaCon 790, John-Hadland) were intensively applied to the observation of bubble motions and subsequent generations of shock waves. For conducting the streak recording, an Argon-ion laser of 500 mW and a mechanical shutter having a 1 ms long opening time interval and a combination of 100 μs opening time and 100 μs closing time were used.

The experiment was conducted in a 200 mm diameter and 150 mm wide stainless steel chamber and the test liquid was ion exchanged water. The test chamber was designed to withstand against pressures ranging from 0.1 to 0.5 MPa and temperatures ranging from 272 to 373 K. Observation windows were 150 mm diameter and 20 mm thick optical glasses. An ultrasonic oscillator had a horn shaped oscillatory section which was driven by a 500 W motor and installed vertically into the test chamber. At the tip of the oscillatory horn, a 16 mm diameter test metal piece was attached and was immersed in test water by 3 mm in depth. The horn was driven at frequency of 17.7 kHz and a half amplitude of 17.5 μm. The phase angle of the horn's oscillation cycle was synchronized with the irradiation of a Q-switched ruby laser beam. The high-speed framing and streak observations were used to supplement holographic observations. The oscillator displacement x is defined by,

$$\mathrm{x} = \mathrm{a}\,\sin 2\pi\omega \mathrm{t}, \tag{9.16}$$

where a is amplitude 17.5 μm and ω is frequency 17.7 kHz. One cycle of oscillation takes approximately 56 μs. Although the amplitude is very small, its acceleration eventually induces a force of the order of magnitude of 10^4 g where g is the gravitational acceleration. This force exceeds even the spalling strength in water attached to the test piece surface. Therefore, cavitation bubbles are created instantaneously. Sequential holographic images are presented in Fig. 9.57 and a streak photograph is shown in Fig. 9.58.

Figure 9.57a shows sequential single exposure interferograms synchronized with the phase angle of every π/4. The upward motion of the image corresponding to the oscillator's recess motion induced a very high tensile force on the oscillator's surface and hence cavitation bubble clouds are created. Dark small spots seen in Fig. 9.57 shows the temporal distribution of bubbles underneath the oscillator. The oscillator's forward motion compressed water and resulted in compression waves, which collapsed bubbles generating secondary shock waves on the oscillator's surface. Shock waves interacted then with the neighboring bubbles and collapsed

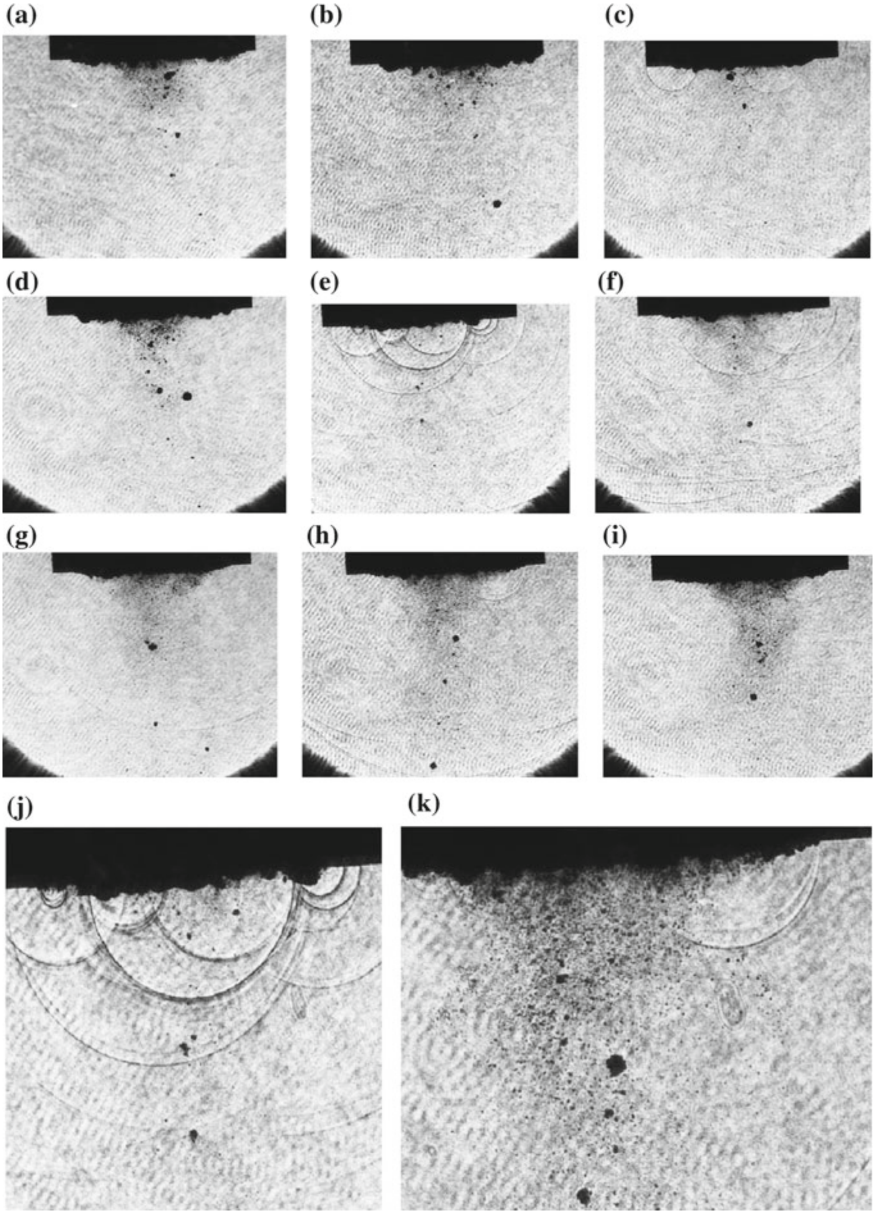

Fig. 9.57 The ultrasonic oscillation at 1013 hPa, 290 K: **a** #82112602, phase angle 0; **a** #82112603, π/4; **c** #82112604, π/2; **d** #82112605, 3π/4; **e** #82112606, π; **f** #82112607, 5π/4; **g** #82112608, 3π/2; **h** #82112609, 7π/4; **i** #82112610, 2π; **j** enlargement of (**e**); **k** enlargement of (**h**)

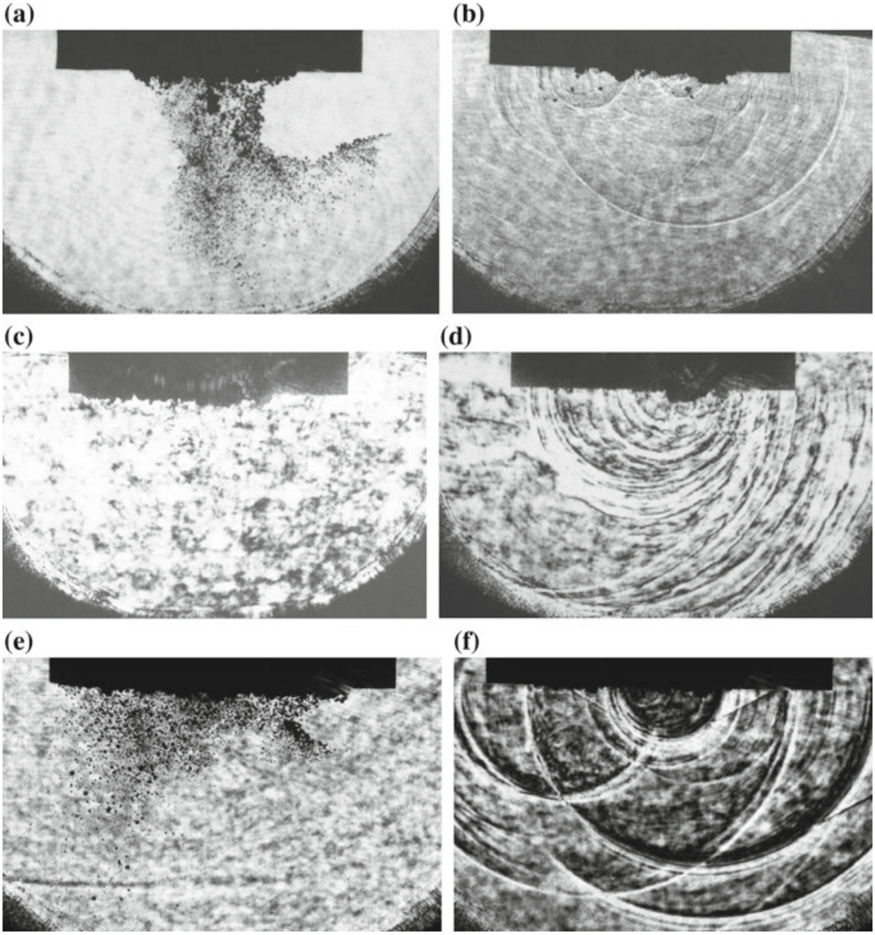

Fig. 9.58 The sequential observation of ultrasonic oscillation at 0.2 MPa, 283 K: **a** #81121765, 2π/3; **b** #81121766, π; **c** #81121767, 4π/3; **d** #811217658, 5π/3; **e** #81121769, 2π; **f** #81121770, π/3

them. Such a chain reaction continues until the oscillator's forward motion ceases. The successive oscillatory motion creates a convective flow which slowly circulates in the entire test chamber. The circulation flow is directed at first downward and later moved upward close to the oscillator. Figure 9.57j, k shows enlargement of Fig. 9.57e, h. In Fig. 9.57a, the initial phase angle allocated was π/4 and the phase angle was increased every π/4 until in Fig. 9.57i the phase angle reached 2π. In Fig. 9.57e, the number of shock wave so far observed were maximal at the phase angle π.

Figure 9.58 shows sequential single exposure interferograms. It is observed that the generation of bubble clouds were not synchronized with the oscillator's cycle, this implies that the hysteresis exists between the oscillatory motion and the number of bubbles observed in the field of view. Figure 9.58a–f shows sequential observation at the test pressure of 0.2 MPa and the phase angle attached to the individual images increased from 2π/3 at every π/3. The phase angle 0 should imply the initiation of the oscillator nut. In Fig. 9.58a at the phase angle 2π/3, a bubble cloud is ejected downward and then due to the buoyancy, individual bubbles slowly moved upward. Eventually, by chance, the bubble cloud resembled a bonsai pine tree, which is indicating the presence of a convective flow. Bubbles migrate following the convective motion and periodically were exposed to pressure fluctuations. However, bubbles migrating in this convective flow look hardly collapsed and hence secondary shock waves are hardly observed. In Fig. 9.57b, the bubble clouds disappear and shock waves appear. The most of shock waves have their center attached to the oscillator's surface. A secondary shock wave so far created successively promoted the neighboring bubbles to oscillate. Eventually they collapsed and produced the secondary shock waves. Then, the bubbles attached to oscillator's surface collapses similarly to a chain reaction. The streak recording shown in Fig. 9.60a clearly explain the observation shown in Fig. 9.57.

Figure 9.59 shows the sequential observation in an elevated test condition at 0.3 PMa and 323 K. As the water temperature is higher than the room temperature, the number of bubbles generated at this condition are much more than those induced at room temperature. Then the number of secondary shock waves are increasing. Figure 9.59d shows a shock wave whose center was uniquely away from the oscillator' surface. The bubble is presumably attached to the window glass. The bubble formation and the secondary shock wave generation were strongly affected by the test condition.

Figure 9.60a is a streak photograph and shows cavitation bubbles induced by ultrasonic oscillation and trajectories of resulting secondary shock waves. Grey oblique lines indicate trajectories of secondary shock waves and a vague grey shadows indicate the initiation and extinction of cavitation bubbles appearing for about 40 μs. Secondary shock waves and also cavitation bubbles appear repeatedly at every 56 μs. It is estimated that by counting the number of secondary shock wave trajectories, about one third to one half of cavitation bubbles transited to the secondary shock wave. The ordinate denotes the diameter of the oscillator 16 mm. The abscissa denotes elapsed time. The bubble cloud is densely populated at the center of the oscillator and is maintained for about 40 μs. When the bubble cloud disappears, at several μs of pause secondary shock waves repeatedly appear and soon terminate. As seen in single exposure interferograms secondary shock waves have their center attached to the oscillator' surface. In the streak photograph, a 0.15 mm wide slit was placed on the oscillator surface. Hence the center of the most of bubbles are located inside the slit width. Therefore, the trajectory inside the slit width of 1.5 mm is not reliable.

Tracing the trajectory of a shock wave in Fig. 9.60a, the time variation of a bubble radius is determined as shown in Fig. 9.60b. The ordinate denotes a radius of a shock wave in mm and the abscissa denotes elapsed time in μs. In interpolating the trajectory, the speed of the shock wave can be obtained as shown in Fig. 9.60c. The shock wave attenuates very quickly to a sound wave already at 4 mm from the

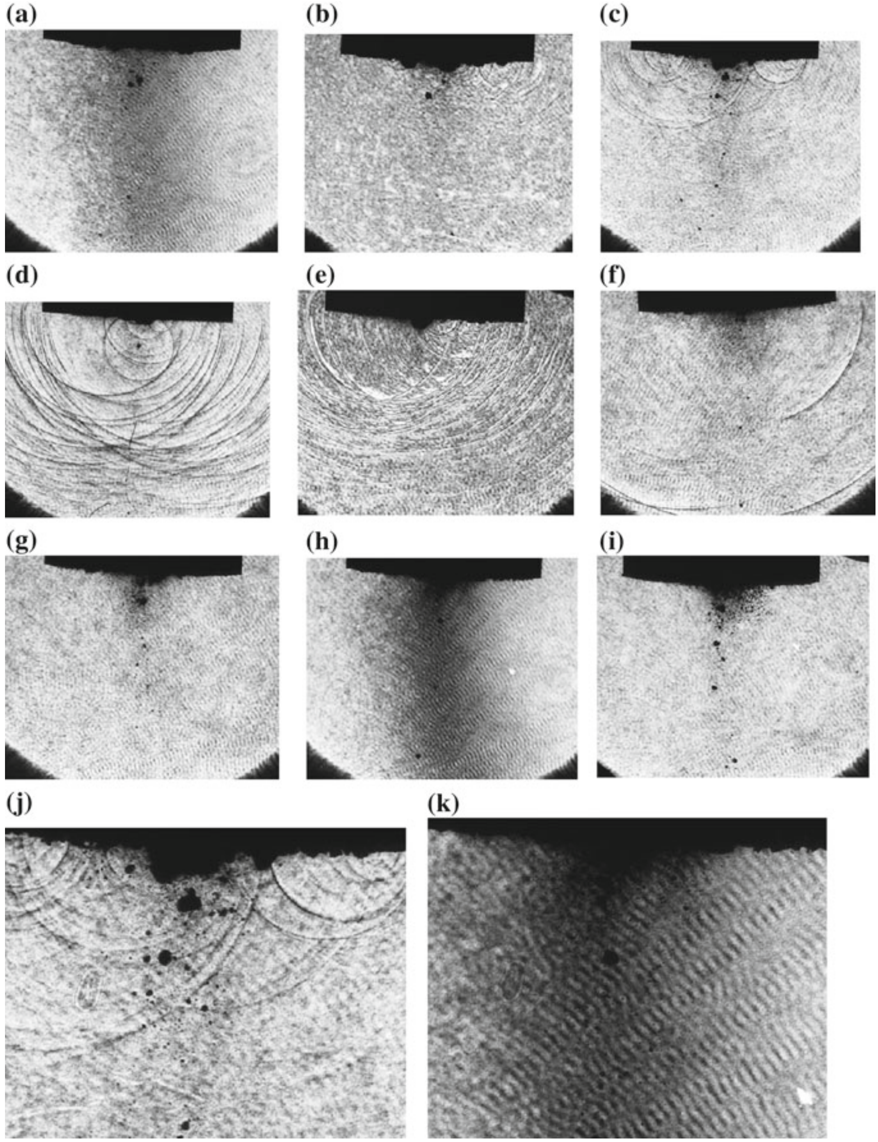

Fig. 9.59 Ultrasonic oscillation at 0.3 MPa, 323 K: **a** #82112532, phase angle 0; **b** #82112533, π/4; **c** #82112534, π/2; **d** #82112535, 3π/4; **e** #82112536, π; **f** #82112537, 5π/4; **g** #82112538, 3π/2; **h** #82112539, 7π/4; **i** #82112540, 2π; **j** enlargement of (**e**); **k** enlargement of (**h**)

center. At 4 mm from the center, the estimated shock Mach number Ms is 1.1. The pressure behind a shock wave of Ms = 1.1 is approximately 800 MPa. This overpressure is high enough to spontaneously erode the surface of hydraulic machine elements made of high-strength carbon steel. In the previous sequential

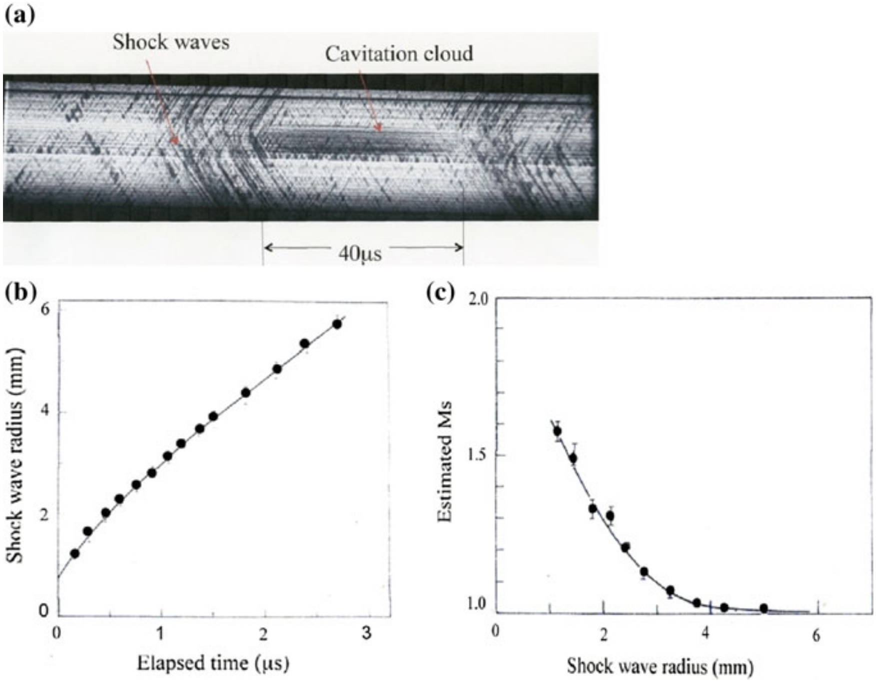

Fig. 9.60 Trajectory of secondary shock wave and its estimated speed: **a** streak photograph of bubble formation and cavitation bubble collapse, #82120820 at 1013 kPa, 293 K; **b** trajectory of a bubble; **c** speed of shock wave generated at collapsing bubble (Sanada et al. 1983)

observations, the oscillator's recess motion generated bubble clouds which were distributed in the vicinity of the surface. The shapes of secondary shock waves were hemi-spherical which indicated that most of collapsing bubbles were located on the oscillator's surface. The presence of circular shaped secondary shock waves was rather exceptional because all the bubbles so far generated did not necessarily collapse, but migrated downward in the convective flows and was eventually dissolved in water.

In order to examine the structure of bubble clouds, a shock wave was loaded over the oscillator. Figure 9.61 shows single exposure interferogram of shock wave propagation over the oscillator. The visualization was conducted to detect the distribution of migrating bubbles over the oscillator, a 10 mg PbN_6 pellet was exploded at about 13 mm away from the oscillator surface. The shock wave over-pressure at the stand-off distance of 20 mm was about 25 MPa so that all the water vapor hit by such a strong shock wave collapsed at once and created the secondary shock waves. Hemi-circular rings were spherical shock waves originated from bubbles which were distributed on the oscillator surface. Circular rings were spherical shock wave originated from bubbles distributed away from the oscillator

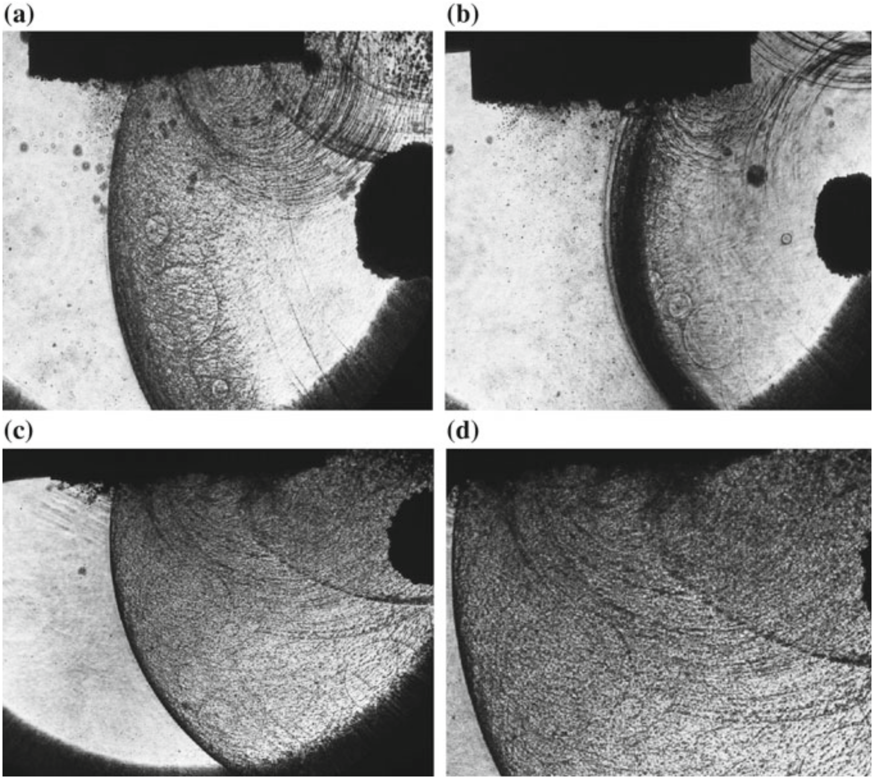

Fig. 9.61 Interaction of spherical shock waves with bubble cloud: **a** #82112973, 77 μs from trigger point; **b** #82112975, 91 μs; **c** #82113035, 31 μs; **d** enlargement of (**c**)

surface. It is readily observed that many bubbles are carried away from the oscillator surface and migrated in the convective flow. These bubbles never contributed to the erosion of the oscillator.

9.7 Interaction with Arrayed Acrylic Cylinders

Figure 9.62 shows stress wave propagations along 10 mm diameter and 10 mm long acrylic cylinders packed in a 5 × 6 arrangement and submerged in a 10 mm wide water chamber. A 9 mg AgN_3 pellet was exploded on the top of the arrayed cylinders. Underwater shock wave propagated at 1.5 km/s, whereas the stress wave propagated at 2.9 km/s in the cylinders. The stress wave transmitted into the cylinder through the contact point of the acrylic cylinders. However, cylinders touched tightly at their vertical contact points but did loosely at their side contact points. Therefore, the stress wave propagated selectively downward through the

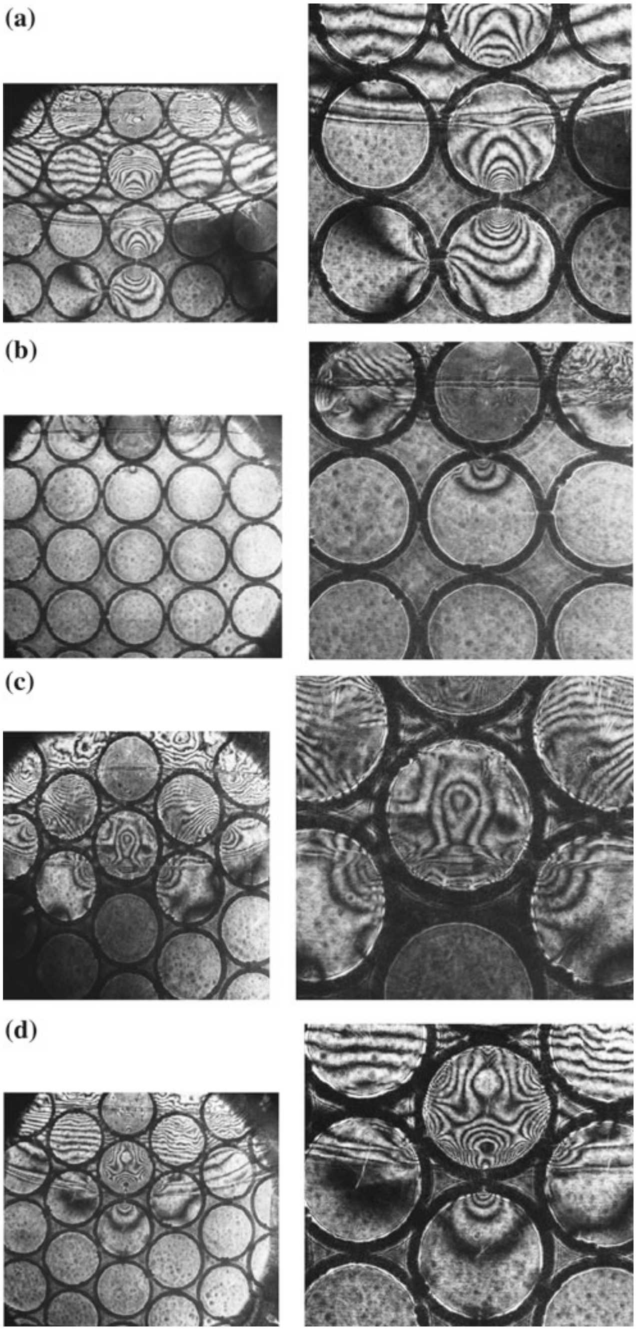

Fig. 9.62 Stress wave propagation in a 5 × 6 arrayed acrylic cylinders, 9 mg AgN_3: **a** #95100515, enlargement; **b** #95100517, enlargement; **c** #95100520, enlargement; **d** #95100522, enlargement

vertical contact points. Fringes appeared inside the cylinder propagating at much faster speed than that in water. Unlike stress waves visualized by photo-elasticity, the fringes appeared in the acrylic cylinders show the difference in phase angles which occurred during the double exposures. If the relationship between the refractive index and the density in acryl are known, the values of the stress would be determined directly by counting the fringe distributions.

9.8 Super-Cavitation

9.8.1 High-Speed Entry of a Slender Body into Water

Can a slender body move at a supersonic speed in water? The slender body was launched by a ballistic range into water at a supersonic speed. The slender body was launched at 1600 m/s into water (Saeki 1993). Figure 9.63a shows the slender body and a sabot. Figure 9.63b shows a test chamber installed in a ballistic range. The chamber had a 300 mm wide and 300 mm diameter cylindrical shape having 20 mm thick observation glass windows. The slender body was 10 mm diameter and 40 mm long and was made of titanium alloy. The slender body was launched into the test chamber from a 100 mm diameter entry port which was separated by a 30 μm thick Mylar membrane from the test chamber filled with water and accommodated in the ballistic range. As the entry speed was 1600 m/s, a bow shock appeared ahead of the slender body. The window glass of the test chamber was illuminated by a flood lamp and the images were recorded by a high-speed video camera Shimadzu SH100 at 10^6 frame/s. In Fig. 9.64 selective images were displayed at the frame interval of 16 μs.

Figure 9.64 shows sequential observation of the slender body projected horizontally into the test chamber. However, its head was slightly shifted upward so that a centrifugal force shifted its course and deformed it. Figure 9.64a shows an

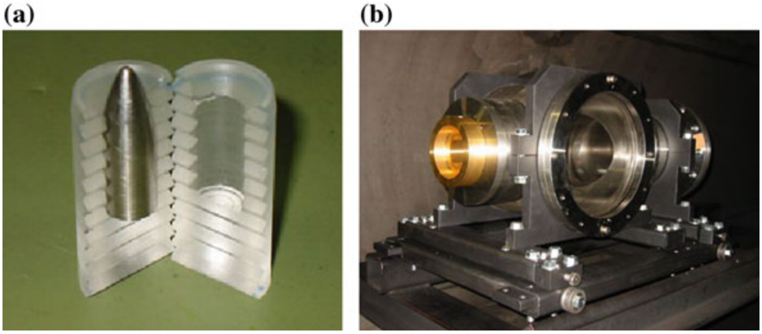

Fig. 9.63 Supersonic entry of a slender body projected into water: **a** a slender body made of titanium alloy; **b** test chamber

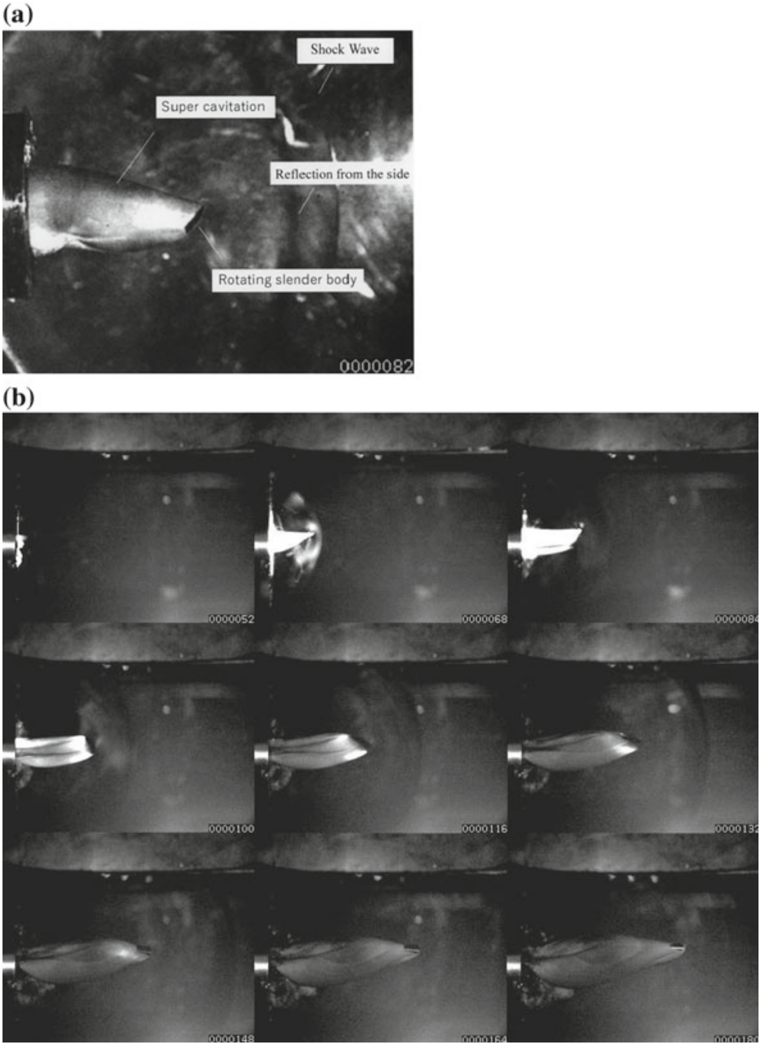

Fig. 9.64 High speed entry of a titanium slender body, sequential observation at frame interval of 16 μs: **a** enlarged view; **b** sequential observation (Saeki 1993)

enlarged image at later time. Immediately after the entry into water, a bow shock wave appeared in front of it. The bow shock wave attenuated quickly to subsonic speed relative to the sound speed in water. As soon as the slender body entered into water, its entire body was covered with water vapor bubble. It started to spin and immediately had an upright position seen in Fig. 9.64.

Inside the super-cavitation bubble, water vapor filled at vapor pressure which kept the balance with the pressure outside the cavitation bubble. Faintly grey

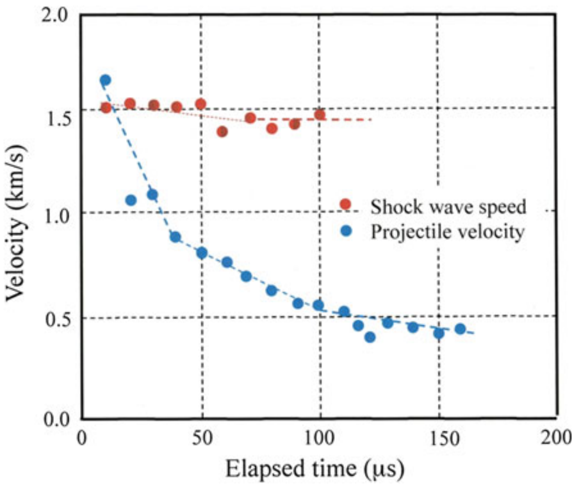

Fig. 9.65 Summary of Fig. 9.65, time variation of slender body velocity and shock wave speed

patterns are observable over its surface. The grey patterns are distributed not randomly but slightly coherently over the surface. The separation distance looked slightly elongated with elapsed time. Sequential observation of the grey patterns indicates that the space inside the super-cavitation bubble is not uniformly motion-less. In watching the time variation of the distributed grey patterns, it is speculated that high-speed flows are induced inside the super-cavitation. The quick attenuation and spinning motion would generate disturbances which would decisively produce high-speed flows and shock waves inside the super-cavitation bubble.

Figure 9.64b shows sequential images of the high-speed entry of the slender body into water. It entered into water at a supersonic speed and immediately decelerated to a subsonic speed. When the slender body hit the Mylar membrane placed at the entrance port, its impact made the slender body's head slightly upward. Its slightest upward inclination was amplified with propagation. The slender body immediately started to spin, which generated an enormous centrifugal force and bent the slender body as seen in Fig. 9.64.

Figure 9.65 summarizes images presented in Fig. 9.64 and shows the time variation of the speed of the slender body. The ordinate denotes the slender body velocity in km/s. The abscissa denotes elapsed time in μs. Filled red circles denote shock wave speed and filled blue circles denotes the speed of the slender body. The shock wave attenuated quickly from low supersonic speed to the sonic speed, whereas the slender body attenuated drastically from 1.6 km/s to approximately 0.5 km/s. The typical Reynolds number ranges of this flow region is from about 10^4 to 10^6. The drag coefficient C_D of this entry is so far estimated from the trajectory of the attenuating the slender body $C_D = 0.13$. The value of C_D for 1:4 cylinder in this Reynolds number range is $C_D = 0.87$ (Saeki 1993). It is concluded that the slender body moving in water at high-speed is surrounded by super-cavitation bubbles and the resulting value of C_D is significantly reduced to 0.13.

9.8.2 High-Speed Entry of a Sphere into Water

Figure 9.66a shows a 10 mm diameter tilted powder gun projecting a four split sabot made of polycarbonate and a 7.9 mm diameter stainless steel bearing ball contained in the sabot at any angles from 0° to 90°. Kikuchi (2011) projected the sabot and a 7.9 mm diameter ball vertically into water surface at the speed ranging from 300 to 1600 m/s. Figure 9.66b shows a direct shadowgraph of the entry of a 7.9 mm diameter sphere at 1143 m/s. Although the entry speed was subsonic in terms of the sound speed in water, at the moment of the projectile's water entry, the stagnation pressure momentarily reached at the air/water interface reached about 1.7 GPa which was almost one half of the detonation pressure of a AgN_3 pellet. Then, the high pressures propagate at the sonic speed in water. The projectile in water attenuated propagating at subsonic speed. In short, the projectile's water entry produced in front of the sphere a train of compression waves propagating at the sonic speed. This observation never contradicts the gas-dynamic interpretation, if the distance between the train of compression waves and the moving sphere is defined as a shock stand-off distance, the shock stand-off distance becomes infinitely long, when the sphere moved slowly.

Figure 9.67 shows sequential images of a 7.9 mm sphere's entry into water at the speed of 1143 m/s. The images were selected out of the recorded pictures taken by Shimadzu HS100 at 250,000 frame/s and exposure time of 500 ns. A detached shock was visible ahead of the sphere and the entry speed is equivalent to Ms = 0.763 in terms of the sound speed in water. If the train of compression waves

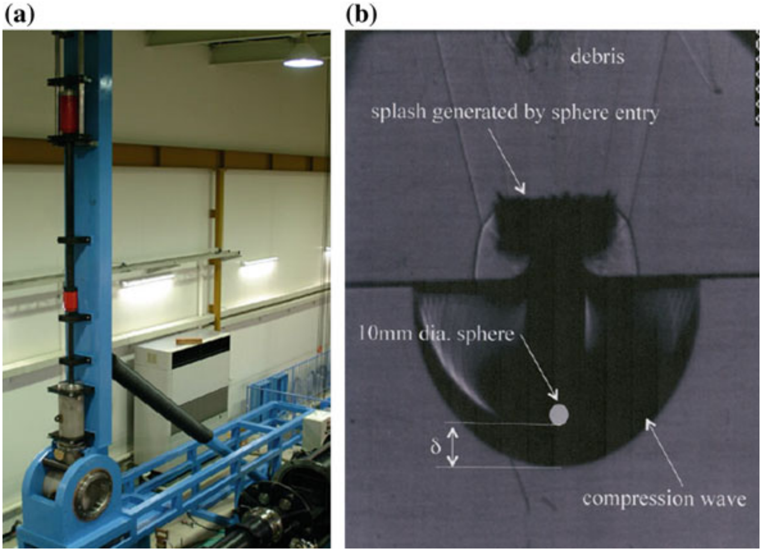

Fig. 9.66 Vertical entry of a sphere into water at entry speed of 1143 m/s: **a** a vertical two-stage light gas gun; **b** entry of 7.9 mm diameter sphere vertically into water at 1143 m/s

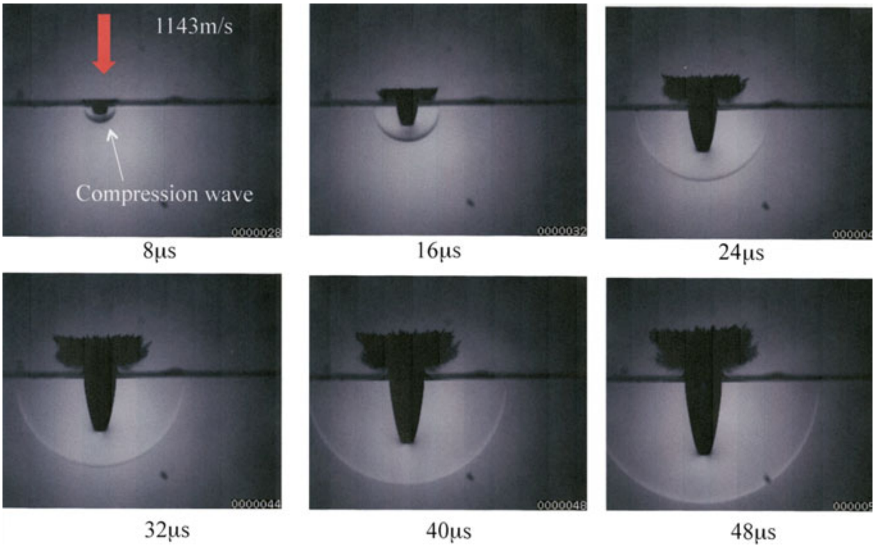

Fig. 9.67 Sequential observation of the entry of a 7.9 mm diameter sphere into water at 1143 m/s

is defined to be a bow shock propagating at the sonic speed. The dimension-less shock stand-off distance δ/d seen in Fig. 9.66 is about 2.0 in Fig. 9.67a. In Fig. 9.67, the sphere is decelerating and then the δ/d increases. In the 5th frame of Fig. 9.67, the δ/d is about 3.0. The similar trend was already discussed regarding the shock stand-off distance over a 40 mm diameter sphere launched in the ballistic range. The sphere dragged super-cavitation bubble whose surface looked a simple smooth interface. Although the visualization was conducted by a conventional direct shadow graph, if the test field was illuminated by a flood lamp in the similar manner as seen in Fig. 9.64, the surface irregularity of the super-cavitation would be observed.

Figure 9.68 shows the sequential observations of the supersonic entry of a 7.9 mm diameter sphere at 1539 m/s. Splashes from the water surface moved at the speed of the reflected shock wave from the water surface. This entry speed is equivalent to Mach number Ms = 4.46 in air and to Ms = 1.02 in water. While propagating in water, the sphere's speed varies from supersonic to subsonic. However, the dimension-less shock stand-off distance δ/d did not show any discontinuous change but increased monotonously.

Figure 9.69 summarizes results presented in Fig. 9.68. The ordinate denotes the sphere's penetration depth from water surface in mm. The abscissa denotes elapsed time in μs. Green filled circles denote positions of the sphere and red filled circles denotes the location of the shock wave. The sphere attenuates quickly with propagation and hence the dimension-less shock stand-off distance δ/d increases monotonously with elapsing time.

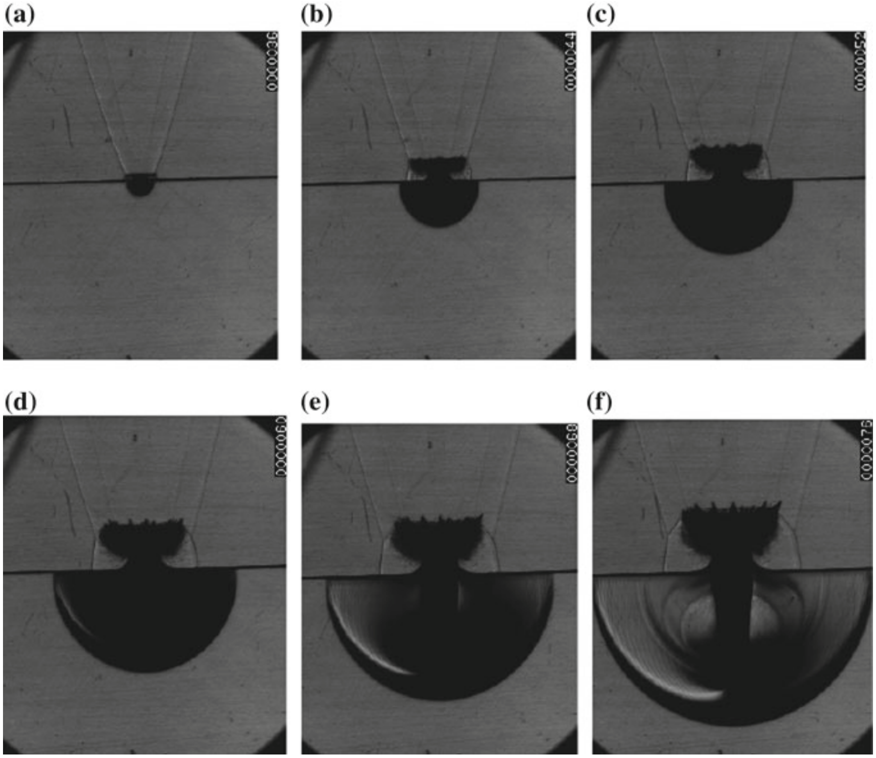

Fig. 9.68 Sequential observation of the entry of a 7.9 mm diameter sphere into water at 1539 m/s: **a** 8 μs; **b** 16 μs; **c** 24 μs; **d** 32 μs; **e** 40 μs; **f** 48 μs

Fig. 9.69 Trajectory of sphere and shock wave at entry speed of 1539 m/s

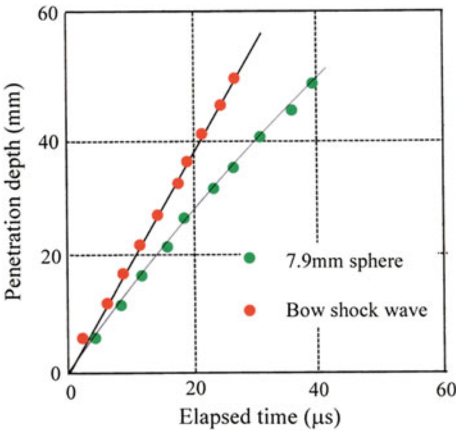

References

Abe, A. (1989). *Study of diffraction of shock wave released from the open end of a shock tube* (Ph.D. thesis). Graduate School of Engineering, Faculty of Engineering Tohoku University.

Abe, A., Ohtani, K., Takayama, K., Nishio, S., Mimura, H., & Takeda, M. (2010). Pressure generation from micro-bubble collapse at shock wave loading. *Journal of Fluid Science and Technology, 5,* 235–246.

Chaussey, Ch., Schmiedt, E., Jocham, D., Walter,V., Brendel, W., Forsmann, B., & Hepp, W. (1982). *Extracorporeal shock wave lithotripsy. New aspects in the treatment of kidney stone disease*. Kerger.

Coleburn, N. L., & Roslund, L. A. (1970). Interaction of spherical shock waves in water. In *Proceedings of 15th International Symposium on Detonation, Pasadena* (pp. 581–588).

Esashi, H. (1983). *Shock wave propagation in liquids* (Master thesis). Graduate School of Engineering, Faculty of Engineering, Tohoku University.

Glass, I. I., & Heuckroth, L. E. (1968). Low-energy spherical underwater explosions. *Physics of Fluids, 11,* 2095–2107.

Hayakawa, S. (1987). *Study of shock/bubble interaction in highly viscous liquids* (Master thesis). Graduate School of Engineering, Faculty of Engineering Tohoku University.

Hirano, T. (2001) *Development of revascularization of cerebral thrombosis using laser induced liquid jets* (M.D. thesis). Graduate School of Medicine, Tohoku University.

Ikeda, K., Matsuda, M., Tomita, K., & Takayama, K. (1999). Application of extracorporeal shock wave on bone. Basic and clinical study. In G. J. Ball, R. Hillier, & G. T. Robertz (Eds.), *Proceedings of 22nd ISSW, Shock Waves, London* (Vol. 1, pp. 623–626).

International Maritime Organization. *Science of ship and the sea.* Retrieved from http://www.imo/org/home.asp.

Kikuchi, T. (2011). *A shock dynamic study of high-speed impact onto condensed matter* (Ph.D. thesis). Graduate School of Engineering, Faculty of Engineering Tohoku University.

Kuwahara, M., Kambe, K., Kurosu, S., Orikasa, S., & Takayama, K. (1986). Extracorporeal stone disintegration using chemical explosive pellets as an energy source of underwater shock waves. *Journal of Urology., 135,* 814–817.

Nagayasu, N. (2002). *Study of shock waves generated by micro explosion and their applications* (Ph.D. thesis). Graduate School of Engineering, Faculty of Engineering, Tohoku University.

Ohtani, K., & Takayama, K. (2010) Shock wave interaction phenomena with a single helium gas bubble in liquid. In *7th International Conference on Flow Dynamics, Sendai* (pp. 120–121).

Okazaki, K. (1989). Fundamental study in extracorporeal shock wave lithotripsy using piezoceramics. *Japanese Journal of Applied Physics, 28*, 143–145.

Sachs, R. G. (1944). *The dependence of blast on ambient pressure and temperature* (BRL Report, No. 466).

Saeki, T. (1993). *Super-cavitation flows of a high speed projectile launched by two-stage light gas gun* (Master thesis). Graduate School of Engineering, Faculty of Engineering, Tohoku University.

Sanada, N., Ikeuchi, J., Takayama, K., & Onodera, O. (1983). Generation and propagation of cavitation induced shock waves in an ultrasonic vibration testing. In: D. Archer & B. E. Milton (Eds.), *Proceedings of 14th International Symposium on Shock Tubes and Waves, Sydney* (pp. 404–412).

Shima, A. (1997). Studies on bubble dynamics. *Shock Waves, 7,* 33–42.

Shitamori, K. (1990). *Study of propagation and focusing of underwater shock focusing* (Master thesis). Graduate School of Tohoku University Faculty of Engineering, Tohoku University.

Tait, P. G. (1888). Report on physical properties of flesh and of sea water. *Physics and Chemistry Challenger Expedition, IV*, 1–78.

Takayama, K. (1983). Application of holographic interferometry to shock wave research. In *International Symposium of Industrial Application of Holographic Interferometry, Proceedings of SPIE* (Vol. 298, pp. 174–181).

Takayama, K. (1987). Holographic interferometric study of shock wave propagation in two phase media, In H. Groenig (Ed.), *Proceedings of 16th International Symposium on Shock Tubes and Waves, Aachen* (pp. 51–62).

Takayama, K. (1990). High pressure generation by shock wave focusing in a confined ellipsoidal cavity. In K. Takayama (Ed.), *Proceedings of International Workshop on Shock Wave Focusing* (pp. 217–226). Institute of High Speed Mechanics, Sendai.

Takayama, K., Yamamoto, H., & Abe, A. (2015). Underwater-shock/bubble interaction and its application to biology and medicine. In R. Bonazza, D. Ranjan (Eds.), *Proceedings of 29th ISSW, Shock Waves, Madison* (Vol. 2, 861–868).

Yamada, K. (1992). *Study of shock wave interaction with gas bubbles in various liquids* (Doctoral thesis). Graduate School of Tohoku University Faculty of Engineering, Tohoku University.

Yutkin, L. A. (1950). Apparat YRAT-1 Medeport USSR Moscow.